Title

KINETICS AND ENERGY TRANSFER OF GAS-SURFACE SCATTERING

Permalink

https://escholarship.org/uc/item/1kd9g5tn

Author

Lin, T-H.

Publication Date

1983-08-01

Lawrence Berkeley Laboratory

UNIVERSITY OF CALIFORNIA

Materials & Molecular Research Division

KINETICS AND ENERGY TRANSFER OF GAS-SURFACE SCATTERING

Te-Hua Lin
(Ph.D. Thesis)

August 1983

DISCLAIMER

This document was prepared as an account of work sponsored by the United States Government. While this document is believed to contain correct information, neither the United States Government nor any agency thereof, nor the Regents of the University of California, nor any of their employees, makes any warranty, express or implied, or assumes any legal responsibility for the accuracy, completeness, or usefulness of any information, apparatus, product, or process disclosed, or represents that its use would not infringe privately owned rights. Reference herein to any specific commercial product, process, or service by its trade name, trademark, manufacturer, or otherwise, does not necessarily constitute or imply its endorsement, recommendation, or favoring by the United States Government or any agency thereof, or the Regents of the University of California. The views and opinions of authors expressed herein do not necessarily state or reflect those of the United States Government or any agency thereof or the Regents of the University of California.

KINETICS AND ENERGY TRANSFER OF GAS-SURFACE SCATTERING

Te-Hua Lin

Materials and Molecular Research Division
Lawrence Berkeley Laboratory

and

Department of Physics
University of California
Berkeley, California 94720

TO MY PARENTS

TABLE OF CONTENTS

ACKNOWLEDGEMENTS

Chapter II. The help and friendship of Gloria Pelatowski, Jim Severns, Hank Brendle, Weyland Wong, John Holthuis, Kent Gaugler, Mike Kujala, Walt Toutolmin, Emery Kozak, Bob McCaslin, Hal Wells, Marian Larsen, Catherine Sterling and Sandy Stewart are greatly appreciated. Last, but not least, I would like to thank Ms. Diana Morris for her fast and accurate typing of this thesis.

Words are inadequate to express my thanks to my wife, Cherry, for her support and understanding. The love and encouragement of my parents, brothers and sisters have helped greatly to make this work possible. Finally, I thank my sons, Erwin and Eric, who have kept me from overworking in the laboratory.

KINETICS AND ENERGY TRANSFER OF GAS-SURFACE SCATTERING

Te-Hua Lin

Materials and Molecular Research Division
Lawrence Berkeley Laboratory

and

Department of Physics
University of California
Berkeley, California 94720

ABSTRACT
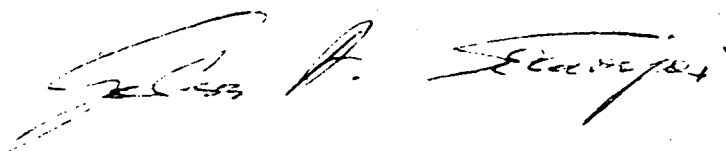
The dynamics of gas-solid interactions for strongly interacting systems has been investigated using molecular beam-surface scattering techniques. The angular, translational energy and internal energy distributions, and residence time of scattered molecules were measured. The residence time of CO on Pt(111) and Pt(557) indicates that while CO can be adsorbed at both step and terrace sites, the desorption kinetics are controlled by the steps. The kinetics of NO/Pt were found to be more complex than those of CO/Pt. The data indicate that one high adsorption energy state is sampled above 525K and a lower adsorption energy state appears suddenly below 480K. The data cannot be explained without using nonlinear processes.

The distribution of energy among all the modes has been measured for NO scattered from Pt(111). The translational and vibrational energy accommodation coefficients are nearly equal to one for $T_s < 900K$ and deviate from unity above this temperature due to

non-equilibrated desorption. The rotational energy accommodation is very poor compared with that of the other two modes. This may be due to the fact that NO is not a free rotor on the surface.

The H_2-D_2 exchange reaction on Pt(557) was found to proceed via a Langmuir-Hinshelwood mechanism. Although the angular distribution of the HD product is slightly peaked at the normal, the velocity distribution is slightly colder than the substrate and the deviation increases as the detection angle increases. This result is explained by a model which assumes that as soon as H and D recombine, they will immediately feel a repulsive force which is most likely perpendicular to the surface.

Using atomic hydrogen and deuterium incident beams, we found that the velocity of desorbing HD molecules increases as the crystal temperature decreases from 300 to 200K. At 200K, the velocity distribution is considerably wider than the Maxwellian distribution and there is a significant amount of HD leaving the surface with 1915K translational energy. The waveform measurement indicates that the residence time decreases for some of the incident atoms as the crystal temperature decreases from 300 to 200K. This result is explained by assuming that at high coverages some of the incident atoms can recombine before they are in thermal equilibrium with the surface.

CHAPTER I.   INTRODUCTION

In the past decade, significant progress has been made in understanding the structural and electronic properties of molecular adsorbates on various single crystal surfaces. The techniques used to study these properties include ultraviolet and x-ray photoelectron spectroscopy (UPS, XPS) (1-6), low energy electron diffraction (LEED) (7), electron energy loss spectroscopy (EELS) (8), Auger electron spectroscopy (AES) (9,10), and thermal desorption spectroscopy (TDS) (11). However, the progress in understanding the dynamics of gas-surface interactions has not proceeded as rapidly due to the complexity of dynamic processes. When a gas molecule collides with a solid surface, a number of processes may occur. The molecule may be elastically or inelastically scattered back into the gas phase. It may lose part of its translational kinetic energy to the solid and become trapped on the surface. The trapped molecule is initially vibrationally excited but can migrate on the surface and become de-excited. The molecule may adsorb dissociatively and various recombination processes, which could be either exothermic or endothermic depending on the interaction potential and the initial atomic state, must occur before desorption can take place. At any time a trapped molecule on the surface may undergo desorption by gaining some thermal energy from the solid.

The molecular beam-surface scattering technique provides one of the best ways of investigating the detailed dynamics of gas-surface

interactions. The basic characteristics of the beam–surface scattering experiment which allow the interaction details to be probed are as follows. First, the incident beam can be prepared with a well defined kinetic energy (12), internal energy state (13,14), and direction. Secondly, there are no collisions between the incident molecules or the outgoing products or between those molecules and any surfaces other than the one studied. Therefore, the states of the molecules before and after the collision with the surface can be well characterized. Finally, the orientation of the macroscopic or microscopic structure of the surface is fixed, relative to the incident particles. The types of information one can obtain with the beam–surface scattering apparatus are the following:

1. Surface crystallography--the surface structure can be derived from the diffraction of light atoms or molecules from the surface. This method is sensitive only to the first surface layer and is non-destructive (15–17).

2. Physisorption potential--the attractive part of the physisorption potential can be studied by looking at bound state resonances of the light particle diffraction intensity (18–20).

3. Low-energy excitations--surface phonon dispersion can be determined by measuring the angular distribution and time-of-flight of the scattered light particles (21–23). For multi-phonon processes, the fundamental aspects of gas-surface accommodation can be extracted (24,25).

4. Average energy transfer—Energy transfer mechanisms for strongly interacting gas-surface systems can be investigated. When coupled with theory, these types of measurements can have considerable impact on our understanding of molecule-surface interaction potentials and their associated dynamics (26).

5. Reactive scattering—the measurement of velocity and internal energy distributions that deviate from a Boltzmann distribution at the crystal temperature and of non-cosine angular flux distributions can provide valuable insights into the molecular dynamics of the desorption process (27-39). The adsorption process can be investigated by the measurement of the sticking probabilities as a function of velocity, internal energy, angle, crystal structure and temperature (40-43). The modulated molecular beam scattering technique is used for the study of the kinetics and mechanisms of elementary reactions on and with surfaces (44-48).

We have used molecular beam-surface scattering techniques to investigate the last two types of dynamical processes because of their practical importance. The angular, translational, and internal energy distributions of scattered products have been measured. Translational energies were measured using cross-correlation time-of-flight (TOF) techniques. The internal energy distributions of scattered NO were measured using two-photon ionization (TPI) techniques. Surface residence time and reaction mechanisms were investigated using

modulated molecular beams. In one case, atomic hydrogen and deuterium
were used as the incident beams and very interesting results were
found at low crystal temperature.

The area of our scattering studies is obviously most complex and
is interesting from both fundamental and applied points of view.
Depending on the experimental variables measured, various types of
qualitative dynamic information can be extracted. For the modulated
molecular beam scattering, the incident beam is square wave modulated
and the waveform or amplitude and phase of the first Fourier component
of the product is measured as a function of reactant pressure, temper-
ature and modulation frequency. The data are used to test models
describing the elemental chemical reaction steps at the surface. For
a given set of data it is not possible to extract a unique model for
the chemical reaction mechanism, but it is easy to test any proposed
alternative model. There are many experimental results in this area,
and the reader is referred to several review articles (49,50). The
theoretical modeling has also been reviewed (47,48).

The measurements of angular, translational energy, and internal
energy distributions of reaction product or strongly scattered
molecules are used for extracting information about energy exchange
dynamics, reaction mechanisms, desorption dynamics, scattering
mechanisms, and the interaction potential. The deviation of energy
distributions from a Boltzmann distribution, the polar angle dependence
of energy distributions and the non-cosine angular flux distributions
allow one to obtain dynamic information. However, the lack of

systematically extended data sets and theoretical work make it difficult to arrive at some uniquely defined dynamical model.

Experimentally, Comsa et al. measured H_2 and D_2 TOF distributions for associative desorption, after permeation through Ni, Pd, and Cu, from both clean and sulfur-contaminated surfaces (30-32). They found that the velocity distribution is "hotter" than the corresponding substrate temperature for normal angle detection but "colder" for grazing angle detection. The experimental findings for desorbing CO_2 resulting from CO oxidation on platinum foil (51) are similar to those of D_2 desorbing from Ni. For the same reaction, Mantell et al. have found that the CO_2 product has much more internal excitation than would be the case for equilibrium at the surface temperature (52). Thorman et al. have found that desorbing N_2, after recombination of adsorbed atomic N on sulfur contaminated iron surface, is vibrationally "hot" and rotationally "cold" as compared with the crystal temperature (34). The desorbing D_2O after the D_2-O_2 reaction on Pt(111) was found to be "colder" than the corresponding substrate temperature (35). The rotational temperature of OH formed during the oxidation of H_2 by O_2 and N_2O is that expected at the surface temperature (53-54). NO desorbed from Ru (100) was found to be rotationally cold (55).

Although theoretical modeling is quite successful for the weak interaction system (56-58), it is in its infancy for strong interaction system or reactive scattering. The main difficulties are as follows.

First, the system is essentially an infinite particles system but without the full lattice symmetry. Secondly, there is no simple way of constructing realistic or reliable gas-surface interaction potentials. Thirdly, the relative importance of energy exchange with the vibrational modes and electronic energy of the solid is still controversial and accurate ways of dealing with excitations or de-excitations of both modes are still under investigation. Finally, the long interaction time (millisecond) makes calculations prohibitively expensive. For more detailed information and examples, the reader is referred to a review article (59).

The lack of a well developed theory makes the quantitative interpretation of experiments difficult, but also implies that having careful and detailed experimental results is important. The detailed experimental results can be used to check the reliability of theoretical calculations and construct an empirical gas-surface interaction potential. Understanding the detailed dynamics of gas-surface interactions is only possible when both experiment and theory are well developed for a large number of systems.

The rest of the thesis will be organized as follows. Chapter II describes in detail the extensive modification of an existing time-of-flight apparatus. Also discussed is surface characterization with helium beam scattering. The modulated molecular beam scattering of CO and NO from Pt(111) and the stepped Pt(557) crystal surface is presented in Chapter III. We have found that while the incident NO and CO can be adsorbed on both terrace and step sites, their desorption

kinetics are completely controlled by steps. Chapter IV describes the angular, translational, rotational, and vibrational energy distributions of NO scattered from the Pt(111) surface. The rotational energy accommodation is found to be very poor as compared with that of the other two modes.

The H_2-D_2 exchange study on Pt(557) is presented in Chapter V and a model is proposed to explain the results that although the angular distribution of the product HD is slightly peaked at the normal, the velocity distribution is slightly colder than the substrate temperature and the deviation increases as the detection angle increases. Chapter VI describes the dynamics of atomic hydrogen and deuterium recombination on the Pt(557) surface. The incident beams are atomic and we have found that at high coverage some of the incident atoms can react with chemisorbed atoms before they are in thermal equilibrium with the surface. Chapter VII serves as a short summary of the work presented here.

References

1. D. A. Shirley, CRC Critical Rev. in Solid State and Material Sci. 10, 373 (1980-82).

2. S. Y Tong and C. H. Li, CRC Critical Rev. in Solid State and Material Sci. 10, 209 (1980-82).

3. G. Margaritondo, J. E. Rowe, J. Vac. Sci. Technol. 17, 561 (1980).

4. P. Weightman, Rep. Prog. Phys. 45, 753 (1982).

5. B. Feuerbacher and R. F. Willis, J. Phys. C: Solid State Phys. 9, 169 (1976).

6. M. I. Holmes and T. Gustafsson, Phys. Rev. Lett. 47, 443 (1981).

7. M. A. Van Hove and S. Y. Tong, Surface Crystallography by LEED, Springer Verlag, Berlin, 1979.

8. H. Ibach and D. L. Mills, Electron Energy Loss Spectroscopy and Surface Vibrations, Academic Press, New York, 1982.

9. P. H. Holloway, Adv. in Electronics and Electron Phys. 54, 241 (1980).

10. R. Weissmann and K. Muller, Surface Sci. Reports, 105, 251 (1981).

11. D. A. King, Surface Sci. 47, 384 (1975).

12. J. B. Anderson, R. P. Andres, and J. B. Fenn, Advances in Chem. Phys. 10, 275 (1966).

13. T. W. Riddle, M. Onellion, F. B. Dunning and G. K. Walters, Rev. Sci. Instrum. 52, 797 (1981).

14. J. G. Pruett and R. N. Zare, J. Chem. Phys. 64, 1774 (1976).

15. K. H. Rieder and T. Engel, Phys. Rev. Lett. 45, 824 (1980).

16. M. J. Cardillo and G. E. Becker, Phys. Rev. B, 21, 1497 (1980).

17. J. M. Horne and D. R. Miller, Surface Sci. 66, 365 (1977).

18. M. W. Cole and D. R. Frankl, Surface Sci. 70, 585 (1978).

19. G. E. Becker, M. J. Cardillo, J. A. Serri and D. R. Hamann, Phys. Rev. B, 28, 504 (1983).

20. H. Hoinkes, Rev. Mod. Phys. 52, 933 (1980).

21. G. Brusdeylins, R. B. Doak, and J. P. Toennies, Phys. Rev. Lett. 46, 427 (1981).

22. G. Brusdeylins, R. B. Doak, and J. P. Toennies, Phys. Rev. Lett. 44, 1417 (1980).

23. G. Brusdeylins, R. B. Doak, and J. P. Toennies, J. Chem. Phys. 75, 1784 (1981).

24. C. A. Becker, D. J. Auerbach, J. P. Cowin, K. C. Janda, L. Wharton, and J. E. Hurst, Rarified Gas Dyn. 11, 1427 (1979).

25. J. E. Hurst, C. A. Becker, J. P. Cowin, K. C. Janda, L. Wharton, and D. J. Auerbach, Phys. Rev. Lett. 43, 1175 (1979).

26. K. C. Janda, J. E. Hurst, C. A. Becker, J. P. Cowin, L. Wharton, and D. J. Auerbach, Surface Sci. 93, 270 (1980).

27. W. Van Willigen, Phys. Lett. 28A, 80 (1968).

28. R. L. Palmer and J. N. Smith, J. Chem. Phys. 60, 1453 (1974).

29. A. E. Dabiri, T. J. Lee and R. E. Stickney, Surface Sci. 26, 522 (1971).

30. G. Comsa, R. David and B. J. Schumacher, Surface Sci. 85, 45 (1979).

31. G. Comsa, R. David and B. J. Schumacher, Surface Sci. 95, L210 (1980).

32. G. Comsa and R. David, Surface Sci. 117, 77 (1982).

33. R. P. Thorman, D. Anderson and S. L. Bernasek, Phys. Rev. Lett. 44, 743 (1980).

34. R. P.Thorman and S. L. Bernasek, J. Chem. Phys. 74, 6498 (1981).

35. S. T. Ceyer, W. L. Guthrie, T. H. Lin and G. A. Somorjai, J. Chem. Phys. 78, 6982 (1983).

36. G. Comsa, R. David and K. D. Rendalic, Phys. Rev. Lett. 38, 775 (1977).

37. T. L. Bradley, A. E. Dabiri and R. E. Stickney, Surface Sci. 29, 590 (1972).

38. T. L. Bradley and R. E. Stickney, Surface Sci. 38, 313 (1973).

39. M. Balooch and R. E. Stickney, Surface Sci. 44, 310 (1974).

40. J. T. Yates, J. J. Zinck, S. Sheard, and W. H. Weinberg, J. Chem. Phys. 70, 2266 (1979).

41. S. G. Brass, D. A. Reed and G. Ehrlich, J. Chem. Phys. 70, 5244 (1979).

42. T. Engel, J. Chem. Phys. 69, 373 (1978).

43. C. T. Campbell, G. Ertl, H. Kuipers, and J. Segner, J. Chem. Phys. 73, 5862 (1980).

44. T. Engel and G. Ertl, Adv. Catal. 29, 1 (1979).

45. M. Salmeron, R. J. Gale and G. A. Somorjai, J. Chem. Phys. 67, 5324 (1977).

46. H. H. Sawin and R. P. Merrill, J. Chem. Phys. 73, 996 (1980).

47. D. R. Olander and A. Ullman, Intern. J. Chem. Kin. 8, 625 (1976).

48. J. A. Schwarz and R. J. Madix, Surface Sci. 46, 317 (1974).

49. M. J. Cardillo, Ann. Rev. Phys. Chem. <u>32</u>, 331 (1981).

50. S. T. Ceyer and G. A. Somorjai, Ann. Rev. Phys. Chem. <u>28</u>, 477 (1977).

51. C. A. Becker, J. P. Cowin, L. Wharton and D. J. Auerbach, J. Chem. Phys. <u>67</u>, 3394 (1977).

52. D. A. Mantell, S. B. Ryali, B. L. Halpern, G. L. Haller and J. B. Fenn, Chem. Phys. Lett. <u>81</u>, 185 (1981).

53. M. E. Ulmstead, L. D. Talley, D. F. Terault, and M. C. Lin, Opt. Eng. <u>19</u>, 94 (1980).

54. L. D. Tally, W. A. Sanders, D. J. Bogan, and M. C. Lin, Chem. Phys. Lett. <u>66</u>, 584 (1979).

55. R. R. Cavanagh and D. S. King, Phys. Rev. Lett. <u>47</u>, 1829 (1981).

56. J. C. Tully, J. Chem. Phys. <u>73</u>, 1975 (1980).

57. J. D. Doll, J. Chem. Phys. <u>59</u>, 1038 (1973).

58. D. Kumamoto and R. Silbey, J. Chem. Phys. <u>75</u>, 5164 (1981).

59. T. C. Tully, Ann. Rev. Phys. Chem. <u>31</u>, 319 (1980).

CHAPTER II. EXPERIMENTAL

2.1 Introduction

The size of the molecular beam–surface scattering apparatus is generally appreciably larger than that of other systems for surface science studies. The basic requirements for a surface scattering apparatus are as follows. It must contain the conventional surface analytic facilities such as an Auger Electron Spectrometer, Low Energy Electron Diffraction equipment, and an ion sputtering gun. Because of low reactivity and low detection sensitivity for neutral molecules (atoms), one needs a high flux, incident molecular beam source requiring at least two stages of differential pumping. High pumping speed is necessary to keep the scattering chamber under the ultra-high vacuum conditions required for sample preparation and maintenance. The detector is usually a mass spectrometer, often rotatable and two-stage differentially pumped, again necessarily because of the low reactivity and low detection sensitivity of neutral molecules. A chopper and motor are required to modulate the incident or scattered beam for the kinetic and time-of-flight measurements. With such a complex system, careful design and construction are very important to achieve a high degree of reliability.

The apparatuses and the experimental conditions used for this thesis are very different from one chapter to another; thus, they will be described in each chapter. In this chapter, the modification of an existing time-of-flight apparatus will be described in detail. The modified apparatus is used for the studies presented in Chapter 5

and 6 and is found to be much more reliable than the original equipment. To illustrate the flexibility of the molecular beam-surface scattering apparatus, helium scattering as a surface analytical method is presented in Section 4.

2.2 Description of the Time-of-Flight Apparatus without Modification

The apparatus without extensive modification has been described in detail previously (1,2). A brief description of the apparatus and the reasons that made the extensive modifications necessary for the present study will be described in this section. A schematic diagram of the apparatus is shown in Fig. 1. The two independent and twice differentially pumped beams are incident on the crystal surface located at the center of the scattering chamber. The beams form a 30° angle with each other and can be either high intensity supersonic or effusive atomic beams. The atomic beams are produced in the microwave discharge sources. The primary beam is modulated by a tuning fork chopper at 150 Hz for the angular distribution and residence time measurements.

The main scattering chamber, which is pumped by a LN_2 trapped-diffusion pump, noble gas ion pump and a titanium sublimator, is equipped with instruments for Auger Electron Spectroscopy (AES), Low Energy Electron Diffraction (LEED) and argon ion sputtering. The manipulator can translate the sample and rotate the surface around a perpendicular and parallel axis as well as tilt the sample surface. The crystal is heated by electron bombardment and its temperature is monitored with a thermocouple spot welded to the edge of the crystal.

The two-stage differentially pumped detector chamber, which is enclosed in the scattering chamber, can be rotated about the sample located at the center of the scattering chamber. The signal is detected with a mass spectrometer which consists of a cross-beam Pierce gun ionizer, UTI quadrupole rods and electronics, and a Channeltron electron multiplier. The chopper motor is bolted onto the side of the detector chamber so that one can measure the time-of-flight (TOF) of the scattered beam at any angle with respect to the crystal normal. Since the scattered beam is chopped instead of the incident beam, the TOF distributions are not affected by the unknown surface residence times which can be very long (milliseconds) for many reactions. The flight path between the chopper wheel and the center of the ionizer is about 12 cm. A pseudo-random chopper is used because of its large duty cycle (50 percent) as compared with that of the single slit chopper (2 percent) (3-5). A light emitting diode and a photodiode mounted around the chopper wheel produce a trigger signal for the multi-channel scalar.

The signal from the Channeltron is passed through a pre-amplifier, discriminator, and a pulse shaper. For angular distribution measurements, the output pulses are fed into two counters gated by a timer-gater module which is triggered by a signal from the pick-up coil of the tuning fork chopper. The timer-gater can be adjusted such that one counter corresponds to the signal plus background and the other to the background signal only. For time-of-flight measurements, the output pulses are fed into a 255 multi-channel scalar which is interfaced to

a Nova 2 minicomputer. A program controls acquisition and deconvolution of the data. For surface residence time measurements, the output pulses are fed into the multi-channel scalar which is triggered by a signal from the pick-up coil of the tuning fork chopper. The signal waveforms are obtained in this manner and the residence time as well as the reaction mechanism can be extracted.

The apparatus was used to measure the angular and TOF distributions of NO scattered from Pt(111), which will be described in Chapter 4 and D_2 oxidation reaction on Pt(111) (6). While performing these experiments, we noticed several drawbacks with the apparatus leading us to modify extensively the apparatus, especially the detector and the rotating mechanism. The main drawbacks were as follows: (1) The UTI 100C mass spectrometer had low sensitivity and could not resolve masses 2, 3 and 4 sufficiently well. An Extranuclear mass spectrometer was needed to study H_2-D_2 exchange reactions. (2) The capacitance of the RF power line inside the vacuum varied as one rotated the detector, thus, the sensitivity of the mass spectrometer was not constant with respect to the angle of detection. (3) The flexible high voltage power lines arced frequently. (4) The distance between the electron multiplier and the discriminator was too long (2 feet), and so the noise pickup was high. This noise was found to be due to the transients on the A.C. power line caused by switching high current equipment in the building.

2.3 Modifications

2.3.1 General Description. A schematic diagram of the modified
TOF apparatus is shown in Fig. 2. The major modifications are in the
detector and the rotating mechanism. The old detector, the movable
part of the bell jar, and the ion pump were removed. The new detector
is two-stage differentially pumped and mounted on a 24" O.D. rotatable
flange. The rotatable seal is a modification of a differentially
pumped seal described in the literature (7). With this design, the
TOF detector can be easily replaced with the two photon ionization
(TPI) detector, constructed on another 24" rotatable flange, used for
internal energy distribution measurements (see Chapter 4). The new
TOF detector is capable of accommodating a high resolution, high
sensitivity Extranuclear mass spectrometer. The flight path is
designed to be as long as possible and is 14.4 cm. The single
sequence cross-correlation chopper disc is replaced with a double
sequence chopper, thus, the velocity resolution is doubled with same
chopper turning speed.

The modified detector has been found to eliminate most of the
drawbacks of the old detector. Some of the results of the H_2-D_2
exchange reaction and H-D reaction studies will be presented in
Chapters 5 and 6. We have found the reliability to be high, with no
noise pickup, and no high voltage arcing in the vacuum. The mass
spectrometer separates masses 2, 3, and 4 perfectly, and the time
resolution has been improved from 22µs per channel to 13µs per

channel. These improvements are very crucial to measure the TOF of the high velocity HD molecules.

2.3.2 <u>UHV Compatible Rotatable Flange Seal</u>. The fixed section of the rotatable seal has the seal surfaces and differential pumping channels on one side and a male Perkin-Elmer 18" (ID) wire seal flange on the other side to seal against the existing female flange on the main scattering chamber. A drawing of this fixed section is shown in Fig. 3. Three spring loaded Teflon seals of 18", 20" and 22" ID (Fluorocarbon Mechanical Seal Divison AR314E18000, AR314E20000, AR314E22000) are used to seal the chamber. The channel between the inner and the center seals is pumped by an 8 l/s ion pump and the outer channel is pumped by a mechanical pump. A 24" OD heat hardened stainless steel washer is used as a thrust bearing. Six cam bearings are placed around the circumference of the rotatable flange to allow adjustment of the center of rotation of the rotable flange. Four additional cam bearings hold the back face of the rotable flange to prevent it from falling off in case of vacuum loss.

The 1.9" by 24" OD rotatable flange is shown in Fig. 4. The 13.25" flange welded onto the 24" flange is used for mounting the detector. The seal surface was machined to approximately 8 μm R.M.S. finish after the 13.25" flange was welded into place. Thus, any irregularity on the seal surface caused by the welding process is eliminated. Within the 13.25" flange are two 4" ports for the mass spectrometer and the pump, and two 1.5" ports for the ionization gauge and the LN_2 cooled titanium sublimator. Between the seal surface

and the 13.25" flange, are several ports for the detector buffer pumping, electrical feed through, the cooling water supply for the chopper motor, and the detector gating mechanism. One 4.25" flange connects the buffer chamber with its pump through a stainless steel bellows. The rest of the flanges, consisting of three 6", six 2.75", and two mini flanges, are welded on the back of the rotatable flange. An U shape bracket is welded on the back surface through which the rotatable flange is mounted to a movable carriage for removing the detector from the scattering chamber.

2.3.3 _Detector._ The detector can, shown in Fig. 5, is constructed on a 13.25" flange through which it is mounted to the rotatable flange. One section of the wall of the detector can is extended by .5" to increase the flight path. The detector is two-stage differentially pumped and the buffer chamber is connected to the rotatable flange through a stainless steel bellows on a 4.25" flange. A mini-conflat flange is welded onto the wall along the beam line for the window used in the initial alignment of the detector. The alignment of the first aperture (between the scattering chamber and the buffer chamber) and the second aperture (between the buffer chamber and the mass spectrometer chamber) is done as follows:

(a) The helium-neon beams along the incident beam paths are aligned first and the rotatable flange is adjusted such that it rotates with respect to the point where the two laser beams cross.

(b) The detector is constructed as accurately as possible and two 0.25" holes are machined at the aperture positions. Two transparent,

marked papers are attached to the first aperture and the mini-conflat flange. With the detector can mounted on the rotatable flange, the system is pumped down, and the detector is rotated to the direct beam position. The primary laser beam spots are identified on the papers. The spot on the first aperture paper is the exact position of the first aperture.

(c) The detector can is then removed and mounted on a lathe and the laser spots on the paper are noted before removing the papers. A metal disk is press-fitted to the 0.25" hole at the first aperture and a 0.050" hole is drilled at the position of the laser spot. Thus, the first aperture is well aligned. The same procedure is used for a mini-conflat blank flange with .125" hole.

(d) The second aperture is aligned by having a straight rod pass through the first aperture and the hole on the mini-conflat flange. A stainless steel circular sheet with a .105" beam hole is positioned by the rod and bolted to the second aperture wall by 4 screws. Thus, the first aperture, second aperture, and the hole on the mini-conflat flange are colinear and the detector has been aligned.

The buffer chamber is pumped with a 60 l/s ion pump mounted on the back of the rotatable flange. The mass spectrometer chamber can be pumped with a cryopump or a 60 l/s ion pump also mounted on the back of the rotatable flange. To mount the cryopump, the cryopump panels have to be detached and mounted from the seal surface side of the rotatable flange after the pump body has been attached to the rotatable flange. Thus, the detector can has to be removed in order to mount or

remove the cryopump. This is also true for the mounting or removing of the LN_2 cooled titanium sublimator which is mounted through a 2.75" flange. At present, the ion pump is used to pump the mass spectrometer chamber to a background pressure of 4×10^{-10} Torr.

To help venting and rough pumping of the system, a .25" tube connects the buffer ion pump and the main scattering chamber and can be opened or closed by a Nupro bellows valve. A linear sliding gate on the first aperture has been constructed to separate the detector and the main scattering chamber. This gate is always closed except during data accumulation to keep the detector in the best possible vacuum.

2.3.4 Mass Spectrometer. The mass spectrometer, Fig. 6, is mounted on an 6" conflat flange with 18 electrical feedthroughs. The ionizer is modified from the pre-existing one described in references (1,2). The top and back plate Faraday cages and the anode are insulated from each other; thus, different voltages can be applied to increase the ionizer sensitivity. The focus plates were replaced with two electrostatic quadrupole lens pairs (8) for focusing of the ion beam. The distance from the top of the housing of the quadrupole mass filter to the filament of the ionizer is about 1.65". The quadrupole mass filter and its power supply are Extranuclear models (4-324-9 and O-11-12). The ion flight path is about 11.65". The electron multiplier is also supplied by Extranuclear (Model 051-72) and is particularly good for ion counting. Note that the electron multiplier is 0.5" off-axis from the mass filter to reduce noise caused by photons

and metastable neutrals, produced in the ionizer, striking the multiplier.

The whole mass spectrometer is then mounted on a supporting bracket which is mounted on the 6" conflat flange. Within the supporting bracket, a stainless steel tube, mounted on the 6" flange, is used to shield further the signal line from the electron multiplier to the flange. To increase the time-of-flight path, the bracket is .5" off the center of the 6" flange, thus, the center of the ionizer is off-set 1" from the center of the 6" flange. Because of this design, to mount the mass spectrometer onto the rotatable flange, it is necessary to rotate the mass spectrometer by 90°, move it into the detector chamber until the two 6" conflat flanges touch, and then rotate the mass spectrometer 90° back such that the mass filter can will fit into the notch of the detector can.

The alignment of the mass spectrometer is done as follows: With the detector can mounted on the rotatable flange which is mounted on the movable carriage, a helium-neon laser is adjusted such that it passes through the first and the second apertures. Having everything else fixed, the detector can is removed and the mass spectrometer is mounted. The ionizer was found to be about 0.125" out of alignment and has been corrected by cutting one side of the supporting bracket to an angle. Thus, the orientation of the bracket should be noted when the mass spectrometer has to be disconnected from the 6" flange.

2.3.5 Motor Mount and Chopper

A new water cooled copper block has been built to house and cool the motor more efficiently than the existing copper cylinder. The copper block is mounted on a rectangular bracket which is mounted on a second rectangular bracket and all the mountings are through teflon washers. Thus, the motor floats on eight teflon washers which are supported by the second bracket mounted to the detector chamber wall. The copper block cooling water tubes are connected to feedthroughs mounted on the rotatable flange by two bellows to prevent the copper tubes from breaking due to vibration.

Because of the low mass of the HD molecule, its velocity is high, thus, the flight time is short. Therefore, it is important to have a long flight path and better time resolution. The chopper is positioned as close (1") to the crystal as possible to increase the flight path. The diameter of the chopper had to be reduced from 8" to 7.4" to prevent the chopper from touching the chamber wall while the detector was positioned for the direct beam TOF measurement. To improve the time resolution, a chopper blade was made (Fig. 7) with two identical sequences, each consisting of 255 elements. The blade was made from .005" stainless steel using photoetching techniques instead of machining. In spite of the accurate cutting obtained by photoetching, some errors are still present and the chopper has to be dynamically balanced. Although the chopper can spin at 300 Hz after the balancing, we spin it at about 150 Hz, which corresponds to $13\mu s$ per channel time resolution, to increase the life time of the UHV compatible bearing.

2.4 Surface Characterization with Helium Beam Scattering

In addition to using Auger Electron Spectroscopy (AES) and Low Energy Electron Diffraction (LEED) for surface characterization, one can use helium beam scattering to check the cleanliness of a flat single crystal (9) and the orientation of stepped single crystal surfaces (10). Although the apparatus is not specially designed for the helium scattering experiment, and its incident beam is not extremely monoenergetic, the technique can be applied for further surface characterization.

Figure 8 shows the angular distribution of the scattered helium atom from a Pt(111) surface at a substrate temperature of 880K. The full width at half maximum (FWHM) of the distribution which is peaked at the specular angle is below 2°, approximately the resolution of the detector. To see how the angular distribution changes when the surface is contaminated by some adsorbate such as NO molecules, a He–NO mixture is used as the incident beam and the angular distribution of the helium atom is measured as the function of the crystal temperature. While all FWHM of the angular distributions are below 2° for the crystal temperature varying from 475 to 1110K, the intensity of the peak increases from 475 to 850K and decreases above 850K as shown in Fig. 9. As will be shown in Chapters 3 and 4, the NO has high sticking coefficient (~.8) on the Pt(111) surface. The increase in the intensity of the peak from 475 to 850K surface temperature is due to decreasing of the NO coverage. Above 850K, the decrease of the He

intensity with increasing temperature is probably due to the Debye-Waller factor.

The above results clearly demonstrate that helium scattering can be used to monitor the cleanliness of the surface. This technique is exclusively surface sensitive, non-destructive and especially useful for detecting hydrogen (deuterium) contamination which cannot be detected with Auger Electron Spectroscopy. Recently, Poelsema et al. have used the technique to study the interaction of hydrogen with the stepped platinum surface (11). They have found that the method enables discrimination between step edge and terrace properties in a direct geometrical way.

The angular distribution of helium scattered from a stepped Pt(557) surface is shown in Figs. 10 and 11. The substrate temperature is 915K and the helium beam is incident along the step edges for Fig. 10. As one can see that the FWHM is about 20° while the angular resolution of the detector is still about 2°. This sharp increase of FWHM as compared with that scattered from the flat Pt(111) surface is partially due to the existence of the step and mainly due to out-of-plane detection. Since the detector is mounted in the plane defined by the macroscopic normal and the incident beam, it does not sample molecules scattered out-of-plane. Since the incident beam comes in along the step edges, the specular angle of the terrace is out-of-plane, thus, the detector "sees" only slices of the scattering distribution.

In Fig. 11 the incident beam comes in perpendicuar to the step edges from the shadow side. The diffraction feature is clearly observable. In addition to peaks at the terrace specular (Ts) and macroscopic specular (Ms), the shoulder near 57° is a reproducible feature. The relationship between the Ts, Ms and the angle of cut from the (111) surface is shown in Fig. 12. The majority of the helium is scattered to the terrace specular rather than the macroscopic specular, indicating that the helium atoms do indeed probe the atomic surface structure. The appearance of the peak at Ms indicates that the interaction potential surface at the upper part of the step has a finite radius of curvature unlike that shown in Fig. 12. This is reasonable since the interaction potential is determined by the electron density which cannot have sharp edges due to the quantum effects.

The above results clearly show that helium scattering from the stepped surface can be used to determine step orientation. With this method, it is very easy to identify the open side of the step. With a very monoenergetic incident beam and good angular resolution, one can observe many diffraction peaks which can be used to extract quantitative information about the helium–metal interaction potential near the step edge (10,12).

References

1. S. T. Ceyer, Ph.D. Thesis, Department of Chemistry, University of California, Berkeley, California (1979).

2. S. T. Ceyer, W. J. Siekhaus and G. A. Somorjai, J. Vac. Sci. Technol. 19, 726 (1981).

3. V. L. Hirschy and J. P. Aldridge, Rev. Sci. Instrum. 42, 381 (1971).

4. G. Comsa, R. David and B. J. Schumacher, Rev. Sci. Instrum. 52, 789 (1981).

5. W. L. Guthrie, Ph.D. Thesis, Department of Physics, University of California, Berkeley, California (1983).

6. S. T. Ceyer, W. L. Guthrie, T. H. Lin, and G. A. Somorjai, J. Chem. Phys. 78, 6982 (1983).

7. D. J. Auerbach, C. A. Becker, J. P. Cowin and L. Wharton, Rev. Sci. Instrum. 49, 1518 (1978).

8. C. S. Lu and H. E. Carr, Rev. Sci. Instrum. 33, 823 (1962).

9. H. Saltsburg, Annu. Rev. Phys. Chem. 24, 493 (1973).

10. G. Comsa, G. Mechtersheimer, B. Poelsema, and S. Tomoda, Surface Sci. 89, 123 (1979).

11. B. Poelsema, G. Mechtersheimer, and G. Comsa, Surface Sci. 111, 519 (1981).

12. J. Lapujoulade and Y. Lejay, Surface Sci. 69, 354 (1977).

Figure Captions

Fig. 2.1 Schematic diagram of the unmodified molecular beam scattering
apparatus and time-of-flight spectrometer.

Fig. 2.2 Schematic diagram of the modified molecular beam scattering
apparatus and time-of-flight spectrometer.

Fig. 2.3 Drawing of the fixed flange of the rotatable seal.

(A) Spring loaded teflon seals; (B) pumping channels;
(C) ion pump port; (D) mechanical pump ports; (E) thrust
bearing; (F) locating cam bearings; (G) chain drive; (H)
Ultek wire seal flange face.

Fig. 2.4 Drawing of the rotatable flange: (A) Seal surface; (B)
13.25" detector mounting flange; (C) port for buffer chamber
pump; (D) port for mass spectrometer; (E) port for mass
spectrometer chamber pump; (F) port for titanium sublimator;
(G) port for ion gauge; (H) port for chopper motor power, PD,
LED feedthroughs; (I) port connecting the detector and the
scattering chamber; (J) blank; (K) port for chopper cooling
and detector gating mechanism; (L), (M) blank.

Fig. 2.5 Drawing of the detector: (A) 13.25" flange; (B) first
aperture; (C) second aperture; (D) alignment window, (E,F)
4.25" flanges; (G).stainless steel bellow.

Fig. 2.6 Mass spectrometer: (A) 6" mounting flange; (B) supporting
bracket; (C) electron multiplier housing can; (D) mass filter
housing can; (E) ionizer.

Fig. 2.7 Cross-correlation chopper dics.

28

Fig. 2.8 Angular distribution of helium scattered from Pt(111) surface at 880K. The arrow on the lower axis indicates the specular angle.

Fig. 2.9 The Pt(111) scattered helium specular peak intensity as a function of the crystal temperature. The incident beam is a mixture of He/NO with ratio of 4/1.

Fig. 2.10 Angular distribution of helium scattered from the stepped Pt(557) surface at 915K. The incident beam comes in along the step edges.

Fig. 2.11 Angular distribution of helium scattered from the stepped Pt(557) surface at 905K. The beam is incident perpendicular to the step edges from the shadow side. The arrows on the lower axis indicate the terrace specular (T_s) and the macroscopic specular (M_s).

Fig. 2.12 Diagram indicating microscopic specularity for step edges perpendicular to the incident beam.
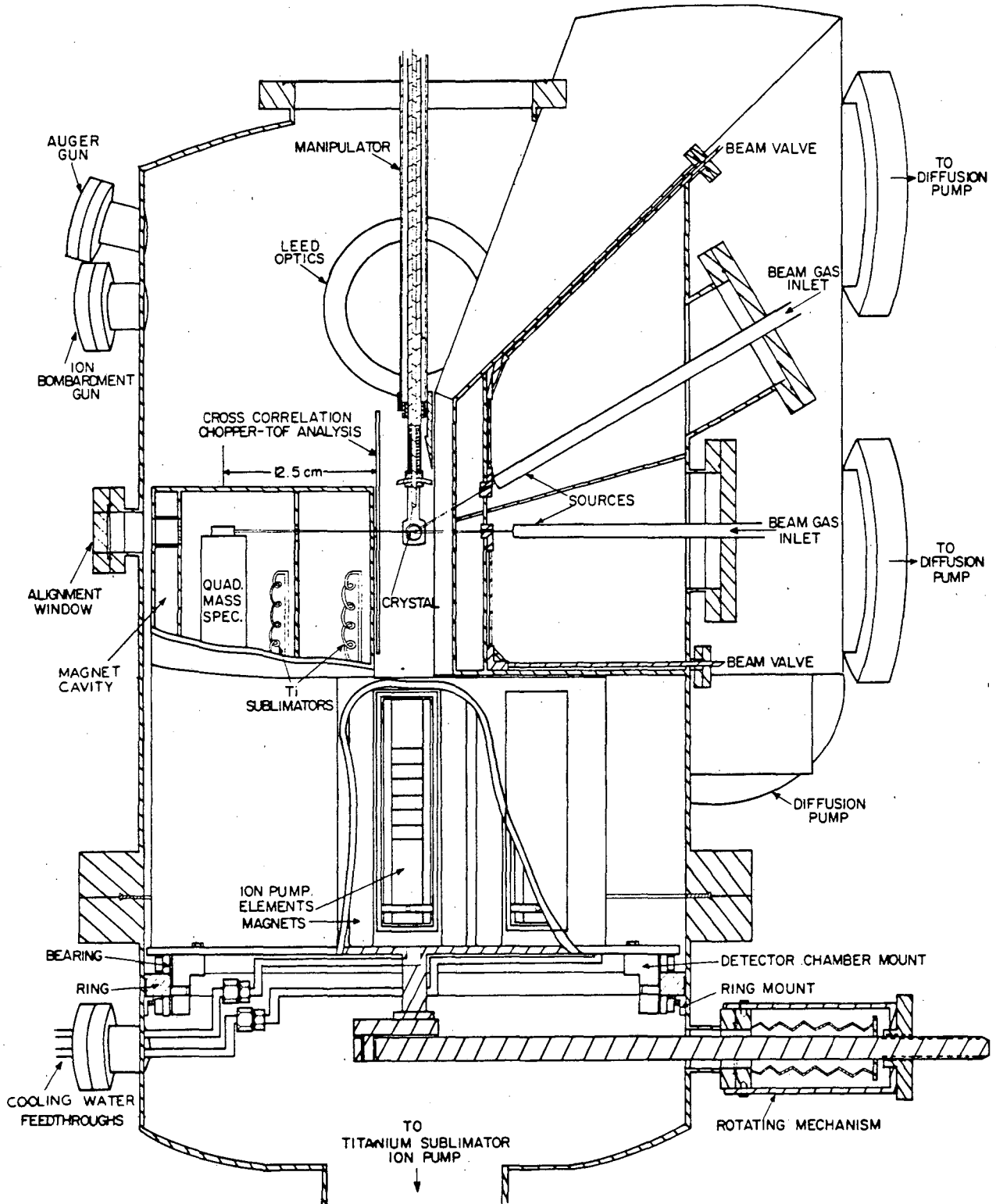
AUGER GUN

MANIPULATOR

BEAM VALVE

TO DIFFUSION PUMP

LEED OPTICS

BEAM GAS INLET

ION BOMBARDMENT GUN

CROSS CORRELATION CHOPPER-TOF ANALYSIS

SOURCES

12.5 cm

BEAM GAS INLET

ALIGNMENT WINDOW

QUAD. MASS SPEC.

CRYSTAL

TO DIFFUSION PUMP

MAGNET CAVITY

Ti SUBLIMATORS

BEAM VALVE

DIFFUSION PUMP

ION PUMP ELEMENTS MAGNETS

BEARING

DETECTOR CHAMBER MOUNT

RING

RING MOUNT

COOLING WATER FEEDTHROUGHS

TO TITANIUM SUBLIMATOR ION PUMP

ROTATING MECHANISM

XBL 799-11376

Figure 2.1

MANIPULATOR

RFA

D.P.

D. P.

BEAM 2

CHOPPER

14.4 cm

MASS SPEC.

BEAM 1

CH

D. P

T.S.P

LN₂
T.S.P.

ION
PUMP

ION
PUMP

ROTATABLE
FLANGE
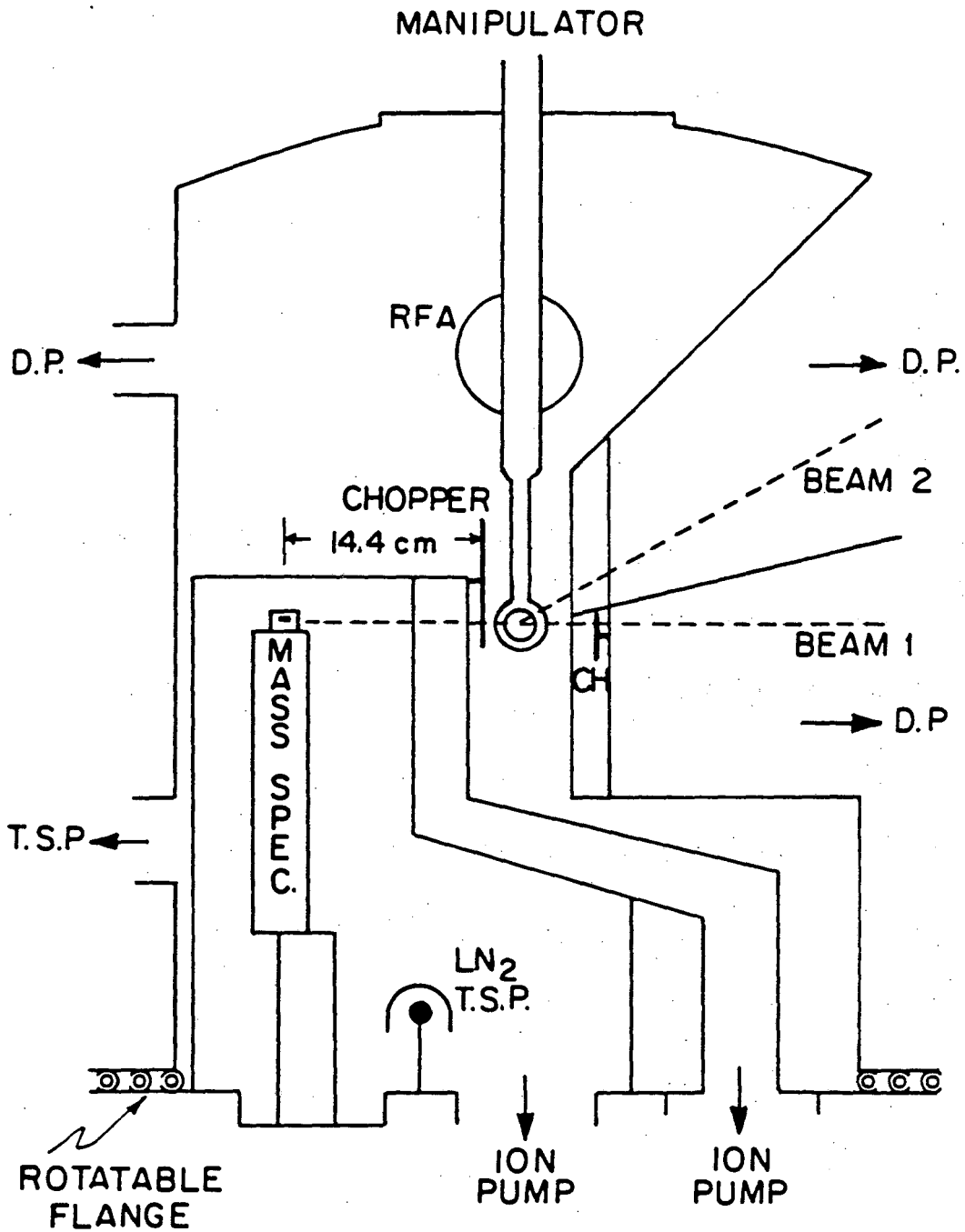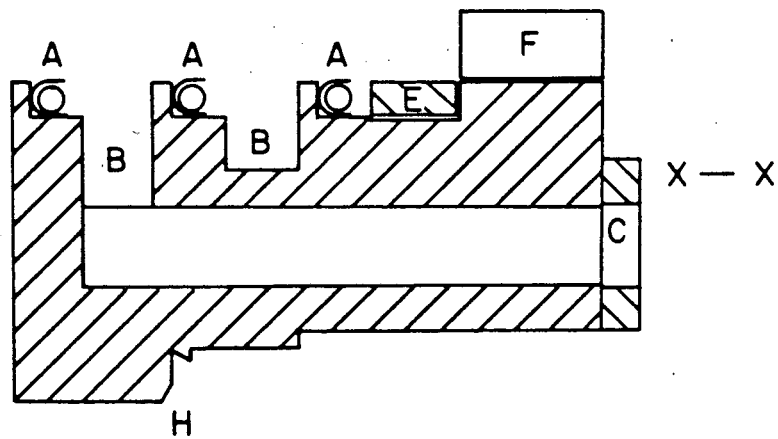
XBL 836-5873
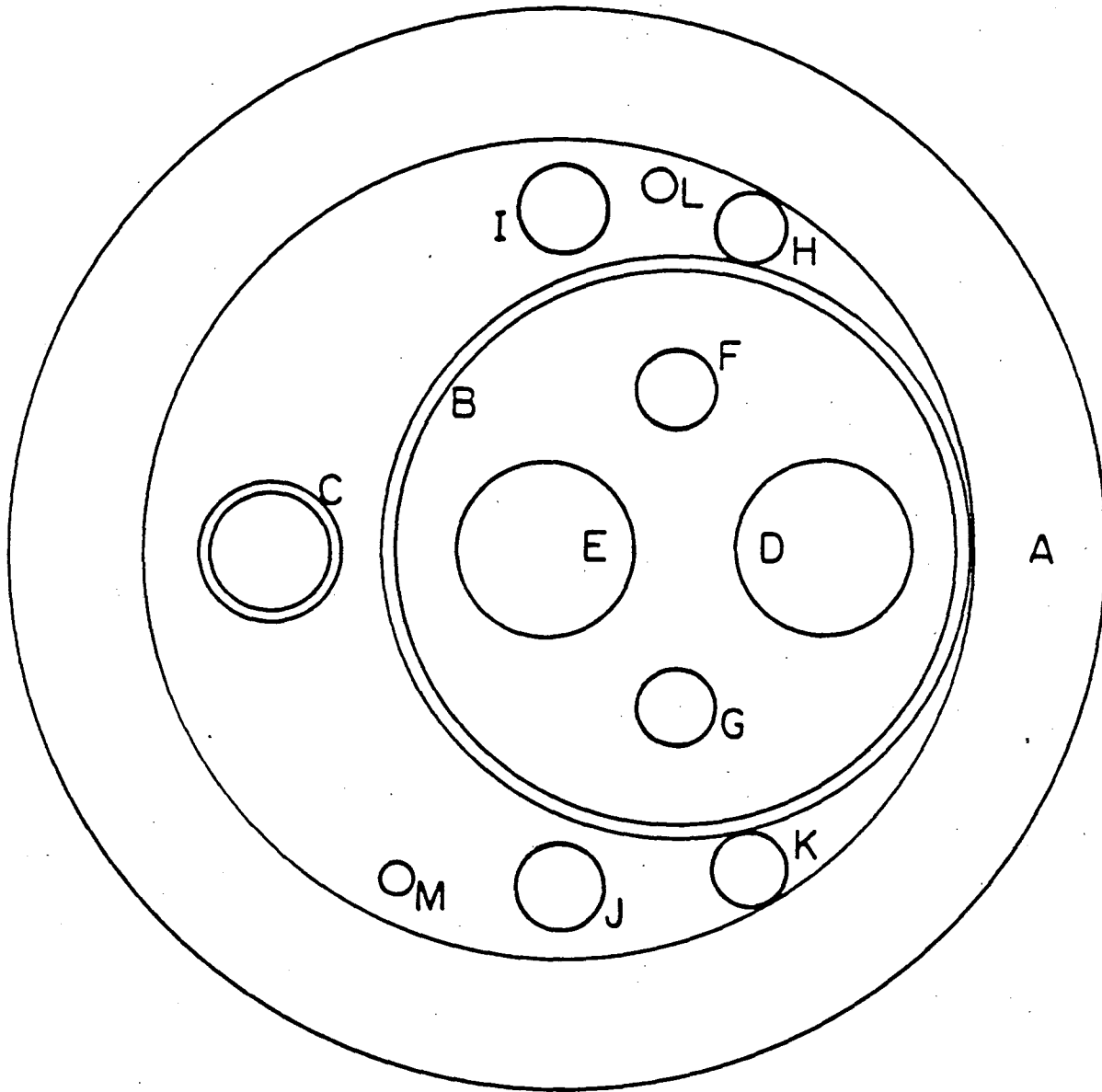
Figure 2.2

XBL 8212-12032

Figure 2.3

XBL 837-6001

Figure 2.4

B C   D

Buffer Chamber

Mass Spectrometer
Chamber

E

G

F   A
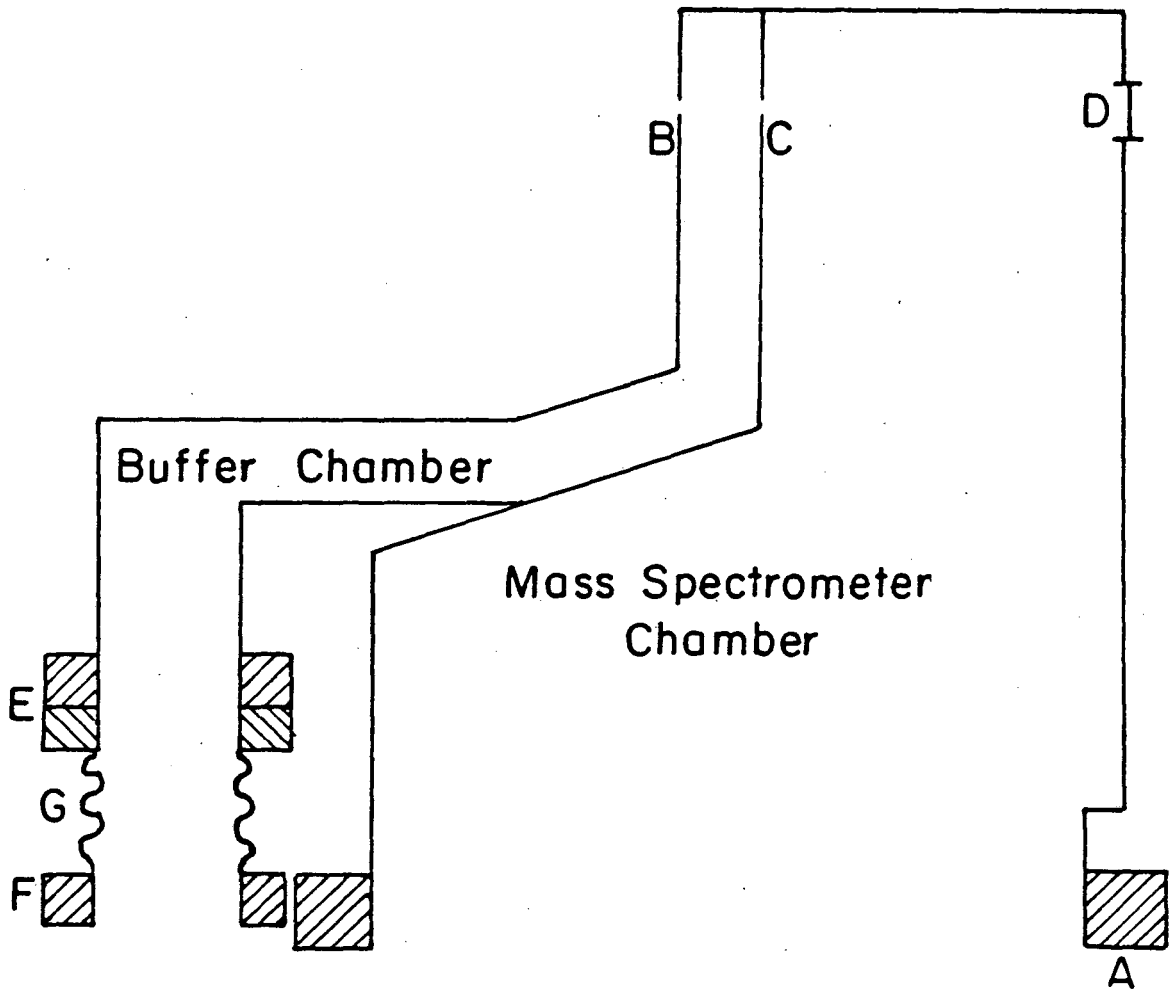
XBL 837-6002
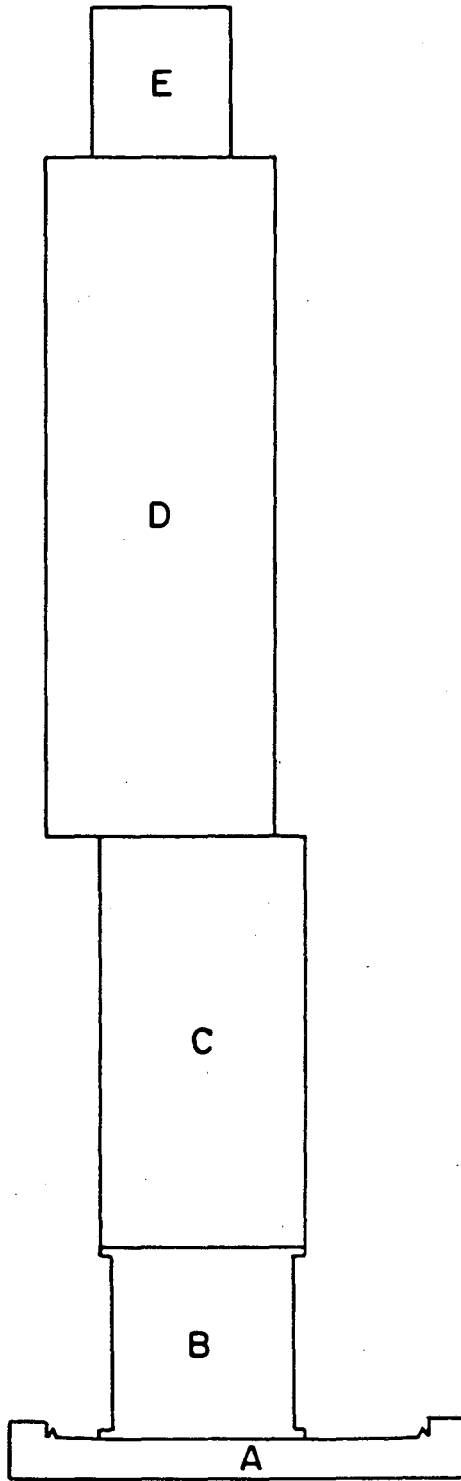
Figure 2.5

XBL837-6003

Figure 2.6

XBB 837-6123

Figure 2.7

He/Pt(III)

$T_S = 880\,K$

$\theta_i = 45°$

Intensity (a.u.)

Detector Angle (degrees)

XBL836-5888

Figure 2.8

He/NO 4:1
Pt(111)
$\theta_i = 45°$

He Peak Intensity (a.u.)

Crystal Temperature (K)

XBL 836-5889

Figure 2.9

He/Pt(557)

$T_S = 915$ K

$\theta_i = 70°$

Beam

Open Side of
Step Edges

Intensity (a.u.)

Detector Angle (degrees)
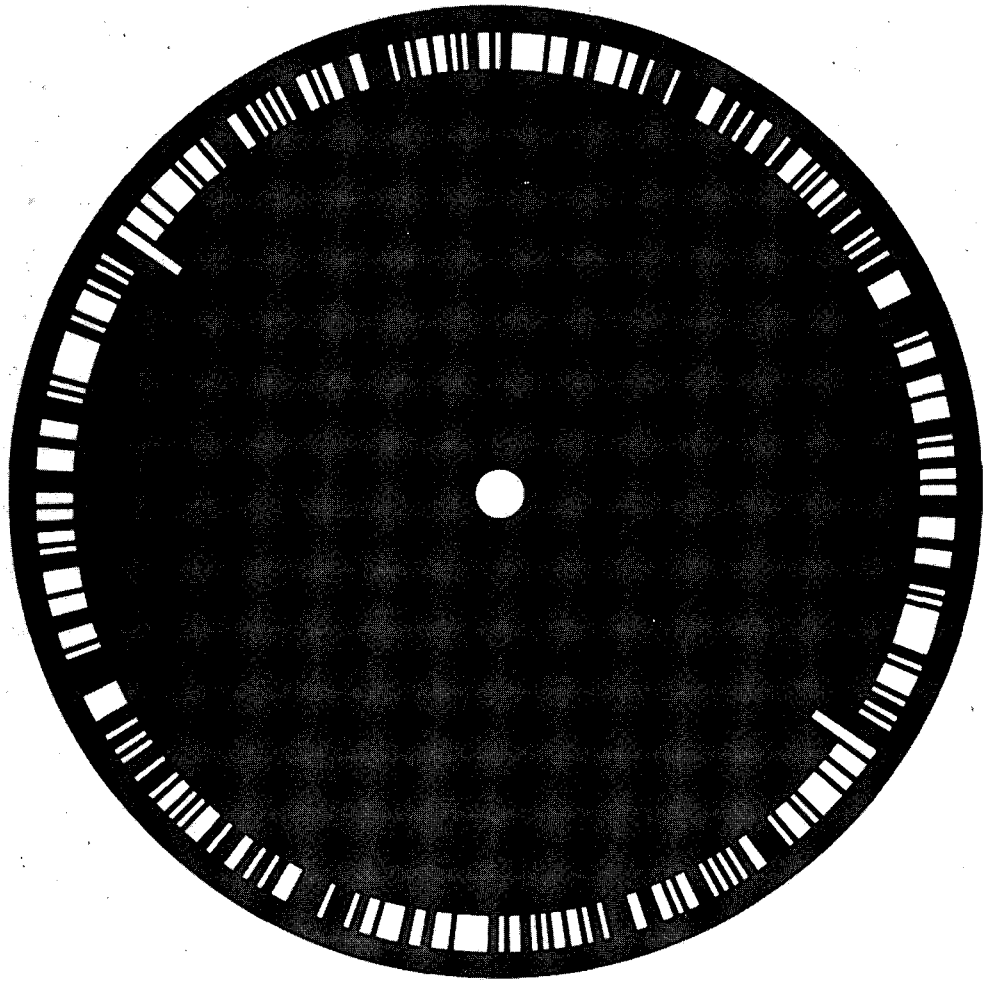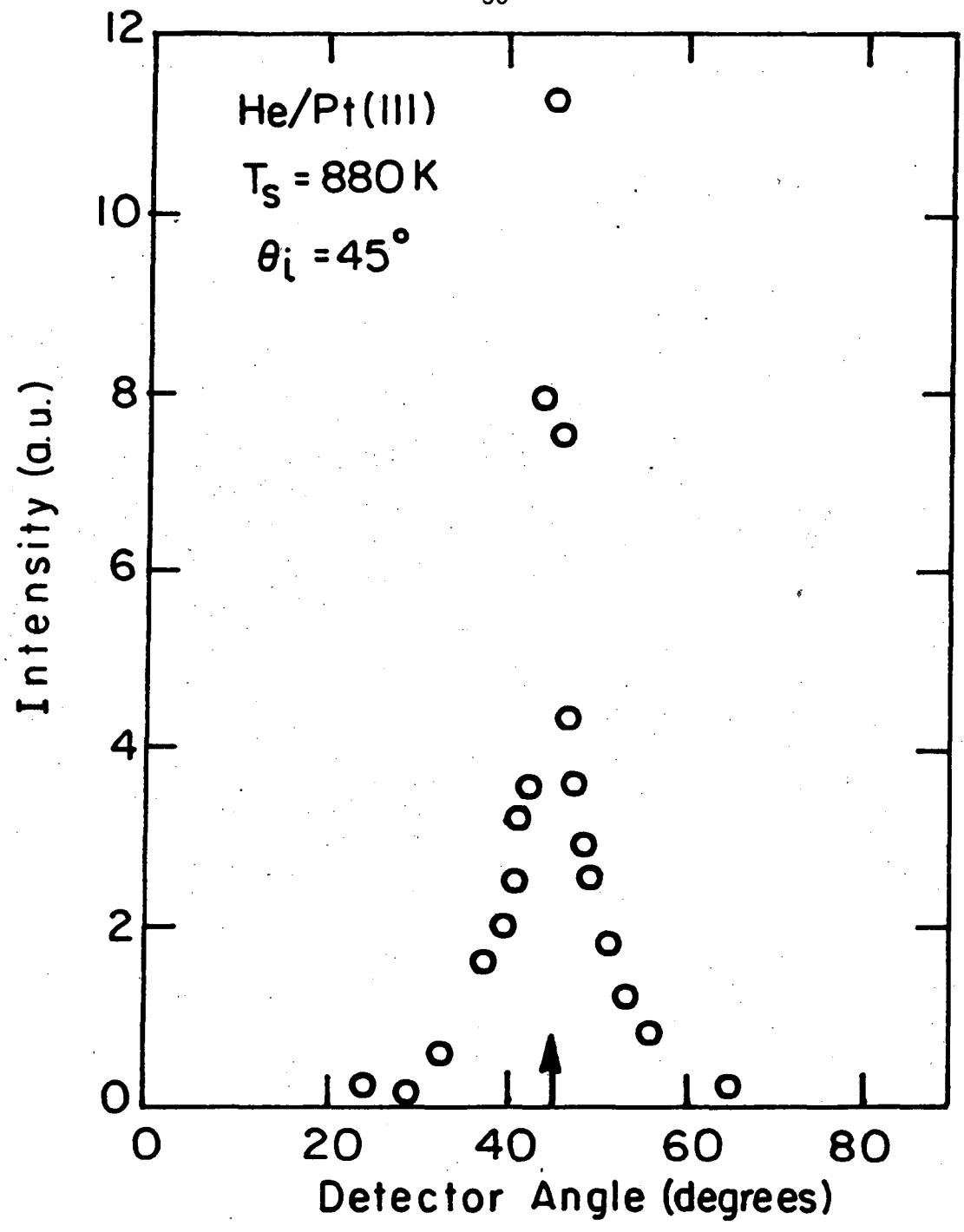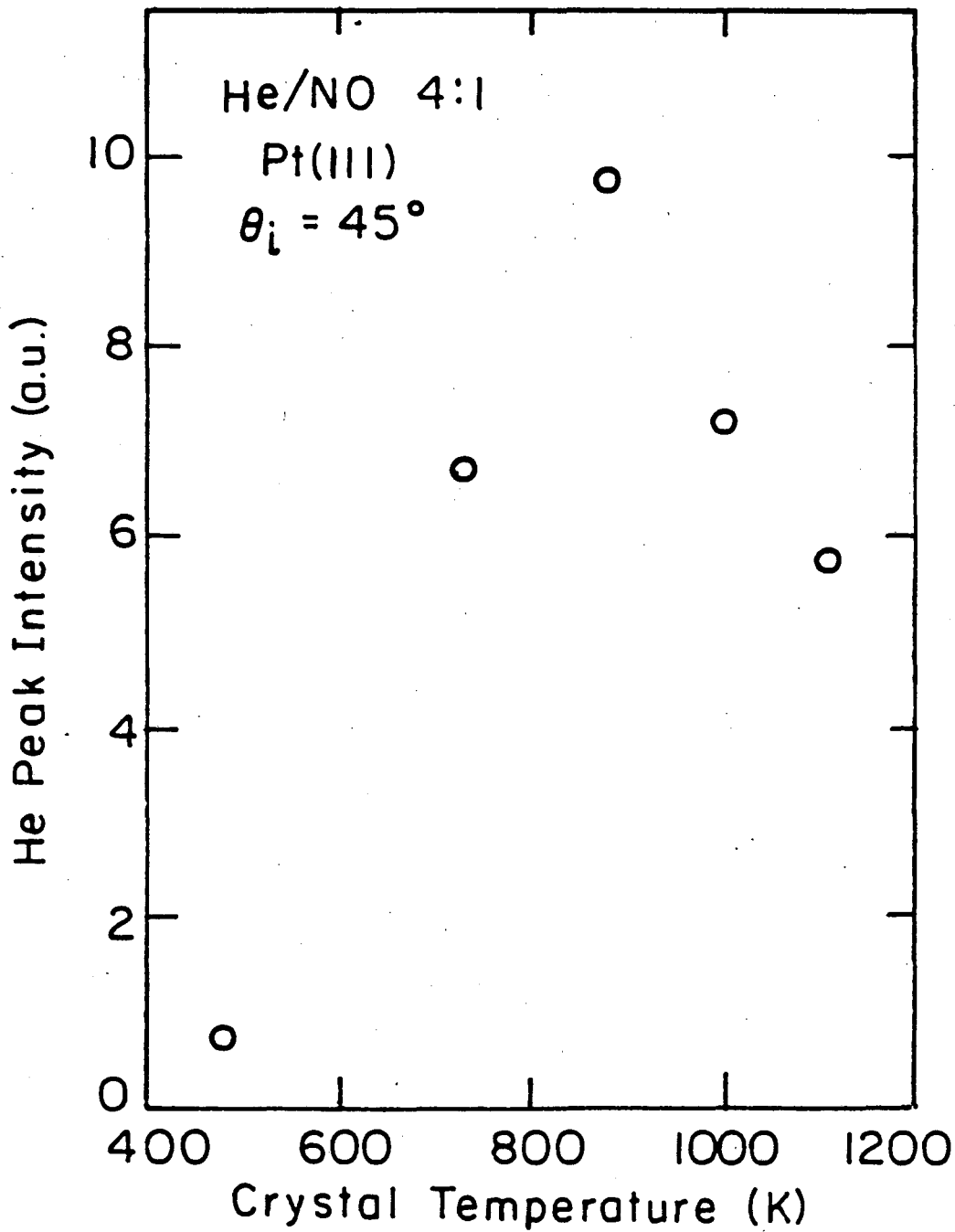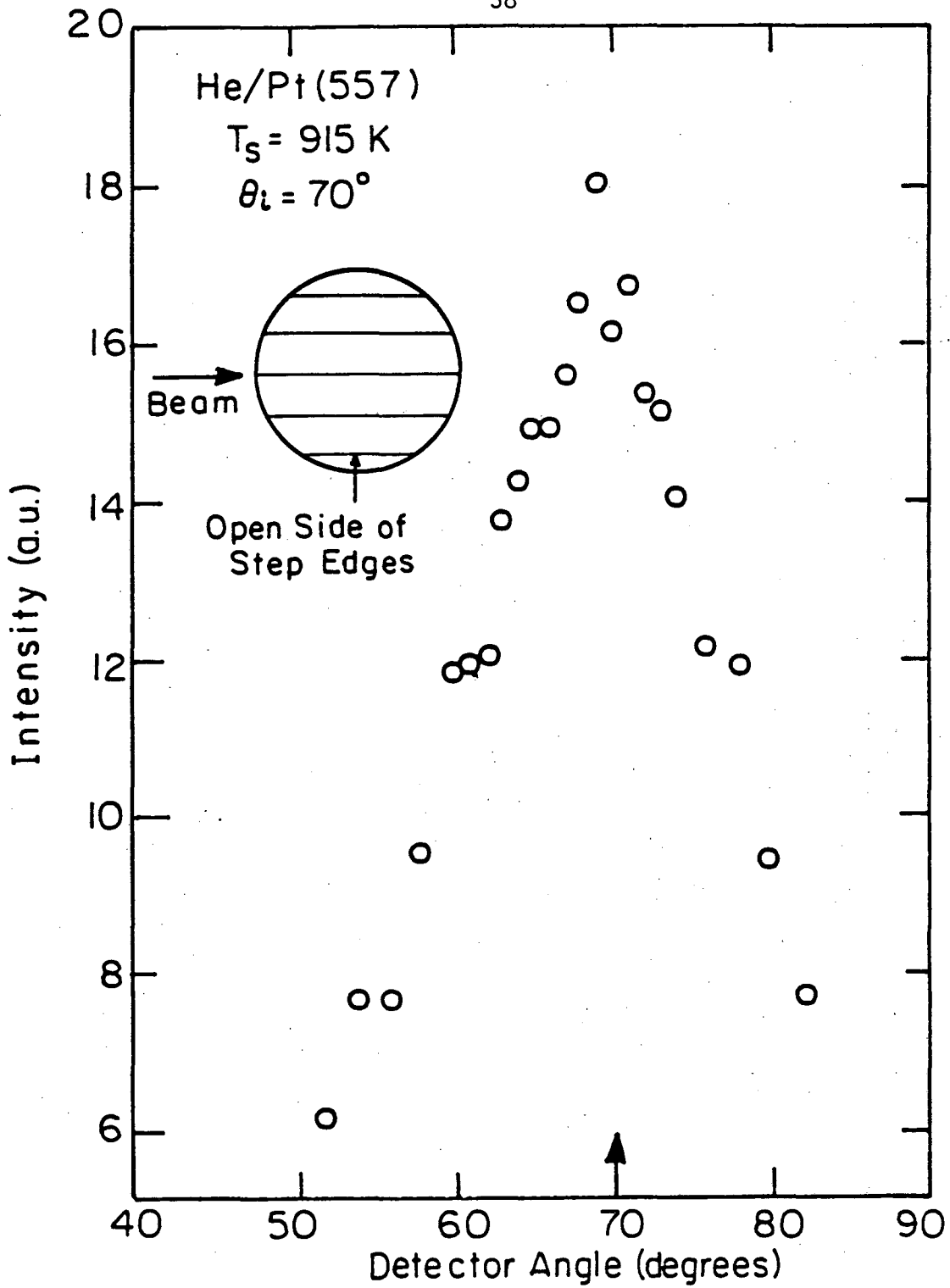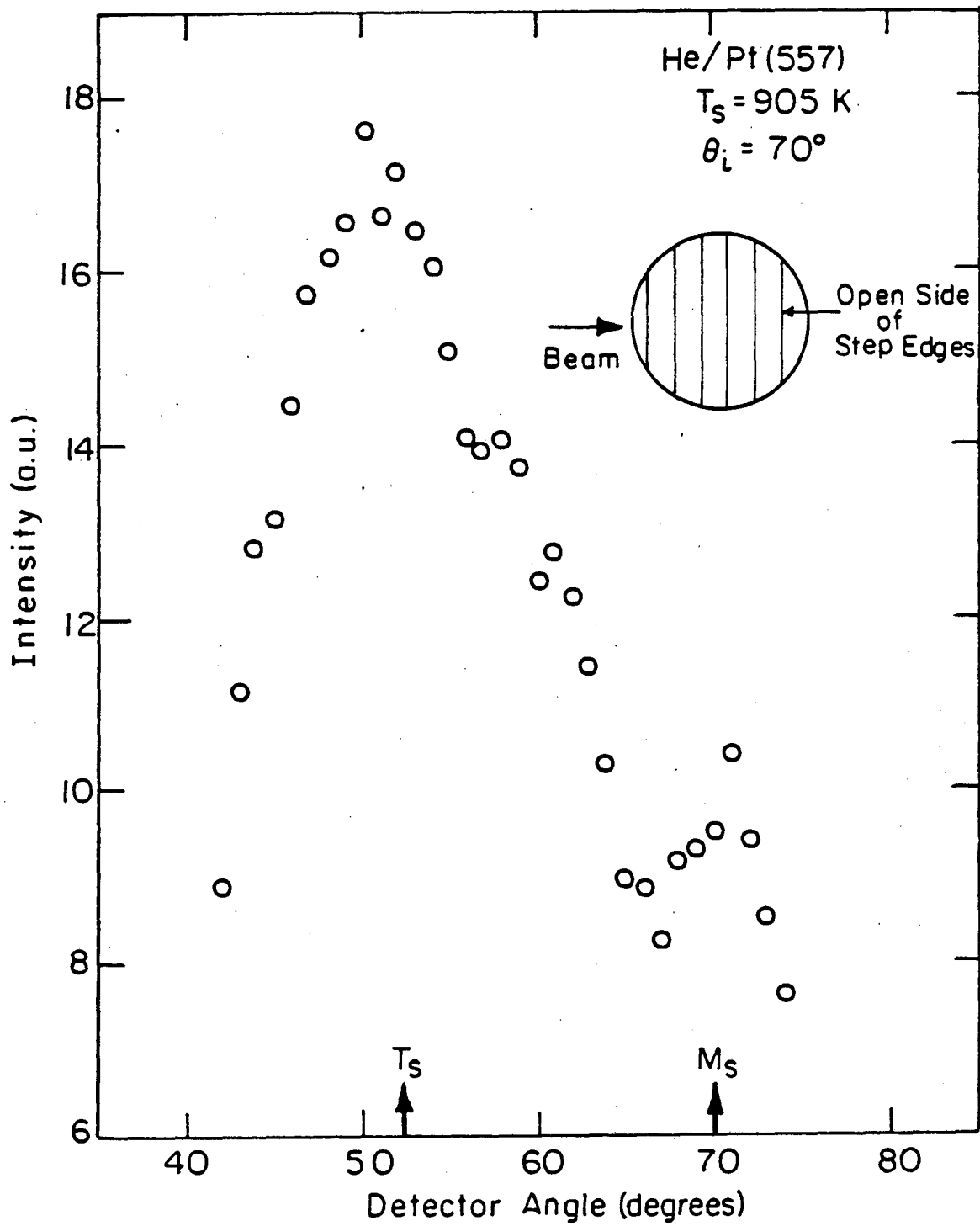
XBL 836-5890

Figure 2.10

Figure 2.11

$$\alpha + 2\gamma = \beta$$

$$2\gamma \simeq 18°$$

M_n = Macroscopic normal

T_n = Terrace normal

XBL 837-6000

Figure 2.12

CHAPTER III. MODULATED MOLECULAR BEAM SCATTERING OF CO

AND NO FROM Pt(111) AND THE STEPPED Pt(557) CRYSTAL SURFACES

3.1 Introduction

Although the interaction of NO with metal surfaces is as important as that of CO, it has not received as much attention until recently. Practically, NO is a nonequlibrium product of combustion and a serious pollutant. Scientifically, it is interesting to compare the interaction of NO and CO on metal surfaces since they have similar molecular orbital structures, but different binding energies (151 Kcal/mole for NO as compared to 256 Kcal/mole for CO). Previous investigations 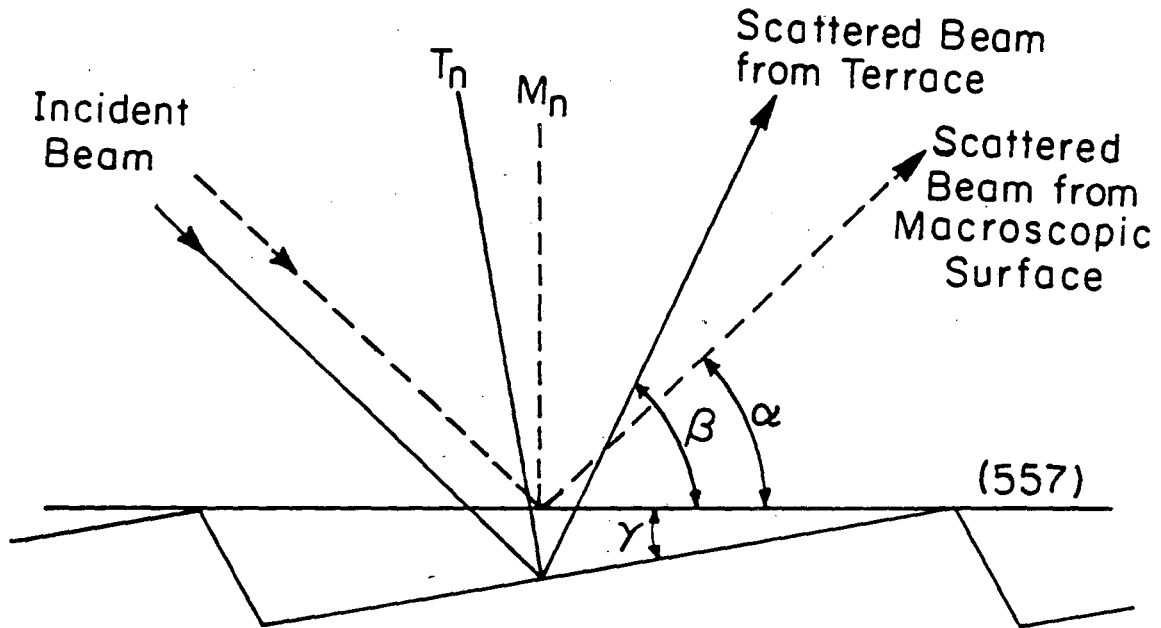of CO (1-7), and NO (8-13) on platinum surfaces mainly studied the static properties of adsorption and desorption. Briefly, CO adsorbs molecularly with carbon bonded to the surface in either the linear or the bridged configuration. The activation energy for desorption from Pt(111) is in the range of 24-33 Kcal/mole and decreases with increasing coverage (1,2). The sticking coefficient is between 0.6 and 0.8 and also decreases with increasing coverage (3,4). The NO/Pt system has been found to be more complex. For example, the appearance of various vibrational modes has been interpreted as either the occupation of different adsorption sites (11) or by the formation of adsorbed dimers (9). Partial dissociation of the molecule upon heating has been reported (8,10,11) although it is not observed here with the molecular beam technique at higher temperatures and lower coverages. It is generally believed that NO is molecularly adsorbed on platinum surfaces with nitrogen atom bonded to

metal at room temperature. The activation energy for desorption is between 20 and 28 Kcal/mole (8,10).

Nevertheless, there is little work on dynamic properties of adsorption and desorption for these two systems. The molecular beam technique offers a unique tool for this purpose and is therefore applied in this study. Here, the results of modulated molecular beam scattering of NO and CO from the flat Pt(111) and the stepped Pt(557) crystal surfaces are presented. The modeling and computational methods used to determine surface reaction mechanisms by modulated molecular beam scattering have been derived, and reviewed by other authors (14-16). We have found that while the incident NO and CO can be adsorbed at the step as well as the terrace, their desorption kinetics are completely controlled by the steps. The kinetic properties of NO/Pt are found to be very different and more complex than those of CO/Pt. Experiments of a similar nature by other investigators were performed independently, (17-20) at the same time or after this work was published (21). Essentially, similar conclusions were reached.

3.2 Experimental

The apparatus used for the experiment has been described in detail elsewhere (22). Briefly, it consists of three differentially pumped chambers as shown in Fig. 1. The first diffusion pumped chamber contains the molecular beam source. The second diffusion pumped chamber contains the slotted disk chopper used to modulate the incident beam in the frequency range of 5-200 Hz. The scattering

chamber which is pumped by an ion pump and titanium sublimator contains the crystal, the rotatable EAI mass spectrometer, and the instrumentation for Auger electron spectroscopy (AES), low energy electron diffraction (LEED), and argon ion sputtering. The mass spectrometer AC signal is processed by a phase sensitive lock-in amplifier.

Two crystal surfaces, Pt(111) and Pt(557) were used. The high Miller index surface has six atom wide terraces of (111) orientation seperated by one atom height steps with (100) orientation. The temperature of the crystal was measured by the chromel-alumel thermocouple spot welded to the edge of the crystal. Before any experiment, the crystal was ion sputtered, treated with oxygen, and annealed in situ. The cleanliness was checked by AES.

The molecular beam source backing pressure was 10 Torr for NO unless otherwise noted. Backing pressure was 3 Torr for CO. The angle of the incident beam was 45° and perpendicular to the step in the case of Pt(557). The signal was detected in the integral mode (23). In this mode of detection, the mass spectrometer is placed behind the crystal surface and measures the modulated chamber pressure. Each datum was normalized to a hot crystal (1250K) datum, which has a negligible phase lag due to the very short residence time. The normalization takes care of all other causes of phase lag (14) except that due to the surface reaction. Therefore, the normalized data depend on the surface processes only. Between each experimental run, the crystal was heated to 1250K for 3-5 minutes to

make sure that it was not poisoned during the experiment as a result of adsorption of ambient gases. At the same time, the reference signal was detected for normalization of the data points. In this way any change in the electron multiplier gain, which could be 10 percent during each day's experiment, was detected and eliminated from the normalized data. At the end of the experiment, the crystal was rechecked with AES.

3.3 Results and Discussion

3.3.1 CO Scattered from Pt(111) and Pt(557) Crystal Surfaces.

Figures 2a and 2b show the normalized amplitudes and phase lags as functions of the crystal temperature for CO scattered from Pt(111) at chopping frequencies of 10 and 100 Hz, respectively. The solid and dash lines are the theoretical fits to the adsorption-desorption model with coverage dependent sticking coefficient (see below). The normalized amplitude stays at the value of 1.0 at high temperature and drops sharply at lower temperature, then starts to climb at even lower temperature (<500K). The phase lag is essentially zero at high temperature and has a sharp peak when the amplitude drops sharply. The phase lag stays at zero at the lowest temperature range where the amplitude is climbing. Note that the phase lag peak appears at a lower temperature for a chopping frequency of 10 Hz than that for 100 Hz.

To understand how the amplitude and the phase lag vary with crystal temperature, let us consider the adsorption-desorption model with a fixed sticking coefficient S:

$$\text{A(gas)} \xrightarrow{(1-S)\ I_0 g(t)} \text{A(gas)}$$

$$\text{A(gas)} \xrightarrow{SI_0 g(t)} \text{A(ads)} \xrightarrow{k} \text{A(gas)}$$
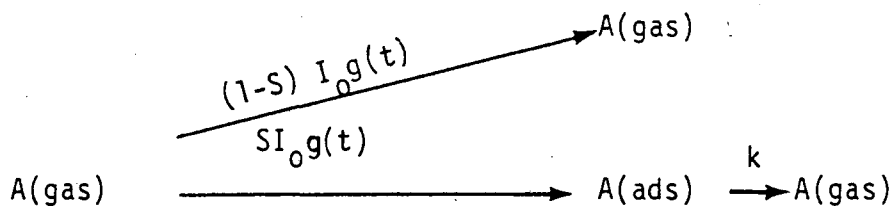
where I_0 is the unmodulated beam intensity, $g(t)$ is the gating function, and $k = \nu \exp(-E/RT)$ is the first order Arrhenius desorption rate. Since the incident beam is chopped into a square wave, it can be decomposed into Fourier series:

$$g(t) = \frac{1}{2}(1 + g_1 e^{i\omega t} + \ldots) \tag{1}$$

The concentration of the adsorbed molecules, $n(t)$, can also be decomposed into Fourier series:

$$n(t) = n_0 + n_1 e^{i\omega t} + \ldots \tag{2}$$

Substitute (1) and (2) into the mass balance equation,

$$\frac{dn(t)}{dt} = SI_0 g(t) - kn(t) \tag{3}$$

One obtains

$$n_1 = \frac{SI_0 g_1/2}{i\omega + k} \tag{4}$$

With the lock-in amplifier tuned to first harmonic detection, the measured signal is

$$MS = \frac{SI_o g_1/2}{i\omega+k}\, k + (1-S)\, I_o\, \frac{g_1}{2} \qquad (5)$$

The normalized signal, NS, is the signal divided by the high temperature signal, which is $I_o g_1/2$; thus,

$$NS = \epsilon\, e^{-i\Delta\phi} = \frac{kS}{i\omega+k} + (1-S) \qquad (6)$$

where the first term is due to the fraction of molecules that stick and then desorb from the surface and the second term is contributed by the fraction that does not stick at all. The first term gives rise to the phase lag and its amplitude approaches zero if $k \rightarrow 0$ due to the long (compared with the chopper frequency) residence time of the molecules that stick, i.e. chemisorb on the surface. In other words, the long residence time caused the phase lag as well as the demodulation of the signal. The second term gives rise to no phase lag since the molecules do not stay on the surface long enough. This fraction of the molecules are those inelastically scattered.

At high temperature, $kS/(k+i\omega) \simeq S$ since $k \gg \omega$, NS equals 1 and has zero phase lag. At very low temperature, $kS/(k+i\omega)$ has negligible amplitude and $90°$ phase lag since $k \rightarrow 0$. However, the sum of $kS/(k+i\omega)$ and $1-S$ will be approximately equal to $1-S$ which has no phase lag either. At certain intermediate temperature where k is

comparable to ω, $kS/(k+i\omega)$ will have finite phase lag and amplitude, so does the sum of $kS/(k+i\omega)$ and $1-S$. Therefore, there will be a temperature where the phase lag is largest and the amplitude will vary from 1 to 1-S as temperature decreases. For a set of fixed ν, E, and S, the phase lag peak position will appear at lower temperature for the smaller chopping frequency, ω.

The adsorption-desorption model with fixed sticking coefficient can explain the general scattering behavior in Fig. 2, except the rising amplitude below 500K. A computer least square fit without using the rising amplitude data gives $\nu = 2.9 \times 10^{13}$, E = 29.9 Kcal/mole, and S = 0.737.

Figures 3a and 3b show the results of CO scattered from Pt(557). The curves are the theoretical fits to the adsorption-desorption model with coverage dependent sticking coefficient (see below). The general features of the data are the same as that scattered from Pt(111). For the same chopping frequency, the phase lag peak appears at higher crystal temperature for Pt(557) than that for Pt(111), indicating that the desorption energy will be higher in the case of Pt(557). The computer fit, without using the rising amplitude data, to the adsorption-desorption model with fixed sticking coefficient gives $\nu = 7.9 \times 10^{13}$, E = 33.6 Kcal/mole, and S = 0.74.

Note that the data show only one binding state of CO for Pt(557), which is a stepped surface and should have at least two states--at the terrace and step sites. Since the sticking coefficients are about the same for both Pt(111) and Pt(557), we believe the molecule can be

adsorbed at the step as well as the terrace site with about the same probability. If the desorption rates are different for these two sites and the molecule does not diffuse from the terrace to the step or vice versa, one should obtain curves more or less like that of Fig. 4. The excellent fit with the simple adsorption-desorption model and the higher activation energy suggest that while CO can adsorb on both the step and terrace sites, its desorption kinetic is completely controlled by the step sites on the stepped surface. Thus, for those molecules adsorbed on the terrace sites, they have to visit the step at least once before they desorb, and the kinetic parameters determined are for desorption from the step sites. However, it is unknown whether the desorption occurs directly from a step site or the adsorbed molecules have to diffuse to the terrace and then desorb.

Some more explanations are needed for the fact that the stronger bonding step sites control the whole kinetic of desorption. As one can observe only the higher energy binding state by thermal desorption spectroscopy at low coverage, we can also see the tightly binding state only at low coverage by molecular beam-surrface scattering as long as the adsorbed molecules are highly mobile. This is also concluded independently by other authors with a similar technique (17-20). While the temperature is low enough that the step sites are completely occupied, the adsorbed molecules on the terrace could be almost completely demodulated. We believe this is the reason that we cannot observe clearly the desorption from the terrace at high coverage range. Recently, Gdowski and Madix intentionally poisoned the step

sites with sulfur and found very different kinetic parameters, 1×10^{15} exp $(-36.2/RT)$ for the clean surface and 1×10^{13} exp$(-27.5/RT)$ for the step sites blocked by sulfur [18]. As will be discussed later, the NO desorption rate is found to be strongly dependent on oxygen contamination (<1 percent) on Pt(111) [20].

To explain the rising amplitude at low temperature, we used a coverage dependent sticking coefficient instead of a fixed sticking coefficient. In this model,

$$S = S_0(1-\theta), \quad \theta = n/N, \tag{7}$$

where S_0 is the initial sticking coefficient, n is the concentration of CO on the surface and N is the density of the available site for CO chemisorption. The way of treating this non-linear process has been described by Olander et al. [16]. Briefly, by substituting (1) and (2) into the mass balance equation

$$\frac{dn}{dt} = S_0 I_0 g(t)(1-\theta) - kn . \tag{8}$$

We obtain

$$n_0 = \frac{S_0 I_0}{2} \frac{1}{k + S_0 I_0/2N} , \tag{9}$$

$$n_1 = \frac{S_0 I_0}{2} g_1 \left(1 - \frac{n_0}{N}\right) \frac{1}{i\omega + k S_0 I_0/2N} . \tag{10}$$

The normalized signal, NS, becomes

$$NS = \epsilon \, e^{-i\Delta\phi} = (1-S_0) + S_0 \left(\frac{n_0}{N} + \frac{n_1}{Ng_1}\right) + k \left(\frac{n_1}{g_1}\right) \frac{2}{I_0} \quad , \qquad (11)$$

which has four fitting parameters: S_0, ν, E, and I_0/N. The best fit is shown by curves on Figs. 2 and 3. The values of the best fitting parameters are, $\nu = 2.1 \times 10^{13}$, $E = 29.5$ Kcal/mole, $S_0 = 0.73$, $I_0/N = 0.0031$ for Pt(111), and $\nu = 4.3 \times 10^{13}$, $E = 32.8$ Kcal/mole, $S_0 = 0.73$, $I_0/N = 0.0002$ for Pt(557). It is evident that the values for ν, E and S_0 are almost identical for both models for each surface.

The values of ν, E and S for both Pt(111) and Pt(557) are in the range of values reported by other authors (1-4). The coverage dependent sticking coefficient has also been reported (3,4). However, the temperature range we use is generally not accessible by those who use TDS. Therefore, our results provide complimentary information. The fit between the data and the model is very good for both Pt(111) and Pt(557) except in the low temperature range. Even for Pt(111) we do not expect the simple function of the coverage dependent sticking coefficient to fit the data well at low temperature. To have a good fit in that region we believe that a more compliated function of the coverage dependent sticking coefficient has to be chosen.

Note that the adsorbed CO must be highly mobile on Pt(111) since surface diffusion is not the limiting step in our temperature range. Ibach et al. (24) pointed out that the preexponential factor can be

near 10^{13} for mobile surface species, which is what we find. For Pt(557), the mobility of the adsorbed molecule is reduced due to the presence of the steps. We believe this is the reason that we obtain a somewhat higher preexponential factor for Pt(557) than that for Pt(111). We also find similar structure sensitive behavior for NO scattered from Pt(111) and Pt(557) as will be shown below.

3.3.2 <u>NO Scattered from Pt(111) and Pt(557) Crystal Surfaces.</u>
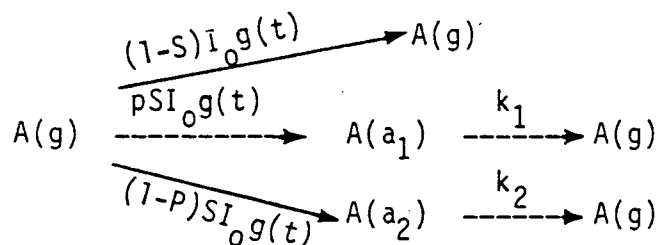
Figures 4a, 4b and 4c show the normalized amplitude and phase lag as a function of the crystal temperature for NO scattered from Pt(111) at 5, 10, and 100 Hz chopping frequencies. The curves are the theoretical fit obtained from our model which will be described later. Many features of the phase shift and amplitude data are quite different from those for CO scattering, especially at 10 and 5 Hz chopping frequenies.

Above 525K, the data behave like that predicted from the adsorption desorption model with fixed sticking coefficient. Fitting those data to the model gives $\nu = 6.2 \times 10^{13}$, E = 28.6 Kcal/mole, and S = 0.645. The activation energy is close to what have been published (8,10). However, previous investigators assumed $\nu = 10^{13}$ instead of determining it from experimental data.

Figures 5a and 5b show the results for NO scattering from Pt(557), showing the similar features as from Pt(111). Fitting the data above 525K to the adsorption-desorption model with fixed sticking coefficient gives $\nu = 1.2 \times 10^{14}$, E = 32.3 Kcal/mole, and S = 0.71. Comparison of these results with those of Pt(111) suggests that the adsorption-

desorption kinetics for NO scattered from Pt(557) at temperature above 525K should be the same as that for CO scattering from the same crystal surface. In other words, although NO can chemisorb on terrace and step sites, those molecules chemisorbed on the terrace have to visit the steps once before desorbing and the desorption kinetic is controlled by the step sites.

The data below 525K are quite different from that predicted from the adsorption-desorption model for NO scattered from Pt(111). With decreasing temperature, the amplitude goes up and then drops sharply. The phase lag changes correspondingly. Below 400K, the amplitude starts to rise again. The features of the data can be used to rule out many models immediately. The usual linear, parallel process can explain the characteristics of the phase lag, but not the amplitude, and thus, has to be ruled out. Nevertheless, the data seem to indicate that one high adsorption energy state is sampled above 525K and a lower adsorption energy state appears suddenly below 480K. One of the models tried is a modified parallel process—Model A.

$$
A(g) \quad
\begin{array}{l}
\xrightarrow{(1-S)I_0 g(t)} A(g) \\[4pt]
\xrightarrow{\quad pSI_0 g(t) \quad} A(a_1) \xrightarrow{\ k_1\ } A(g) \\[4pt]
\xrightarrow{(1-P)SI_0 g(t)} A(a_2) \xrightarrow{\ k_2\ } A(g)
\end{array}
$$

where p is coverage dependent instead of a constant. Basically, we manage the sticking molecule to fill site 1 first before it can migrate to site 2. The curves in Fig. 4 are the best fit to this model, without using the data below 400K. Although the fit to the

model is reasonably good, we obtained unusual parameter values for the best fit; $k_2 = 9.8 \times 10^7 \exp(-13.3/RT)$. The model was used to fit the data for NO scattering from Pt(557) and the fitting was found to be worse. This is not surprising since the surface structure of Pt(557) is more complicated than that of Pt(111).

As mentioned before, the desorption kinetics are controlled by the step sites which occupy only 17 percent of the total surface area of Pt(557). If desorption kinetics are also controlled by the defect site on Pt(111) surface, then a small amount of contamination will change the kinetics if the defect density is not high. We intentionally increased the defect density by sputtering at higher argon energy and found that the kinetics changed. Recently, Serri et al. have suggested that less than 1 percent of oxygen contamination, which is difficult to detect with AES, can influence the kinetics of NO desorption from Pt(111) surface drastically (20).

To see how the data were affected by beam intensity, we tried NO scattered from Pt(111) at 100 Hz with backing pressure of 1.5 Torr rather than 10 Torr and from Pt(557) at 10 Hz with backing pressure of 2 Torr. The results are shown in Figs. 6 and 7. The main difference is that the sticking coefficient is larger for the lower beam intensity, indicating that the sticking coefficient decreases as the coverage increases.

We tried to obtain evidence for NO dissociation by measuring the modulated O_2 and N_2 signals as function of the crystal temperature at different frequencies. Compared with the modulated NO signal, O_2

and N_2 signals were very small and independent of the crystal
temperature. We believe NO does not dissociate to any appreciable
extent under our experimental conditions. The same conclusion is
found later by Serri et al. (20).

3.4 Conclusion

The modulated molecular beam scattering of CO and NO from Pt(111)
and Pt(557) have been studied in the temperature range of 350-1100K.
For CO scattered from Pt(111), an adsorption-desorption model with
constant sticking coefficient fits the data well above 500K. The best
rate parameters are ν = 2.9 x 10^{13}, E = 29.9 Kcal/mole, and S =
0.74. For CO scatterted from Pt(557) the same model fits the data
well above 550K and the best rate parameters are ν = 7.9·x 10^{13}, E =
33.6 Kcal/mole, and S = 0.74. The higher activation energy for
desorption from the stepped Pt(557), as compared to the flat Pt(111),
suggests that while the incident molecules can be adsorbed at the step
as well as at the terrace, their desorption kinetic is controlled by
the steps. It appears that any adsorbed molecule has to visit the
step sites once before it desorbs.

For NO scattered from Pt(111), the adsorption-desorption model
with constant sticking coefficient fits the data well above 525K using
the rate parameters of ν = 6.2 x 10^{13}, E = 28.6 Kcal/mole, and S =
0.65. For NO scattered from Pt(557), the same model fits the data
well above 525K with ν = 1.2 x 10^{14}, E = 32.3 Kcal/mole, and S =
0.71. The higher activation energy suggests again that NO desorption
kinetic is controlled by the steps. Below 525K, the NO scattering

results are very different from those of CO and indicate that one high adsorption energy state is sampled above 525K and a lower adsorption energy state appears suddenly below 480K. The features of the data rule out the usual linear, parallel or series processes immediately. The nonlinear process might be due to the fact that the desorption kinetic is controlled by a small concentration of defects which would be blocked by some impurity at lower temperature.

References

1. G. Ertl, M. Neumann, and K. M. Streit, Surface Sci. 64, 393 (1977).

2. D. M. Collins and W. E. Spicer, Surface Sci. 69, 114 (1977).

3. R. A. Shigeishi and D. A. King, Surface Sci. 58, 379 (1976).

4. G. Ertl, Surface Sci. 89, 525 (1979).

5. P. R. Norton, J. W. Goodale, and E. B. Selkirk, Surface Sci. 83, 189 (1979).

6. A. M. Baro and H. Ibach, J. Chem. Phys. 71, 4812 (1979).

7. A. Crossley and D. A. King, Surface Sci. 95, 131 (1980).

8. C. M. Comrie, W. H. Weinberg and R. M. Lambert, Surface Sci. 57, 619 (1976).

9. H. Ibach and S. Lehwald, Surface Sci. 76, 1 (1978).

10. J. L. Gland, Surface Sci. 71, 327 (1978).

11. J. L. Gland and B. A. Sexton, Surface Sci. 94, 355 (1980).

12. R. L. Gorte and J. L. Gland, Surface Sci. 102, 348 (1981).

13. H. P. Bonzel and G. Pirug, Surface Sci. 62, 45 (1977).

14. R. H. Jones, D. R. Olander, W. J. Siekhaus and J. A. Schwarz, J. Vacuum Sci. Technol. 9, 1429 (1972).

15. J. A. Schwarz and R. J. Madix, Surface Sci. 46, 317 (1974).

16. D. R. Olander and A. Ullman, Intern. J. Chem. Kin. 8, 625 (1976).

17. C. T. Campbell, G. Ertl, H. Kuipers and J. Segner, Surface Sci. 107, 207 (1981).

18. G. E. Gdowski and R. J. Madix, Surface Sci. 115, 524 (1982).

19. C. T. Campbell, G. Ertl, and J. Segner, Surface Sci. 115, 309 (1982).

20. J. A. Serri, M. J. Cardillo, and G. E. Becker, J. Chem. Phys. <u>77</u>, 2175 (1982).

21. T. H. Lin and G. A. Somorjai, Surface Sci. <u>107</u>, 573 (1981).

22. S. L. Bernasek, Ph.D. Thesis, University of California, Berkeley (1975).

23. M. Salmeron, R. J. Gale and G. A. Somorjai, J. Chem. Phys. <u>67</u>, 5324 (1977).

24. H. Ibach, W. Erley and H. Wagner, Surface Sci. <u>92</u>, 29 (1980).

Figure Captions

Fig. 3.1 Schematic diagram of modulated molecular beam scattering apparatus.

Fig. 3.2 Normalized amplitudes and phase lags as function of the crystal temperature for CO scattered from Pt(111). Curves are theoretical fits to the adsorption-desorption model with coverage dependent sticking coefficient. (a) f = 10 Hz, (b) f = 100 Hz.

Fig. 3.3 Normalized amplitudes and phase lags as a function of the crystal temperature for CO scattered from Pt(557). Curves are theoretical fits to the adsorption-desorption model with coverage dependent sticking coefficient. (a) f = 10 Hz, (b) f = 100 Hz.

Fig. 3.4 Normalized amplitudes and phase lags as a function of the crystal temperature for NO scattered from Pt(111). Curves are theoretical fits to model A (a) f = 5 Hz, (b) f = 10 Hz, and (c) f = 100 Hz.

Fig. 3.5 Normalized amplitudes and phase lags as a function of the crystal temperature for NO scattered from Pt(557). Curves are theoretical fits (a) f = 10 Hz, (b) f = 100 Hz.

Fig. 3.6 NO scattered from Pt(111) at 100 Hz with backing pressure of 1.5 Torr instead of 10 Torr.

Fig. 3.7 NO scattered from Pt(557) at 10 Hz with backing pressure of 2 Torr instead of 10 Torr.

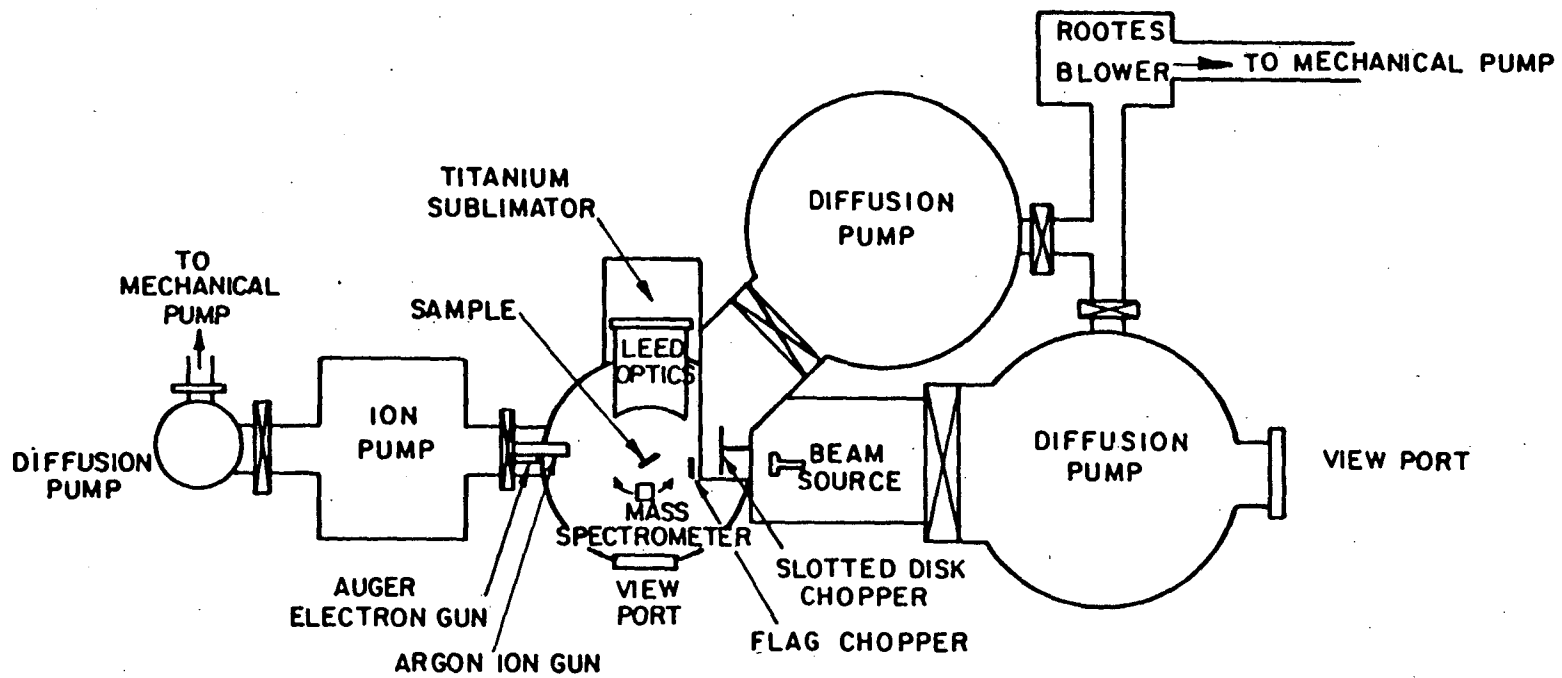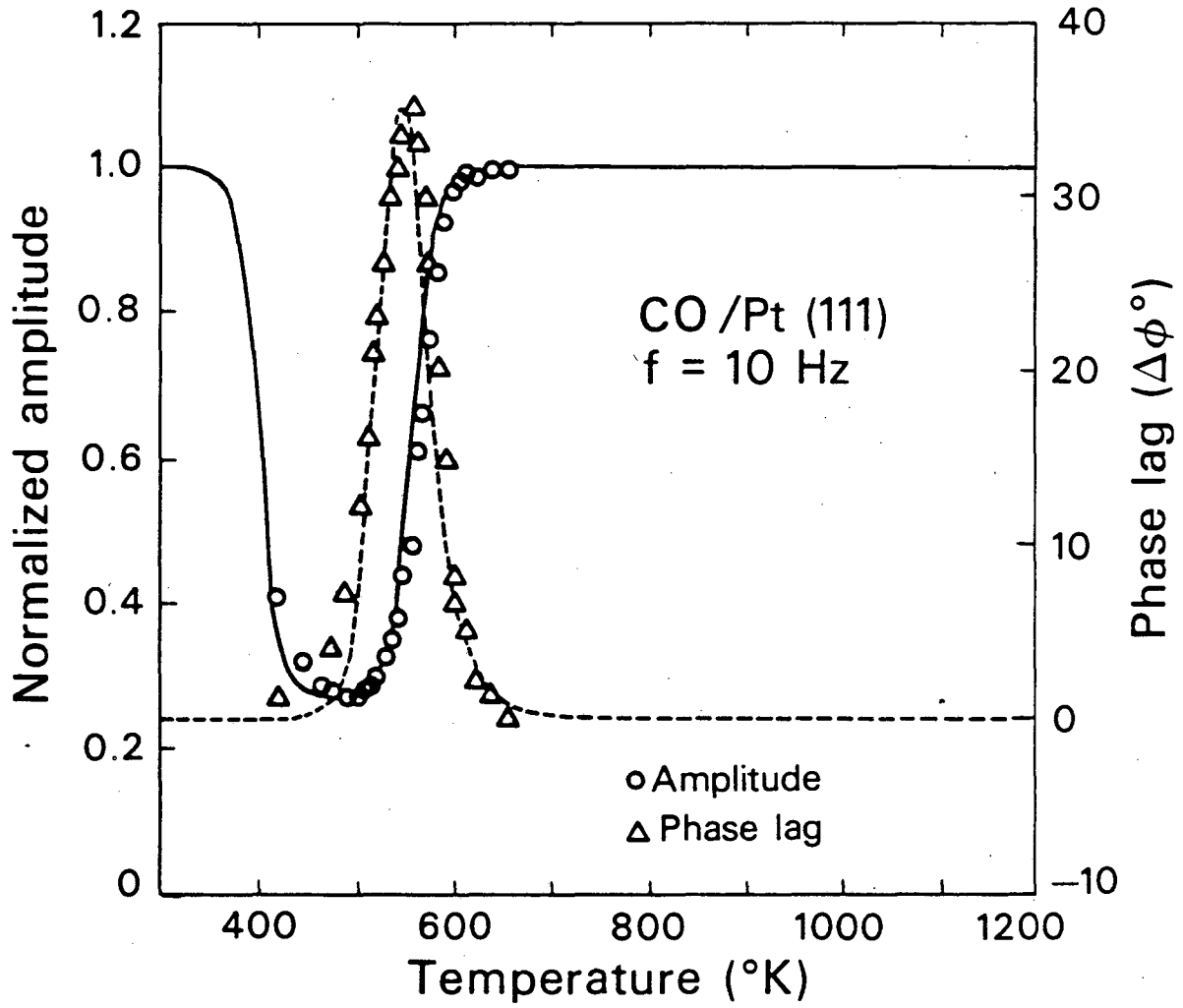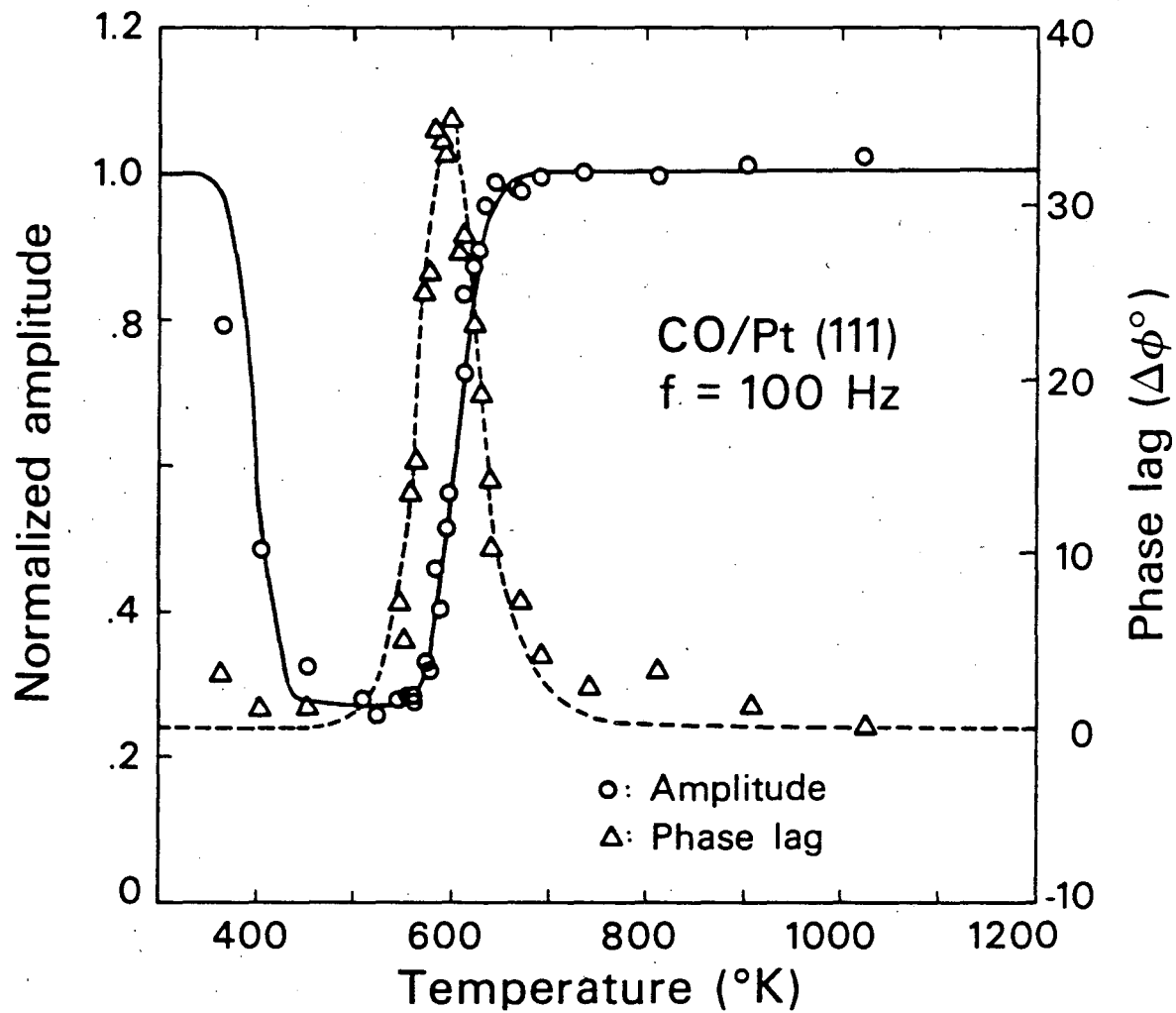TO MECHANICAL PUMP

ROOTES BLOWER

DIFFUSION PUMP

TITANIUM SUBLIMATOR

TO MECHANICAL PUMP

SAMPLE

LEED OPTICS

DIFFUSION PUMP

ION PUMP

DIFFUSION PUMP

BEAM SOURCE

VIEW PORT

MASS SPECTROMETER

VIEW PORT

SLOTTED DISK CHOPPER

AUGER ELECTRON GUN

ARGON ION GUN

FLAG CHOPPER

XBL 785-4948

Figure 3.1

59

XBL 8011-2325

Figure 3.2a.

CO/Pt (111)
f = 100 Hz

o: Amplitude
△: Phase lag

XBL 8011-2324
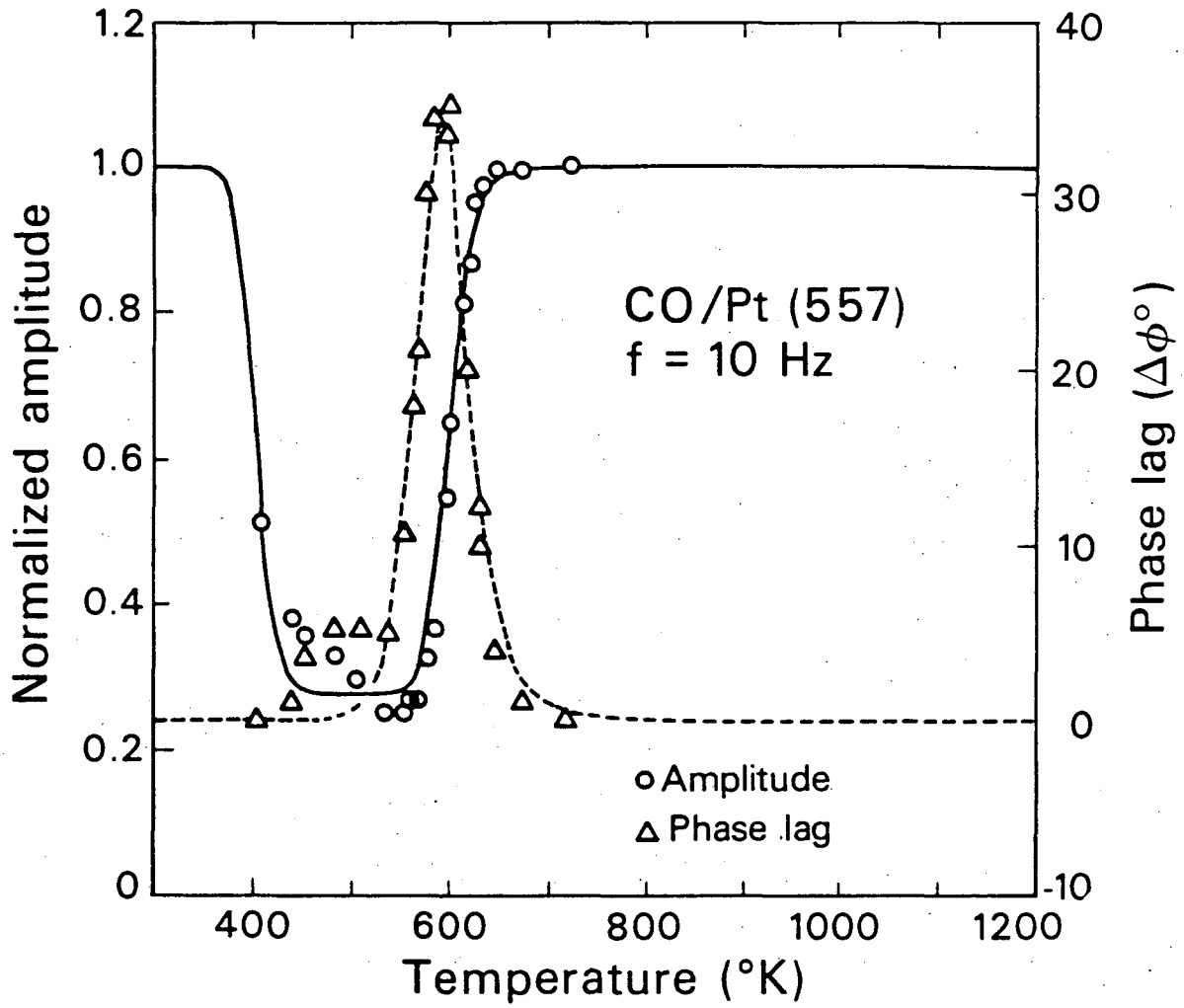
Figure 3.2b.
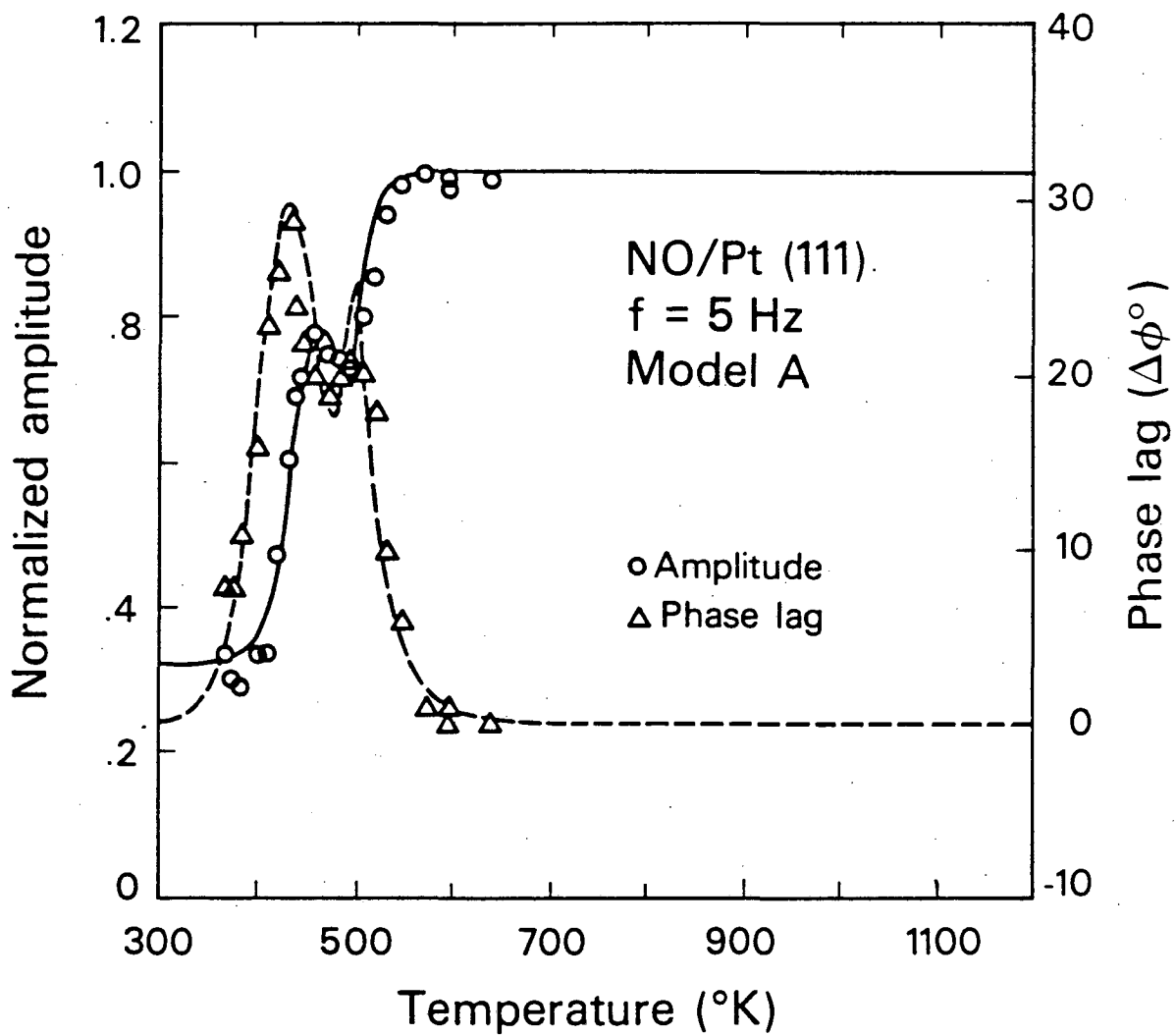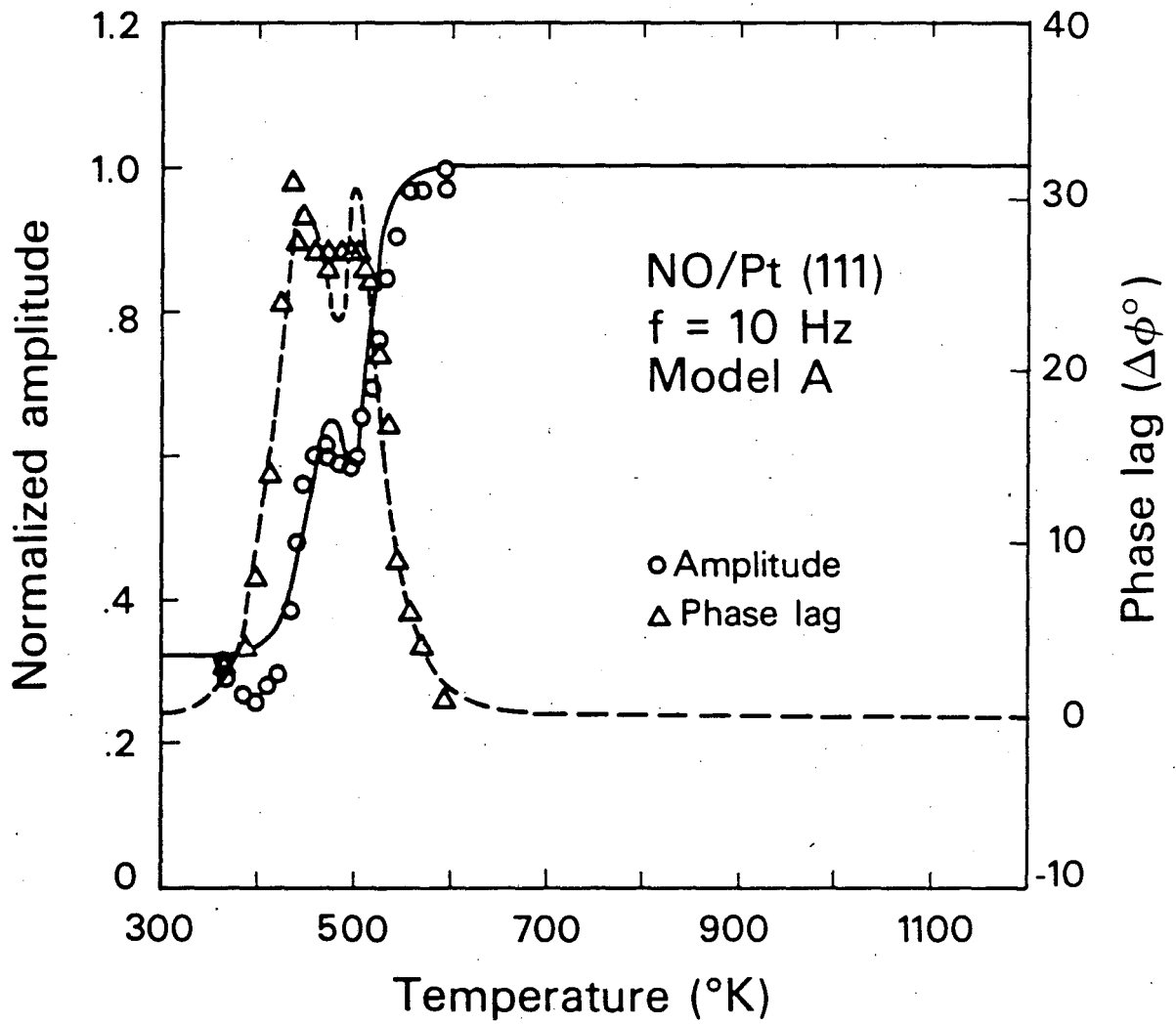
Figure 3.3a.

XBL 8011-2327
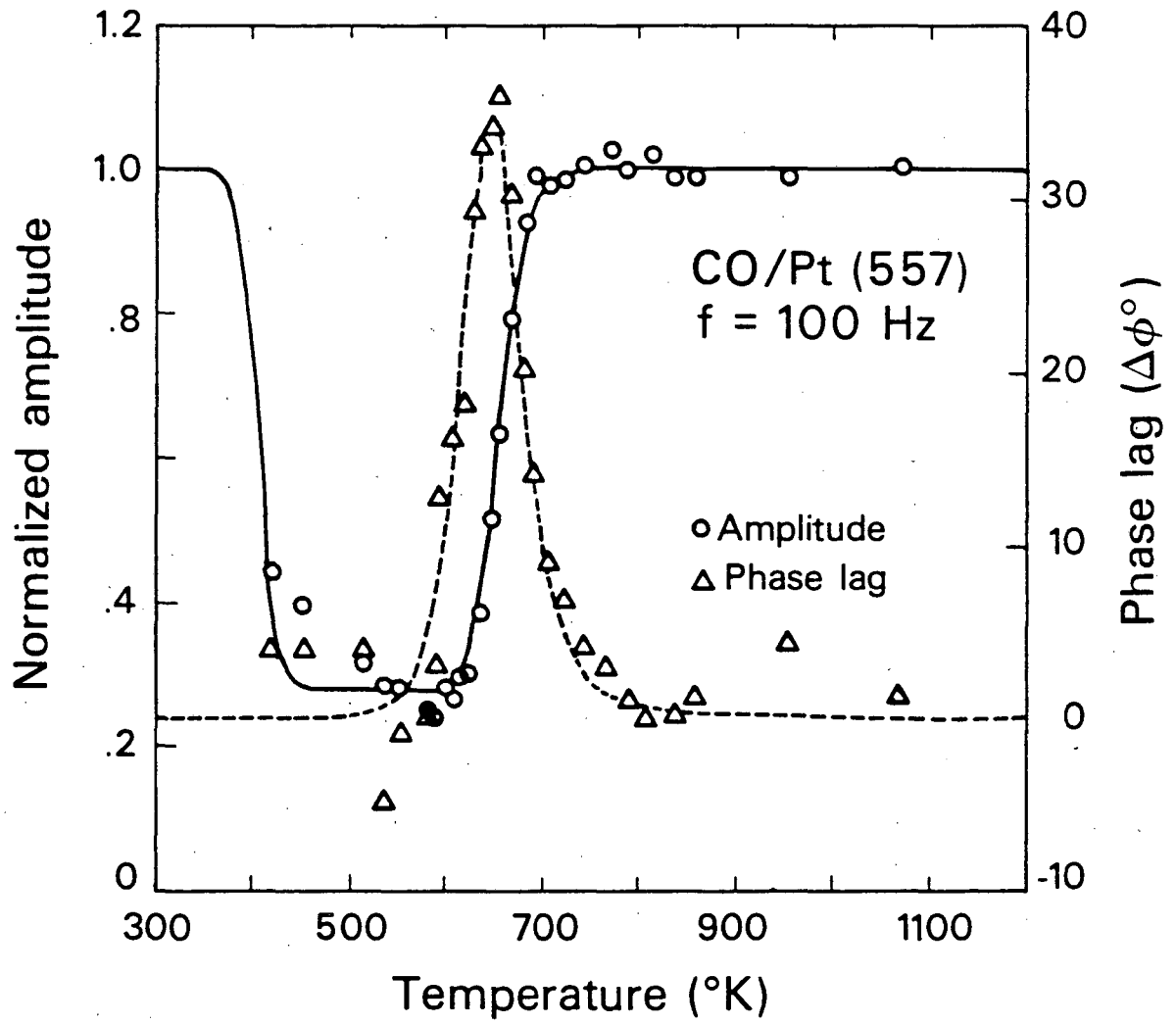
XBL 8011-2326

Figure 3.3b.

64

XBL 8011-2328

Figure 3.4a.

NO/Pt (111)
f = 10 Hz
Model A

o Amplitude
△ Phase lag

XBL 8011-2329

Figure 3.4b.

NO/Pt (111)
f = 100 Hz
Model A

o Amplitude
△ Phase lag

XBL 8011-2332

Figure 3.4c.

NO/Pt (557)
f = 10 Hz
Model A

o Amplitude
△ Phase lag
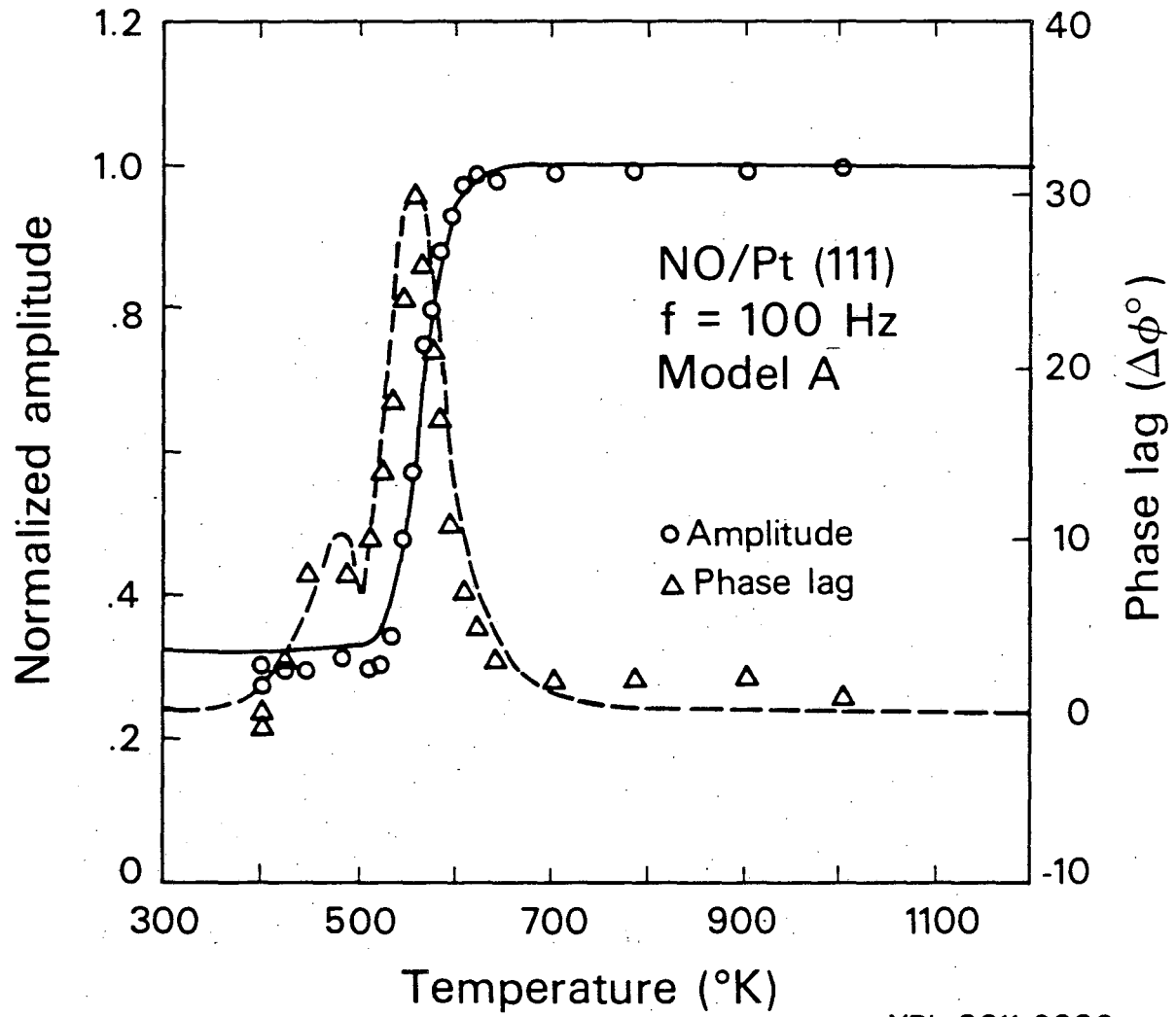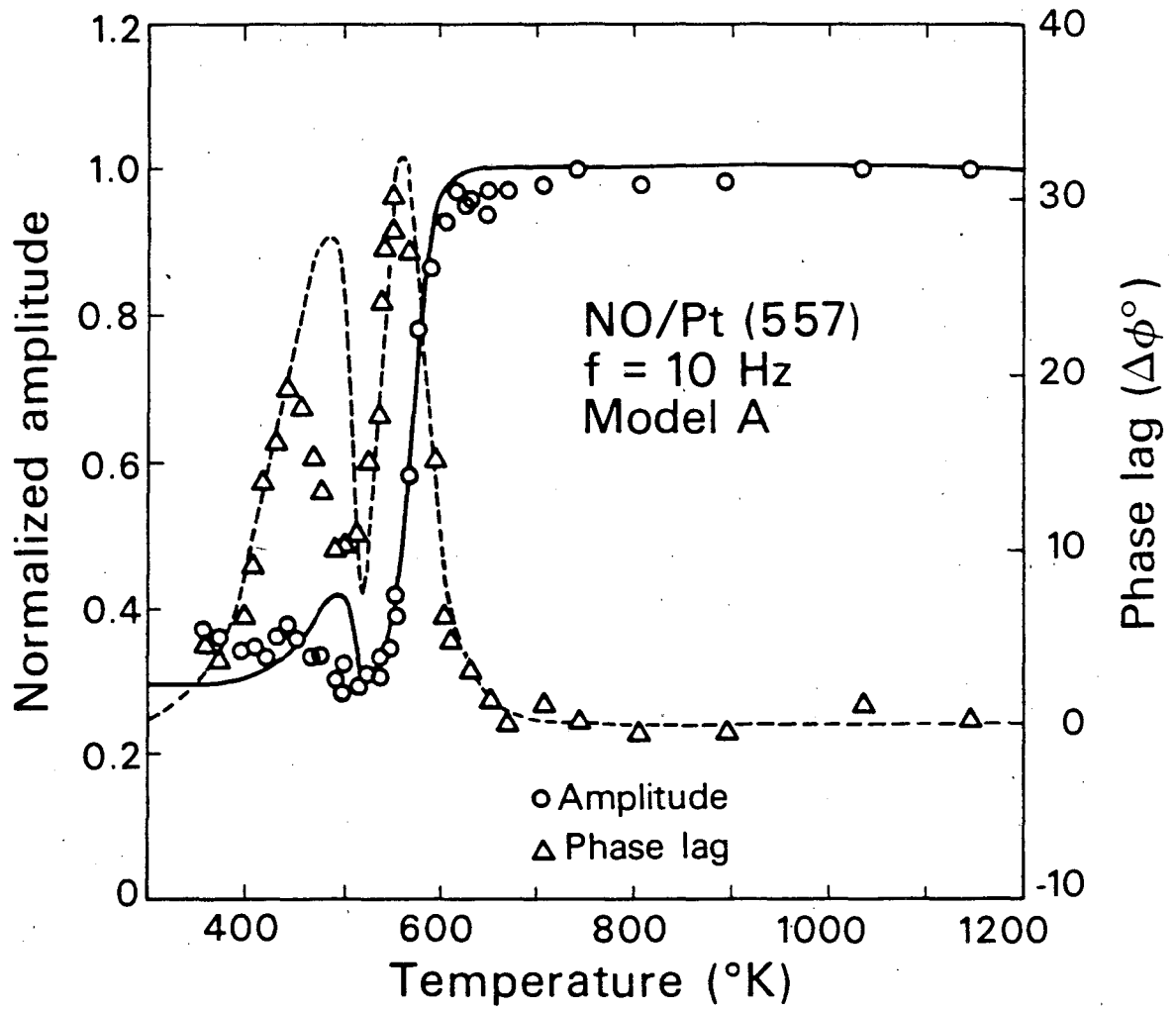
XBL 8011-2322

Figure 3.5a.

XBL 8011-2323

Figure 3.5b.

NO/Pt (111)
f = 100 Hz
B.P. = 1.5 Torr

o Amplitude
△ Phase lag

XBL 8011-2330

Figure 3.6

NO/Pt (557)
f = 10 Hz
B.P. = 2 Torr

o Amplitude
△ Phase lag
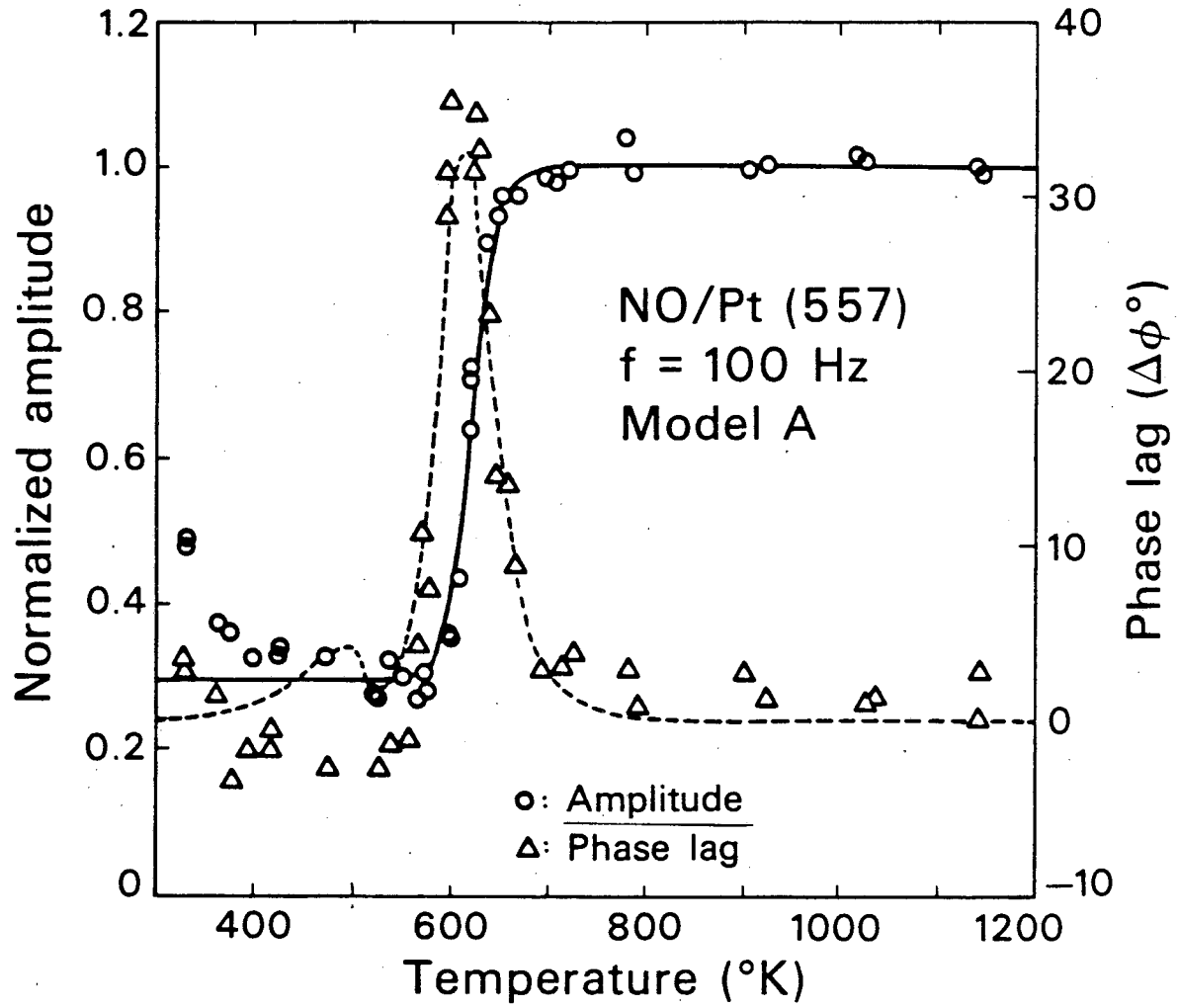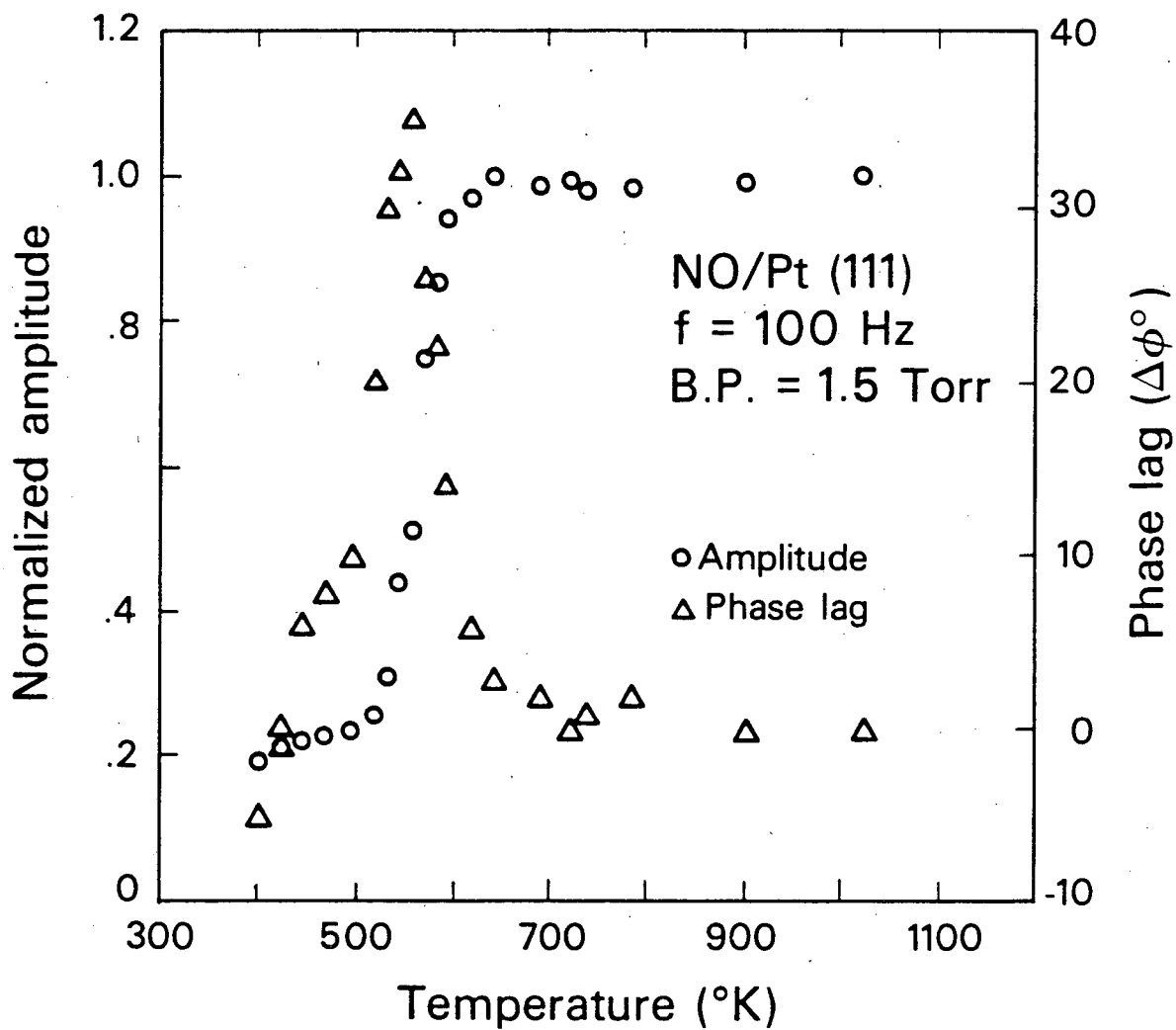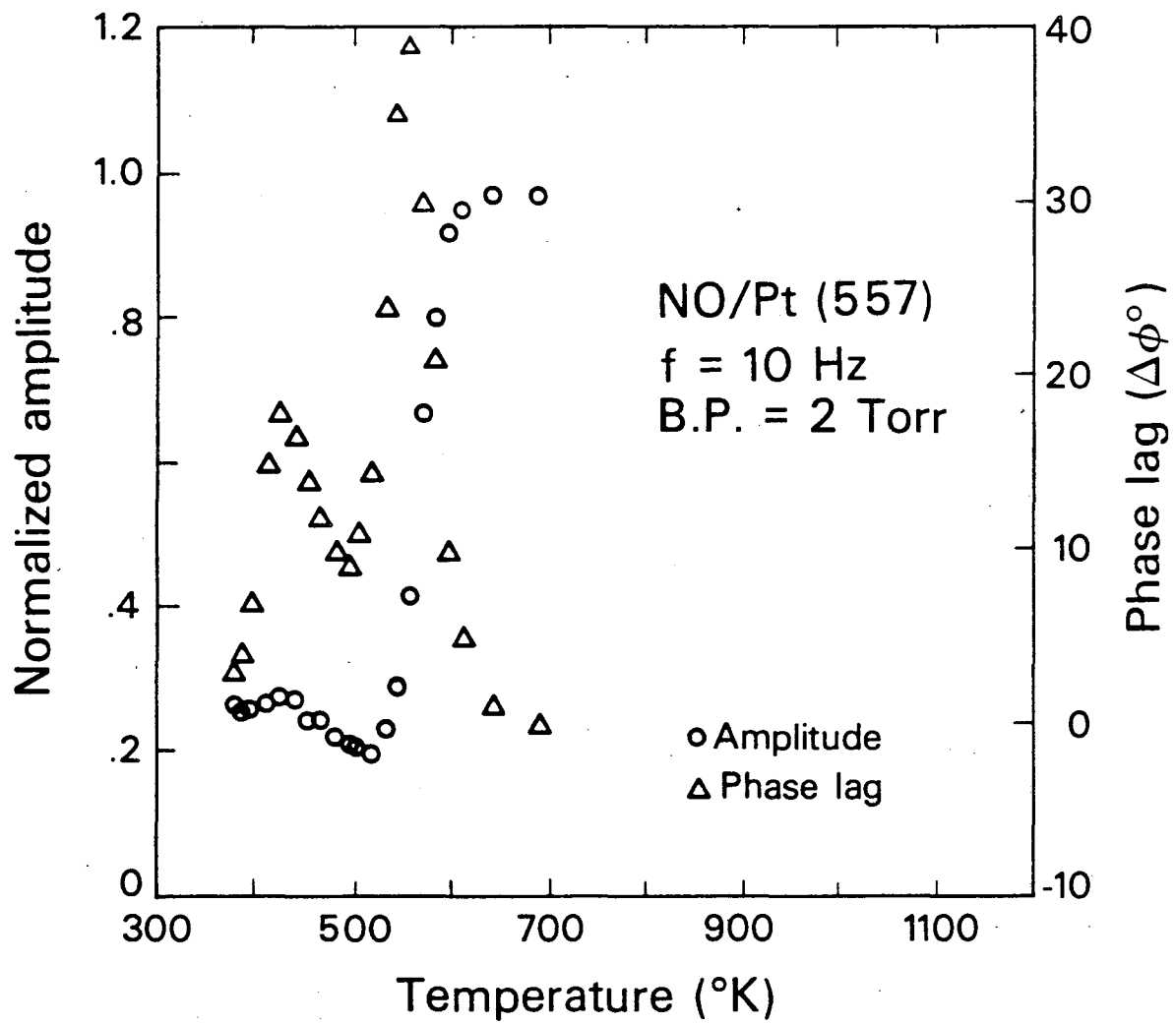
XBL 8011-2331

Figure 3.7

CHAPTER IV

ANGULAR, TRANSLATIONAL, ROTATIONAL, AND VIBRATIONAL

ENERGY DISTRIBUTIONS OF NO SCATTERED FROM THE Pt(111) SURFACE

4.1 Introduction

The study of energy transfer between gas molecules and solid
surfaces is crucial to the understanding of the fundamental processes
in heterogeneous catalysis, for example, adsorption, decomposition,
surface diffusion, bond formation and desorption. Molecular beam-
surface scattering technique provides one of the best ways of
investigating gas-solid energy transfer processes. With this
technique, the amount of energy exchanged between molecules and the
surfaces can be measured for a single collision from the translational,
rotational and vibrational energy distributions of the scattered and
the incident molecules.

In the past, most of the energy exchange information was obtained
by monitoring the angular distribution of the scattered molecules
(1-2). Recently, the translational and internal energy distributions
of molecules scattered from well characterized surfaces have been
measured in various laboratories (3-12). For the most part, however,
the systems that have been studied are only weakly attractive; for
example, Ar on tungsten, Xe on platinum, and NO on silver. To gain
insight into the energy transfer processes on a chemically interesting
system we have measured the angular, translational, rotational and
vibrational energy distributions of nitric oxide scattered from a
Pt(111) single crystal surface. The translational energy distribution

was obtained using a time-of-flight (TOF) technique and the internal energy distributions by two photon ionization (TPI). (This will be described in more detail in a subsequent section.)

For NO, TPI is at least one order of magnitude more sensitive than the optimum laser-induced fluorescence measurements (8-12). For the first time, angular, translational, rotational, and vibrational energy distributions of the scattered molecules are obtained for the one system. These results should considerably help the theoretical study of elementary surface processes.

We find that the rotational energy accommodation is relatively poor and that the vibrational energy transfer is somewhat more efficient but declines with increasing crystal temperature. The translational energy is found to be equilibrated with the surface except at very high crystal temperatures.

4.2 Experimental

4.2.1 Translational Energy and Angular Distributions. The apparatus is described in Section 2 of Chapter 2, and so, only experimental conditions will be described here. The angle of the incident beam was ~51° in all of our experiments. TOF was measured by moving the detector either to 7° from the surface normal or to the specular angle of 51°. The surface temperature (Ts) was varied from 475 to 1195K. The pseudo-random chopper was operated at 180 Hz, and 15 to 25 min. were required to obtain each TOF distribution depending on the incident beam energy.

The mass spectrometer is density sensitive rather than flux sensitive, and so, to calculate the flux mean kinetic energy and the spread of the velocity distribution, the velocity moments M_1, M_2 and M_3 are obtained from the TOF data. The moments M_I (I=1, 2, 3) are defined as follows:

$$M_I = \int_0^\infty v^I p(v) dv$$

where $p(v)$ is the density velocity distribution of the scattered molecules. M_1 is proportional to the flux into the detector. The flux mean kinetic energy <KE> and the spread of the velocity distribution $<\sigma^2>$, are given by

$$<KE> = (1/2) \, m<v^2> = (1/2) \, mM_3/M_1$$

$$<\sigma^2> = (<v^2>-<v>^2)/<v>^2 = M_1 M_3 / M_2^2 - 1$$

where m is the mass of the molecule. For a beam with a Maxwellian density distribution at temperature of T, the flux mean kinetic energy is 2kT rather than (3/2) kT and $<\sigma^2>$ is 0.132. Hereafter, the term "a beam energy of TK" will imply that the beam mean kinetic energy is equal to 2kT.

NO supersonic beams with three different flux mean kinetic energies <KE>/2k = 265, 615, and 1390K were used. The corresponding values of $<\sigma^2>$ are 0.026, 0.038, and 0.024, respectively. Beams of 265 and 1390K were obtained by antiseeding NO with xenon and seeding with helium while keeping the nozzle at room temperature.

A TOF distribution of NO from an effusive source at 300K is shown in Fig. 1. The solid curve corresponds to a Maxwellian distribution at 300K. The agreement between the theoretical curve and the data points from the effusive source is excellent. Several TOF distributions of effusive thermal beams were obtained in order to calibrate the flight path and also to determine the zero flight-time channel.

4.2.2 <u>Internal Energy Distributions</u>. A schematic diagram of the apparatus is shown in Fig. 2. The main difference between this and the modified TOF apparatus described in Chapter 2 is the detector. The detector, equipped with an electron multiplier for ion detection and a quartz lens for focusing the UV laser beam, is mounted on a 24 in. diameter rotatable flange. The laser beam was aligned externally with the center of the rotatable flange, then deflected 2.5 cm off axis, so that rotation of the flange caused laser beam and the detector to move synchronously.

The UV laser system is a Quanta-Ray Nd:YAG pumped dye laser together with a wavelength extension unit. This system is capable of generating tunable UV radiation near 225 and 236 nm which is required to excite the $A^2\Sigma^+(v'=0)\leftarrow X^2\pi_{1/2}(v''=0)$ and $A^2\Sigma^+(v'=0)\leftarrow X^2\pi_{1/2}(v''=1)$ NO vibronic transitions. The laser energy was monitored by two separate photodiodes. One of the signals from the photodiodes was used for manual monitoring of the laser intensity and the other was used to normalize the signal from the ion multiplier. The signal processing was performed by a minicomputer.

4.3 Results

4.3.1 Angular Distributions. Figure 3 shows a typical angular distribution of the scattered NO molecules. The closed circles represents the experimental data, the solid line shows a cosine function, and the open circles represents the difference between the data and the cosine function. The angular distribution can be separated into a cosine angular distribution and a broad angular distribution peaked near the specular (indicated by the arrows on the lower axis of the figures). We have observed that all the angular distributions are dominated by a cosine angular distribution with a slight increase in the flux near the specular angle.

The general features of the angular distributions as functions of incident beam energy and of the crystal temperature are shown in Figs. 4 and 5. Figure 4 represents the angular distributions at a fixed crystal temperature of 1195K. The triangles, closed circles and pen circles represent the distributions for the incident beam energies of 265K, 615K, and 1390K, respectively. Evidently the degree of specularity increases as the incident beam energy increases. Figure 5 shows the angular distributions for a fixed incident beam energy of 615K. The closed circles, open circles, and the triangles represent the distributions for crystal temperatures of 475K, 725K, and 1195K respectively. The specularity of the distribution also increases as the crystal temperature increases.

4.3.2 <u>Translational Energy Distributions</u>. Typical time-of-flight distributions under different experimental conditions are displayed in Figs. 6 and 7. The experimental variables are the crystal temperature, T_s, the incident beam energy, T_B, and the detection angle, either specular or near the surface normal. The solid curves correspond to a Maxwell-Boltzmann distribution at the respective crystal temperatures. The Maxwell-Boltzmann distributions have been convoluted with the TOF chopper and electronic gating width to reproduce the experimental broadening.

Rather than present the complete body of data, we present the two important parameters that characterize the TOF distribution, the flux mean kinetic energy in units of K, and the velocity spread $\langle\sigma^2\rangle = (\langle v^2\rangle - \langle v\rangle^2)/\langle v\rangle^2$, as functions of the experimental variables. In Figs. 8, 9, and 10, these parameters are plotted as a function of crystal temperature for the three different incident beam velocities. The arrows on the ordinates of Figs. 8(b) and 9(b) indicate the expected width ($\langle\sigma^2\rangle$) for a Maxwell-Boltzmann distribution. Experimental broadening makes the expected value slightly larger than the theoretical value of 0.132.

The incident beam energy for the data shown in Fig. 8 is 1390K. From Fig. 8(a), it is clear that for $T_s < 900K$, the scattered beam energy at the specular scattering angle is larger than that at the surface normal, and both are different from the surface temperature. For $T_s > 900K$, the scattered beam energies at both specular and normal angles are similar to the surface temperature. This, however,

does not imply equilibration with the surface as can be seen from Fig. 8(b). The $<\sigma^2>$ for scattering in the specular direction is smaller than that of a Maxwell–Boltzmann distribution, the discrepancy being largest at higher T_s. Figure 7(b) shows that the TOF distribution at the specular angle is visibly narrower than the corresponding Maxwell–Boltzmann distribution, whereas $<\sigma^2>$ for molecules scattered at 7° is that for the corresponding Maxwellian distribution.

The incident beam kinetic energy for the data shown in Fig. 9 is 615K. At the surface normal, the kinetic energy of the scattered NO beam is equal to T_s for $T_s < 900K$, and becomes smaller than T_s above 900K. In the specular direction, the scattered beam kinetic energy shows the same trend. In general, the specularly scattered beam has less kinetic energy than that at the surface normal, especially at high surface temperatures. $<\sigma^2>$ in the specular direction is smaller than that near the surface normal for low T_s [Fig. 9(b)], but the $<\sigma^2>$ at these angles become almost equal at high T_s. The difference in the widths of the distributions at low surface temperature is visually evident in Fig. 6.

The incident beam energy for the data shown in Fig. 10 is 265K. The scattered beam energy shows the same trend as a function of T_s as that shown in Fig. 9(a). The kinetic energies of the scattered beam in both the specular and the normal directions are in general less than those for the 615K incident beam energy. For $T_s < 800K$, the mean kinetic energy of the beams scattered in the normal direction

is independent of incident beam energy and equal to the corresponding surface temperatures. $<\sigma^2>$ of the scattered beams for this incident beam energy 265K are inconclusive because the statistical error is large due to the lower incident beam intensity.

4.3.3 <u>Rotational Energy Distributions</u>. Typical vibronic two photon ionization (TPI) spectra are shown in Fig. 11a, b and c for the direct incident beam, room temperature NO, and NO scattered from the Pt(111) surface at 580K, respectively. The laser wavelength is near 226nm and the electronic transition of one photon absorption is $A^2\Sigma^+(V'=0) \leftarrow X^2\pi_{1/2}(V''=0)$. The rotational temperature is obtained by plotting the logarithims of the rotational line intensities $N_{j''}$ normalized by the rotational degeneracy $(2j''+1)$ and rotational line strength factor $S_{j''}$ versus the rotational energy. Due to the saturation of the first electronic transition under our experimental condition, $S_{j''}$ is equal to 1. For a crystal temperature of less than 850K, we have found that the scattered NO molecules can be characterized by a single rotational temperature which is colder than the corresponding crystal temperature except for a substrate temperature of 295K. These results are shown in Fig. 12, where the incident beam energy is 615K, and the detector is at the surface normal. We also observe that there is considerable deviation from a single rotational temperature for $T_s = 870K$. At $T_s = 580K$, different rotational temperatures, T_{rot}, were obtained at the two scattering angles: $T_{rot} = 400 \pm 40K$ for normal scattering, and $T_{rot} = 480 \pm 40K$ for specular scattering. The angular distribution

of the scattered NO for a fixed rotational state is dominated by a cosine angular distribution with a slight increase in the flux near the specular angle.

4.3.4 <u>Vibrational Energy Distributions</u>. The vibrational excited state was monitored by tuning the laser to 236nm and exciting the $A^2\Sigma^+(v'=0)\leftarrow X^2\pi_{1/2}(v''=1)$ transition. Figure 13 shows the angular distribution of the vibrationally excited NO molecules scattered from the Pt(111) surface at 820K. The angular distribution is an almost perfect cosine function without any sign of the enhancement near the specular angle. The relative populations of the ground state and the vibrationally excited state is determined as follows.

The laser is tuned to around 236.28nm, the $Q_{11}+P_{21}$ band head of the scattered NO molecules could be scanned and averaged over 100 laser pulses for each wavelength. The crystal was removed and the scattering chamber filled with room temperature gas phase NO to the pressure that gave the same signal intensity as that of the scattered molecules. This reference signal originates from an effective pressure of NO(v''=1) molecules that is the measured pressure times the vibrational Boltzmann factor at room temperature. This is 1.05 x 10^{-4} for T_v = 295K and E_v = 1876.1 cm^{-1}. This procedure is repeated for the scattered ground state molecules. The ratio between the two effective pressures is the population ratio of NO(v''=1) and NO(v''=0) molecules and is calculated at four crystal temperatures, T_s = 620, 820, 990 and 1155K. For other crystal temperatures, the

ratio is measured by monitoring a relative signal for both the ground state and the vibrationally excited molecules and the ratios between these signals were then normalized to the directly measured ratios. The vibrational temperatures of the scattered NO can be calculated with these ratios, and the results are shown in Fig. 14. One can see that the vibrational temperature of the desorbed molecules is lower than T_s but does not differ by more than 100K for $T_s < 1000K$.

4.4 Discussion

4.4.1 Scattering Mechanisms. The energy exchange between the incident molecules or atoms and the surface is generally discussed in terms of three scattering mechanisms: namely, elastic, inelastic, and trapping-desorption (1,13). For elastic scattering there is little or no energy exchange between the gas molecules and the surface. Thus, the angular distribution is very narrow and peaked in the specular direction for scattering from a smooth surface. This scattering mechanism occurs when the the interaction between the incident atom and the surface is very weak, as in the case of, for example, helium scattered from the Pt(111) surface.

For the inelastic scattering, there is some energy exchange between the gas molecules and the surface. The scattered beam energy depends on the incident beam energy and is weakly surface temperature dependent. The angular distribution of the scattered beam is characterized by a broad peak distribution while the peak is not necessarily in the specular direction. The reflected intensity becomes less peaked as the surface temperature increases.

For trapping-desorption scattering, the incident molecules are trapped in the region of the surface for many vibrational periods allowing accommodation. The scattered beam energy is strongly surface temperature dependent and does not depend on the incident beam energy. The angular distribution is diffuse and is often a cosine function.

For any particular system, such as He/Pt(111) or NO/Pt(111), the scattering does not occur by a single mechanism but by a combination of two or even three processes. For NO scattered from Pt(111), the elastic scattering mechanism is unimportant due to the strong interaction potential (14-16). The results of Chapter III, show that the majority of the incident NO is trapped before desorbing below 700K while there is always some fraction which is not trapped. It is assumed that the trapping-desorption and inelastic scattering processes both operate during all of our experiments and can explain all the results. This assumption does explain all the experimental results consistantly and therefore, appears to be valid.

4.4.2 Angular Distributions

Figure 3 shows that the angular distribution can be separated into two fractions: the cosine function and the broad angular distribution peaked near the specular angle. Associating the former fraction with trapping-desorption scattering and the latter with inelastic scattering, it is observed that both scattering mechanisms coexist and that the trapping-desorption mechanism is dominant. This is true over the whole temperature range investigated, i.e. $T_s = 475 - 1195K$.

Although the broad angular width of the inelatic portion makes the separation of the two fractions difficult, trapping-desorption is estimated to contribute about 80-90 percent of the total scattering. This is consistent with previously published results (14-16). The degree of specularity increases as the incident beam energy or the crystal temperature increases which indicates that more of the incident molecules are inelastically scattered as the incident beam energy or the crystal temperature increases. As the incident beam energy increases, more energy transfer is needed to trap the molecules; thus, the trapping-desorption fraction decreases. Increasing crystal temperature will decrease the residence time of the molecules on the surface; therefore, more molecules are inelastically scattered.

4.4.3 <u>Translational Energy Distributions</u>. With two scattering mechanisms present, the TOF distributions will be a sum of two distributions. The trapping-desorption fraction accommodates almost completely with the surface and, thus, has approximately the corresponding Maxwellian distribution. The inelastic fraction cannot completely accommodate with the surface, thus, its TOF distribution should be close to that of the incident beam. In the normal direction, the trapping-desorption fraction has the major contribution to the flux. At the specular angle, both the inelastic fraction and the trapping-desorption fraction will contribute significantly.

For a 1390K incident beam and T_s=475-1195K, the average energy of the inelastic fraction will be higher than that of the trapping-

desorption fraction, especially, at low surface temperatures. This explains why the average energy at the specular angle is higher than that at the normal for T_s <900K in Fig. 8(a). At T_s=1195K and for specular angle detection the inelastic and trapping-desorption velocity distributions overlay each other. Thus, the TOF distribution will be narrow since the inelastic fraction has a very narrow distribution due to the narrow distribution of the incident beam. At lower surface temperatures and for specular angle detection, the two mechanism have velocity distributions separated in energy so that the total distribution is broader. This trend is shown clearly in Fig. 8(b) for specular detection. The same argument can be applied to the results of Fig. 9.

To determine the existence of accommodation from the velocity distributions, it is necessary to examine the average energy of the distribution and the width, $<\sigma^2>$. The average energy can have the equilibrium value, if the inelastic scattering has the right energy, but the width will be too small, as is visually evident in Figs. 6(b) and 7(b). Likewise, the width may be artificially large due to the separation of the average energies of the two scattering mechanisms. Examination of Figs. 8, 9 and 10 shows complete equilibration only for T_s=475-900K at scattering near normal and T_B = 265 and 615K.

For T_B = 1390K, T_s = 475K, and for scattering near the surface normal, the lack of accommodation is unusual given the weakness of the specular feature in the angular distribution. From this, we conclude that the angular distribution of inelastic scattering is extremely

broad. For T_B = 265 and 615K, and scattering at the surface normal, the degree of accommodation falls for T_S >900K. The incomplete accommodation is partly due to nonequilibrated desorption and this would be expected from detailed balance considerations (17). Since the probability of trapping decreases with increasing incident beam energy, as evidenced by the degree of specularity and velocity distributions, there will be a deficiency of high energy molecules during desorption. However, the degree of accommodation for near normal scattering at T_S = 1000K and T_S = 1195K is lower for T_B = 265K than for T_B = 615K, so there is a significant contribution from inelastic scattering. This again indicates extremely large angle inelastic scattering.

4.4.4 <u>Vibrational Energy Distributions.</u> The angular distribution of the vibrationally excited NO molecules shown in Fig. 13 is very different from that measured with the mass spectrometer or that of the ground state molecules. The lack of enhancement of the flux near the specular angle indicates that all the vibrationally excited NO originates from desorbed molecules and that the inelastically scattered molecules cannot be vibrationally excited. As with translational energy accommodation, vibrational energy accommodation is generally well accommodated, although a small but increasing deviation of the vibrational temperature from that of the surface is evident from Fig. 14. Above 1000K, the deviation is partly due to nonequilibrated desorption as happened in the case of translational energy accommodation. No explanation is offered for the small deviation below 1000K.

4.4.5 <u>Rotational Energy Distributions</u>. The rotational energy accommodation is very poor as compared with that of translational and vibrational energies. This can be seen from Fig. 15 where the accommodation coefficients γ for each mode of energy distribution are plotted as a function of the crystal temperature. The accommodation coefficient γ is defined as

$$\gamma_i = \frac{T^i_{scatt} - T^i_{incident}}{T_s - T^i_{incident}}$$

for i equal to translation (T), rotation (R) or vibration (V). The overall accommodation coefficient is high due to the strong interaction between NO and the surface. The poor accommodation for the rotational excitation may relate to the fact that NO is not a free rotor on platinum (18,19). During desorption, some of the wagging vibration energy could be transferred to NO-surface bond breaking (20) so that the desorbed molecule would be rotationally cold.

The fact that the rotational temperatures are different for the normal and specular angles is not surprising since different scattering mechanisms apply in the two cases. The fact that rotational temperature at the specular is higher seems to indicate that the inelastically scattered fraction is easier to rotationally excite than trapped molecules. When the crystal temperature is high (870K), the nonequilibrated desorption mechanism can cause the rotational distribution to be non-Boltzmann.

Finally, the importance of having complete energy exchange information for a particular system should be emphasized. Although theoretical studies of the dynamics of gas-solid interactions have proved quite successful recently for inelastic scattering (21-24), it has several shortcomings in the case of trapping-desorption scattering. Difficulties occur in the construction of accurate potential-energy hypersurfaces and because of the long interaction times for the chemically interesting systems. It is also not clear whether energy transfer to electronic levels of the substrate is important, although most of the calculations do not include this dissipation mechanism. It is, therefore, important to have a complete set of experimental results on a system so that the results can be compared with theoretical calculations.

4.5 Conclusion

The angular, translational, rotational, and vibrational energy distributions of the scattered NO molecules from the Pt(111) surface are measured as functions of incident beam energy and crystal temperature. It has been found that both trapping-desorption and inelastic scattering mechanisms apply under all of our experimental conditions, and that the trapping probability decreases as T_B or T_s increases. The inelastically scattered molecules have broad angular distribution due to strong energy transfer to the surface. The energy accommodation coefficients are nearly equal to one in the case of the translational and vibrational energy distributions for $T_s < 900K$ while they increasingly deviate from unity above this

temperature due to non-equilibrated desorption. Vibrationally excited molecules are produced by the molecules scattered by the trapping-desorption mechanism whereas inelastically scattered molecules cannot be vibrationally excited. The rotational energy accommodation is very poor as compared with the other two modes. This may be due to the fact that NO is not a free rotor on the surface and so may be cooled down further during the desorption process.

References

1. W. H. Weinberg, Adv. Colloid Interface Sci. 4, 301 (1975).

2. S. T. Ceyer and G. A. Somorjai, Annu. Rev. Phys. Chem. 28, 477 (1977).

3. J. Lapujoulade and Y. Lejay, J. Chem. Phys. 63, 1389 (1975).

4. K. C. Janda, J. E. Hurst, C. A. Becker, J. P. Cowin, L. Wharton, and D. J. Auerbach, Surf. Sci. 93, 270 (1980).

5. J. E. Hurst, C. A. Becker, J. P. Cowin, K. C. Janda, L. Wharton, and D. J. Auerbach, Phys. Rev. Lett. 43, 1175 (1979).

6. K. C. Janda, J. E. Hurst, C. A. Becker, J. P. Cowin, D. J. Auerbach, and L. Wharton, J. Chem. Phys. 72, 2403 (1980).

7. J. R. Arthur and T. R. Brown, J. Vac. Sci. Technol. 12, 200 (1975).

8. F. Frenkel, J. Hager, W. Krieger, H. Walther, C. T. Campbell, G. Ertl, H. Kuipers, and Segner, Phys. Rev. Lett. 46, 152 (1981).

9. G. M. McClelland, G. D. Kubiak, H. G. Rennagel, and R. N. Zare, Phys. Rev. Lett. 46, 831 (1981).

10. A. W. Kleyn, A. C. Luntz, and D. J. Auerbach, Phys. Rev. Lett. 47, 1169 (1981); A. C. Luntz, A. W. Kleyn, and D. J. Auerbach, J. Chem. Phys. 76, 737 (1982).

11. R. R. Cavanagh and D. S. King, Phys. Rev. Lett. 47, 1829 (1981).

12. J. W. Hepburn, E. J. Northrup, G. L. Ogram, J. C. Polanyi, and J. M. Williamson, Chem. Phys. Lett. 85, 127 (1982); D. Ettinger, K. Honma, M. Keil and J. C. Polanyi, ibid. 87, 413 (1982).

13. R. Sau and R. P. Merrill, Surface Sci. 34, 268 (1973).

14. T. H. Lin and G. A. Somorjai, Surface Sci. 107, 573 (1981).

15. C. T. Campbell, G. Ertl, and J. Segner, Surface Sci. 115, 309 (1982).

16. J. A. Serri, M. J. Cardillo, and G. E. Becker, J. Chem. Phys. 77, 2175 (1982).

17. M. J. Cardillo, M. Balooch, and R. E. Stickney, Surface Sci. 50, 263 (1975).

18. C. M. Comrie, W. H. Weinberg and R. M. Lambert, Surface Sci. 57, 619 (1976).

19. H. Ibach and S. Lehwald, Surface Sci. 76, 1 (1978).

20. W. Frost, "Theory of Unimolecular Reactions" in Phys. Chem. series V. 30, Academic Press, New York (1973).

21. R. M. Logan, R. E. Stickney, J. Chem. Phys. 44, 195 (1966).

22. Y. W. Lin and S. A. Adelman, J. Chem. Phys. 68, 9 (1978).

23. J. D. Doll, J. Chem. Phys. 59, 1038 (1973).

24. E. K Grimmelmann, J. C. Tully, and M. J. Cardillo, J. Chem. Phys. 72, 1039 (1980).

Figure Captions

Fig. 4.1 Time-of-flight distribution for an effusive 300K direct NO
beam. The solid curve is the Maxwellian distribution at 300K.

Fig. 4.2 Molecular beam-surface scattering laser-induced ionizaton
apparatus.

Fig. 4.3 Angular distributions of NO scattered from Pt(111),
T_B = 615K, T_s=1195K. The closed circles represent the
experimental data, the solid line represents a cosine
function, and the open circles represents the difference of
the data and the cosine function.

Fig. 4.4 Angular distributions for T_s=1195K, T_B = 265, 615 and
1390K.

Fig. 4.5 Angular distributions for T_B = 615K, T_s = 475, 725 and
1195K.

Fig. 4.6 Time-of-flight distributions for T_B = 615K, T_s = 475K(a)
detector sits at 7° from normal (b) specular detection. The
solid curves are the Maxwellian distributions at the
corresponding surface temperature.

Fig. 4.7 Time-of-flight distributions for T_B = 1390K, (a)
T_s = 475K, 7° from normal detection, (b) T_s = 1110K,
specular detection. The solid curves are the Maxwellian
distributions at the corresponding surface temperature.

Fig. 4.8 (a) Correlation of <KE>/2k of the scattered beam with

respect to surface temperature for T_B = 1390K. (b)

Correlation of $<\sigma^2>$ of the scattered beam with respect to

surface temperature for T_B = 1390K. The arrow on the left

indicates the value of a Maxwellian distribution.

Fig. 4.9 (a) Correlation of <KE>/2k of the scattered beam with

respect to surface temperature for T_B = 615K.

(b) Correlation of $<\sigma^2>$ of the scattered beam with respect

to surface temperature for T_B = 615K. The arrow on the

left indicates the value of a Maxwellian distribution.

Fig. 4.10 Correlation of <KE>/2k of the scattered beam with respect to

surface temperature for T_B = 265K.

Fig. 4.11 Two photon ionization spectra. The assignment represents a

one photon rovibronic adsorption of the

$A^2\Sigma^+(v'=0)\leftarrow X^2\pi_{1/2}(v''=0)$ transition. (a) Incident

supersonic beam of NO molecules; (b) room temperature

ambient NO gas at 5×10^{-8} Torr; (c) scattered NO molecules

from a Pt(111) surface at 580K.

Fig. 4.12 Rotational temperature of the scattered NO molecules as a

function of the crystal temperature.

Fig. 4.13 Angular distribution of vibrationally excited ($v''=1$) NO

molecules scattered from the Pt(111) surface, T_s = 820K.

The solid line is a cosine function.

Fig. 4.14 Vibrational temperature of the scattered NO as a function of
the crystal temperature.

Fig. 4.15 The accommodation coefficient (γ) of the three degrees of
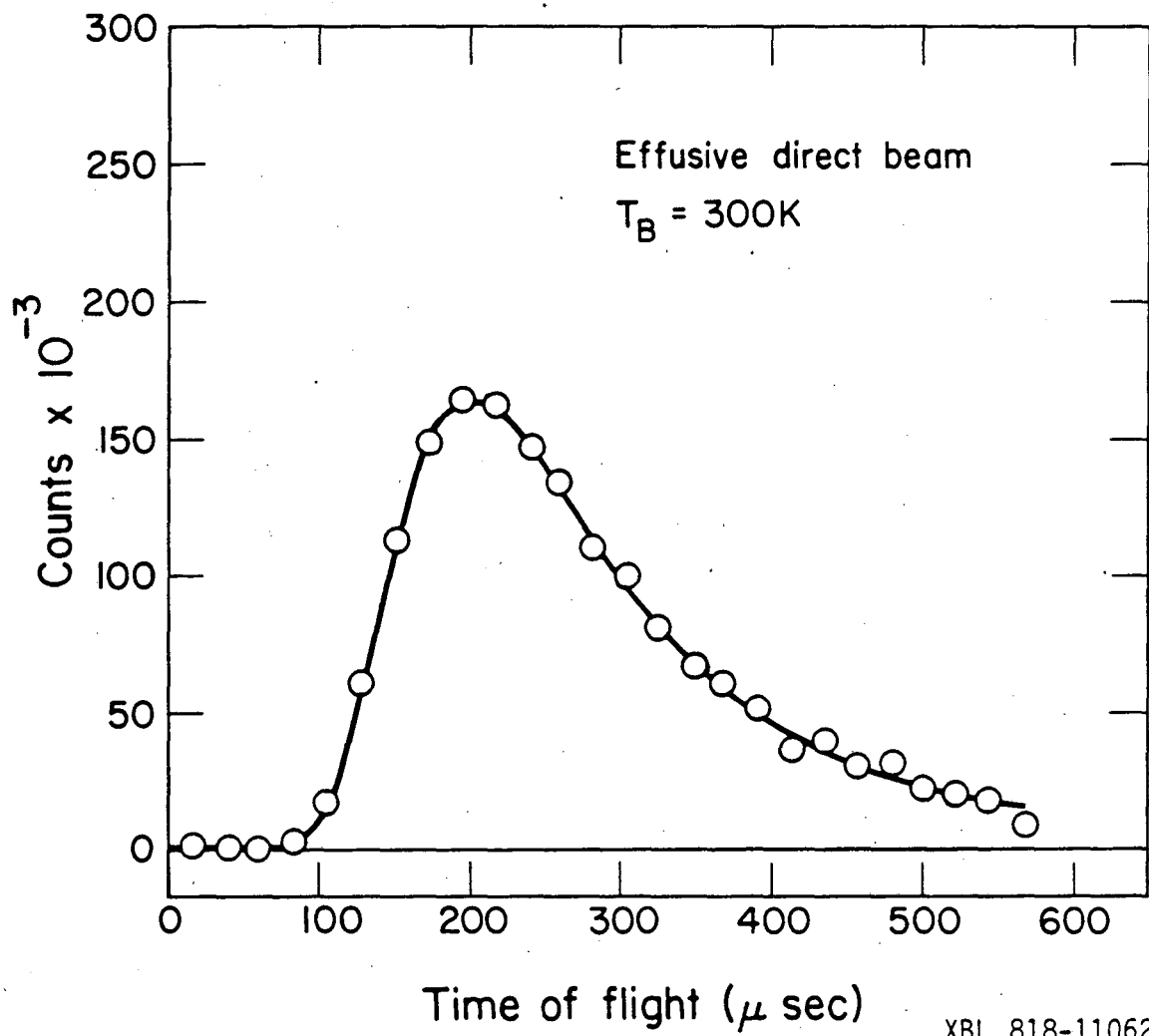freedom of the scattered NO molecules as a function of the
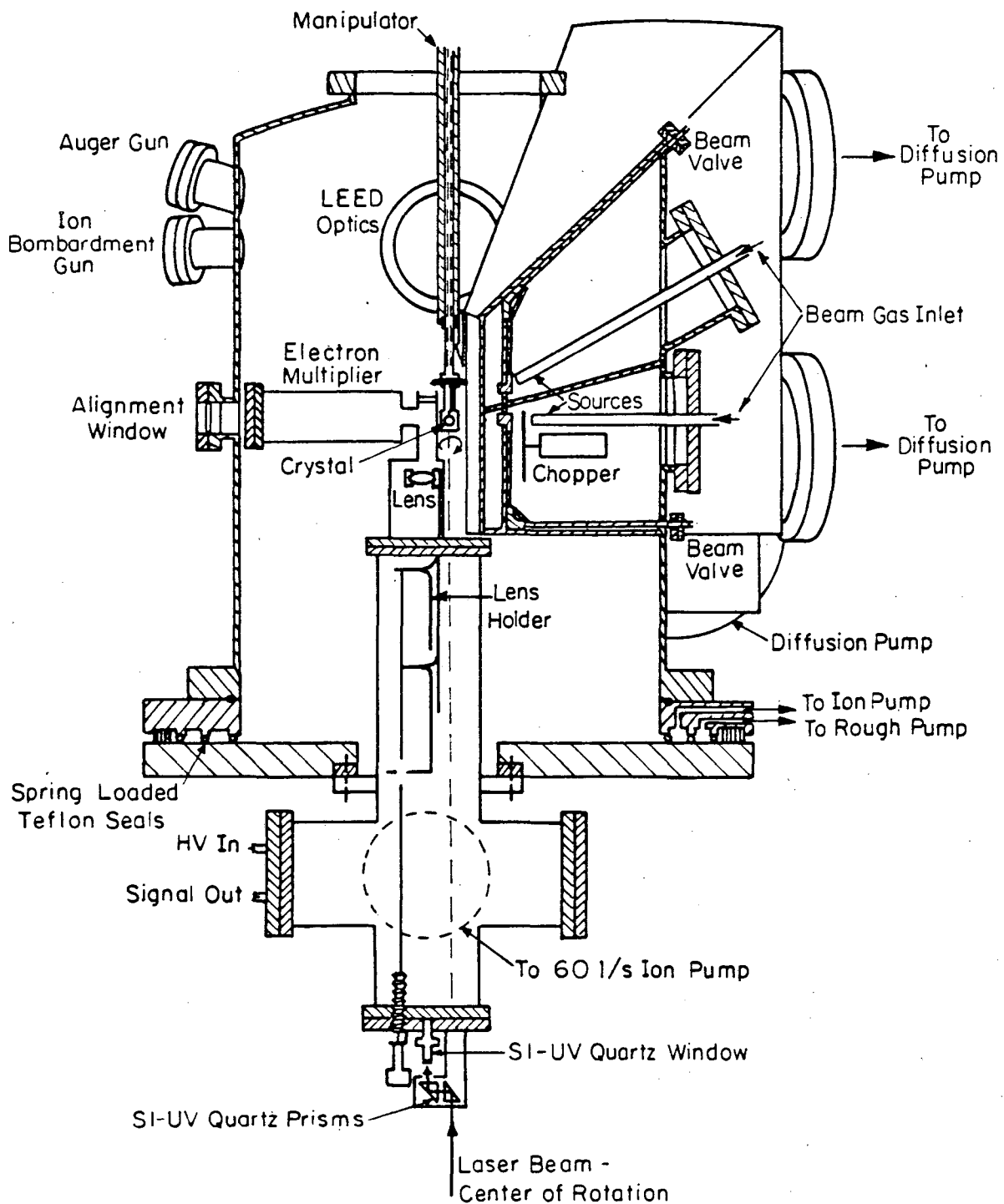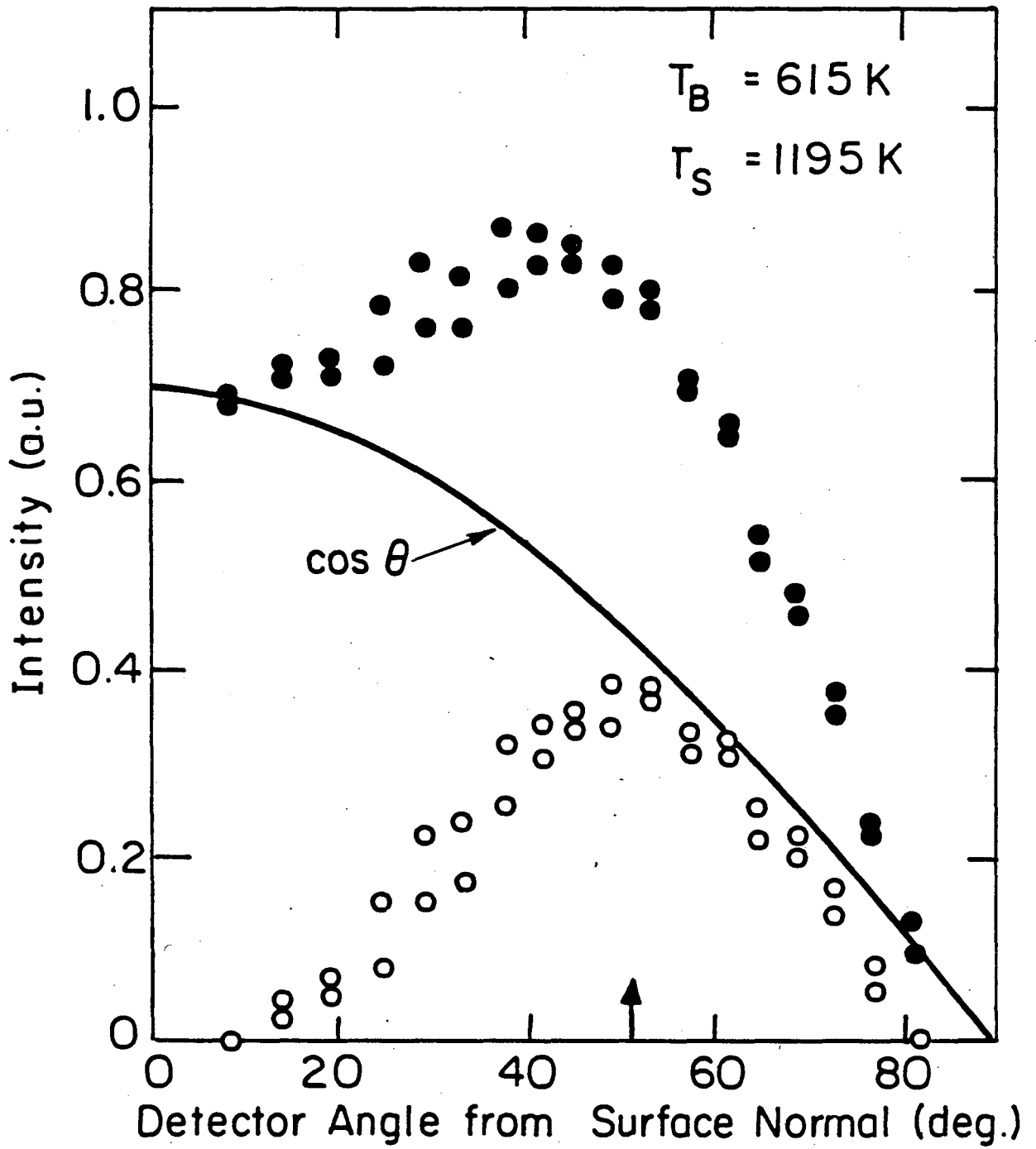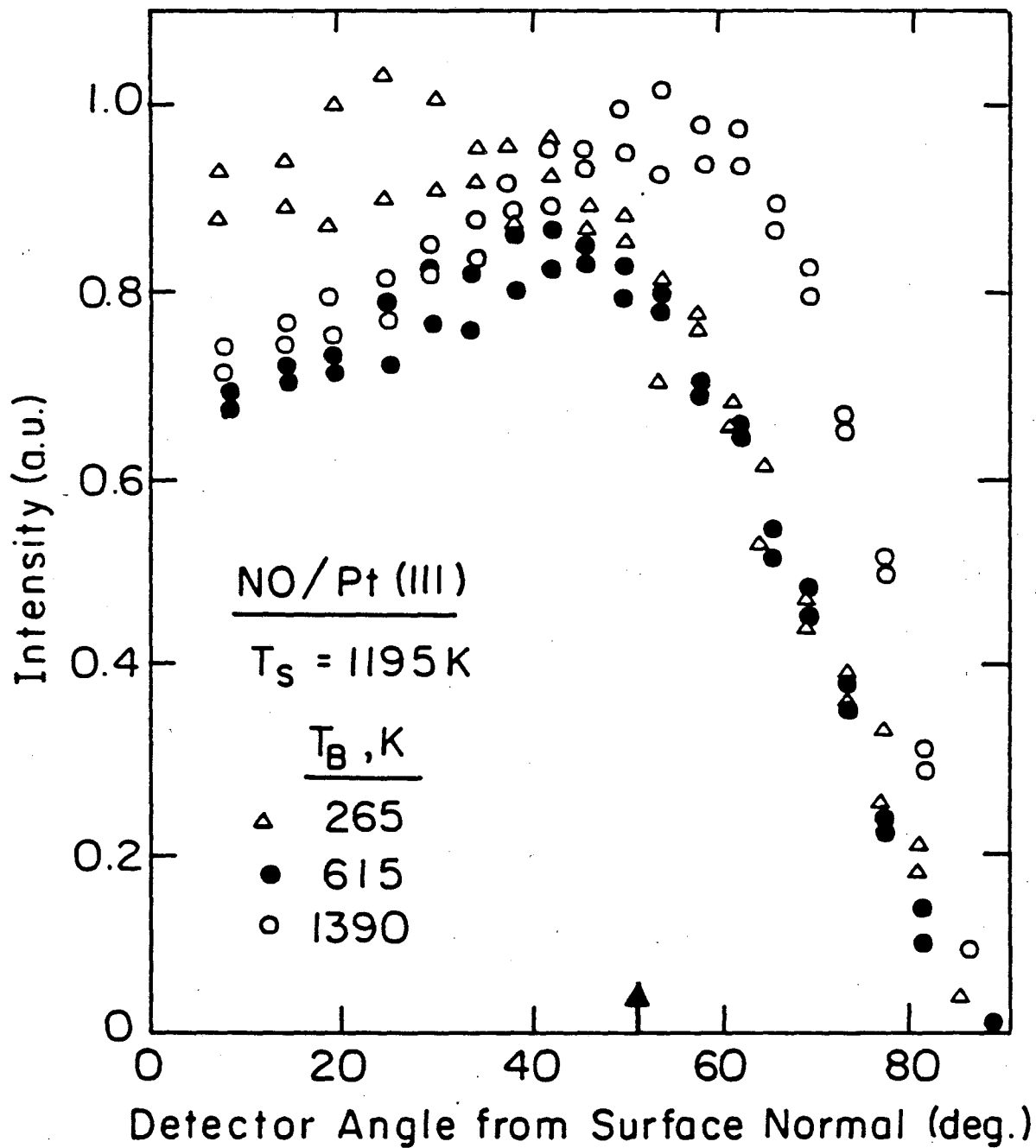crystal temperature.

Figure 4.1

Figure 4.2

XBL 823-5321

XBL 837-6005

Figure 4.3

NO/Pt (III)

$T_S = 1195 K$

T_B, K

△ 265

● 615

○ 1390

Detector Angle from Surface Normal (deg.)

Intensity (a.u.)

XBL 837-6007

Figure 4.4

NO/Pt(III)
$T_B = 615$ K

T_S, K	
●	475
○	725
△	1195

Intensity (a.u.)

Detector Angle from Surface Normal (deg.)
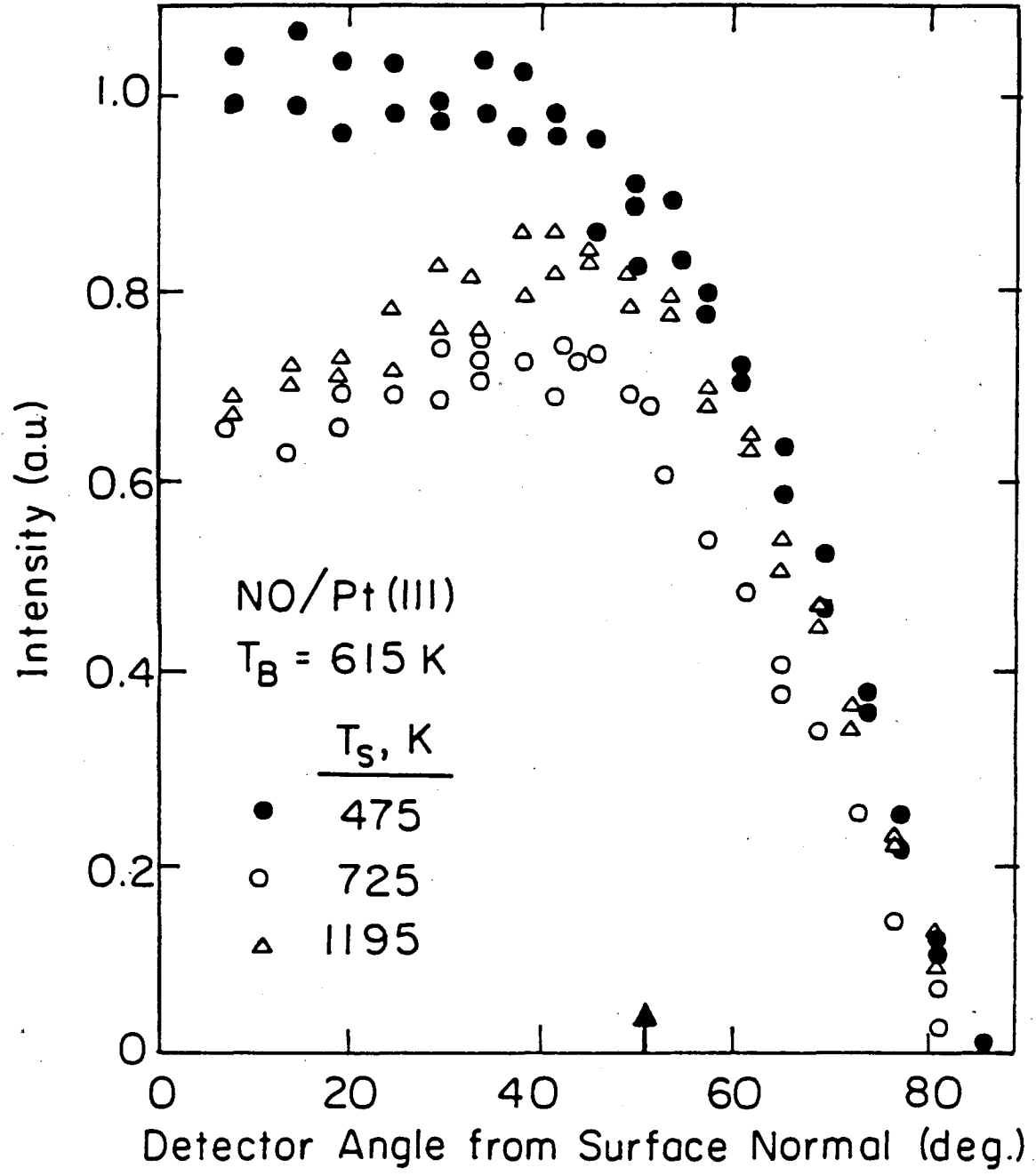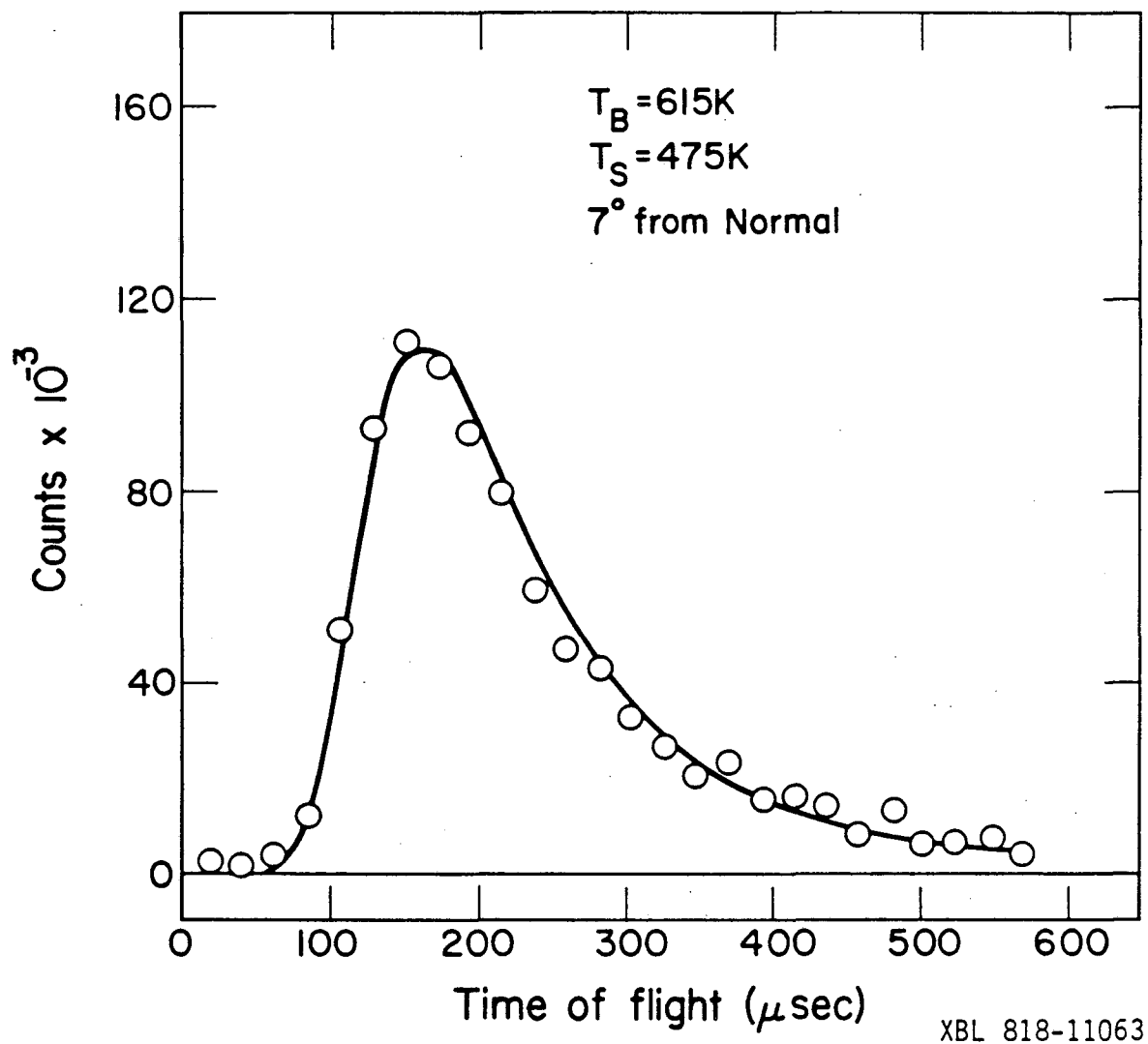
XBL 837-6006

Figure 4.5
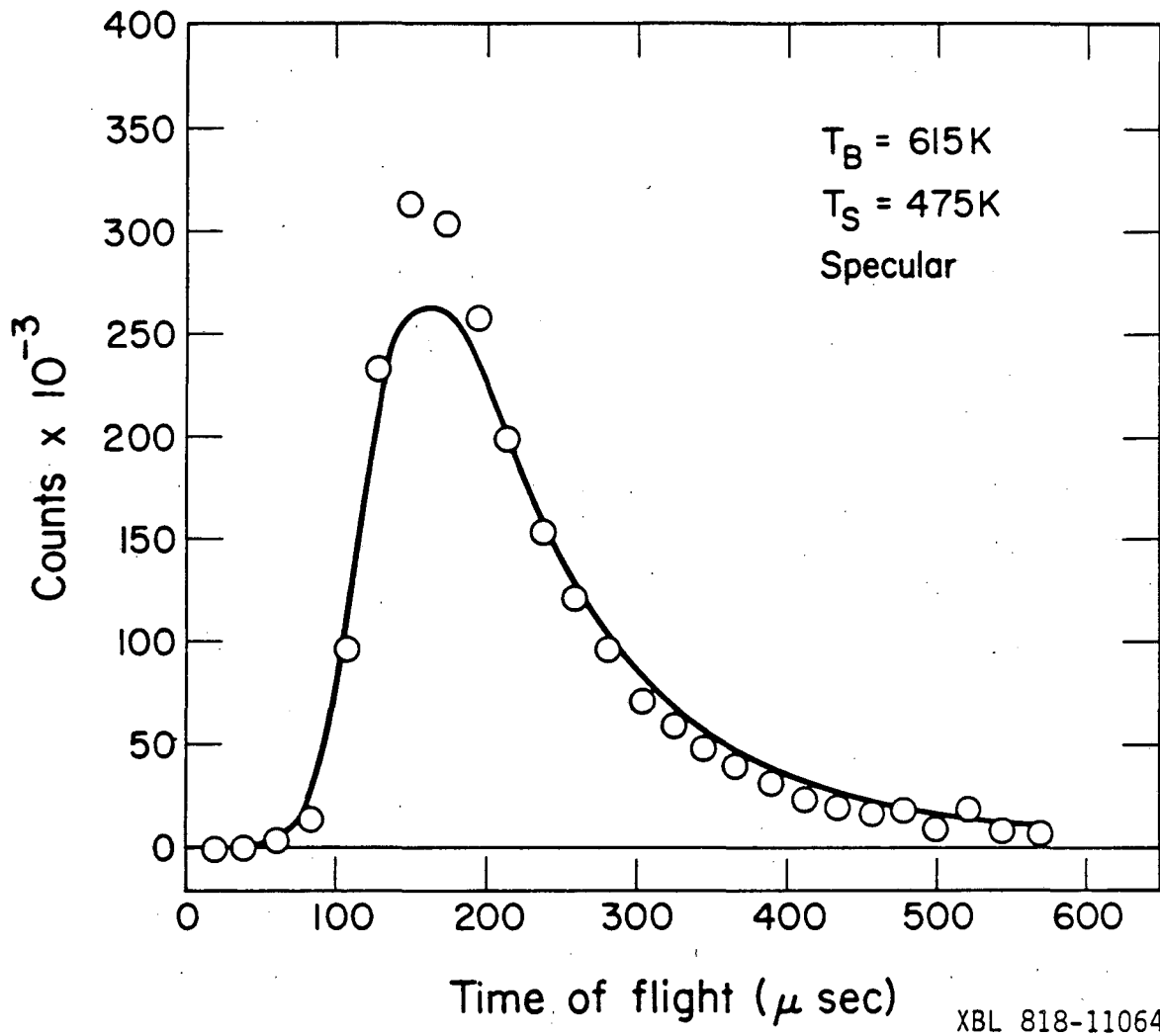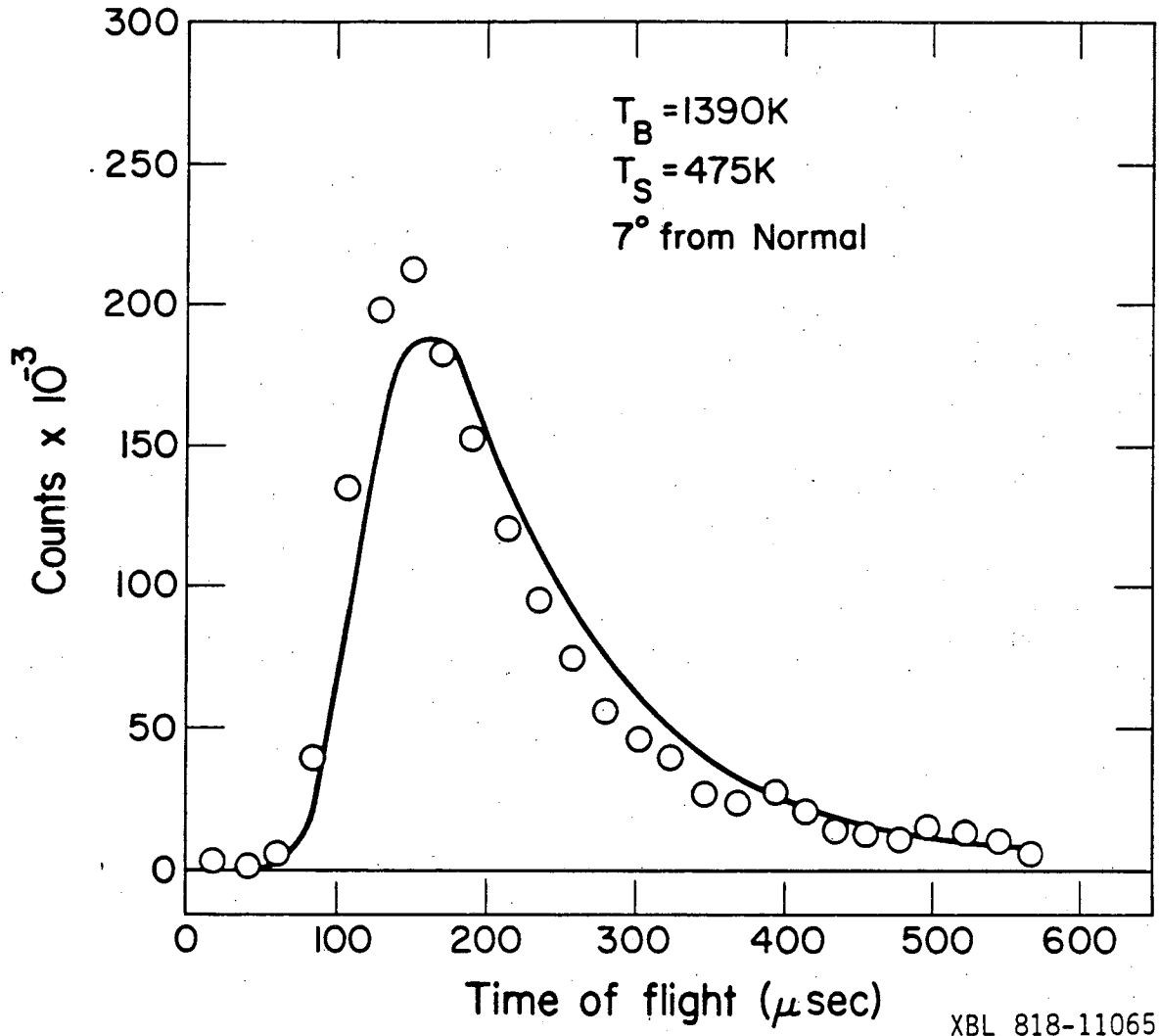
Figure 4.6a

Figure 4.6b

Figure 4.7a
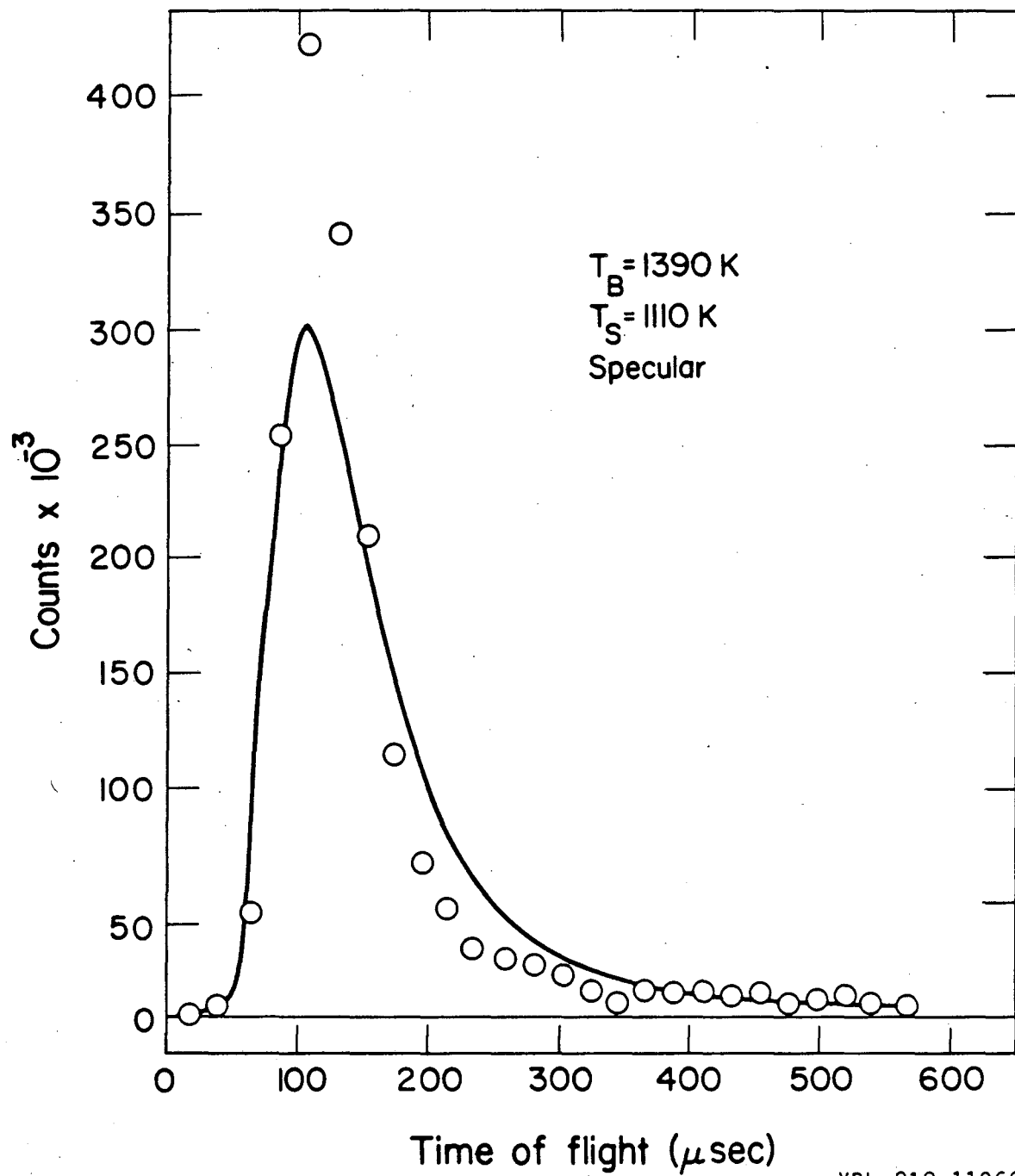
XBL 818-11065

Figure 4.7b

Figure 4.8a

XBL 818-11052

$T_B = 1390K$

○ Specular

● 7° from Normal

Surface temperature (K)
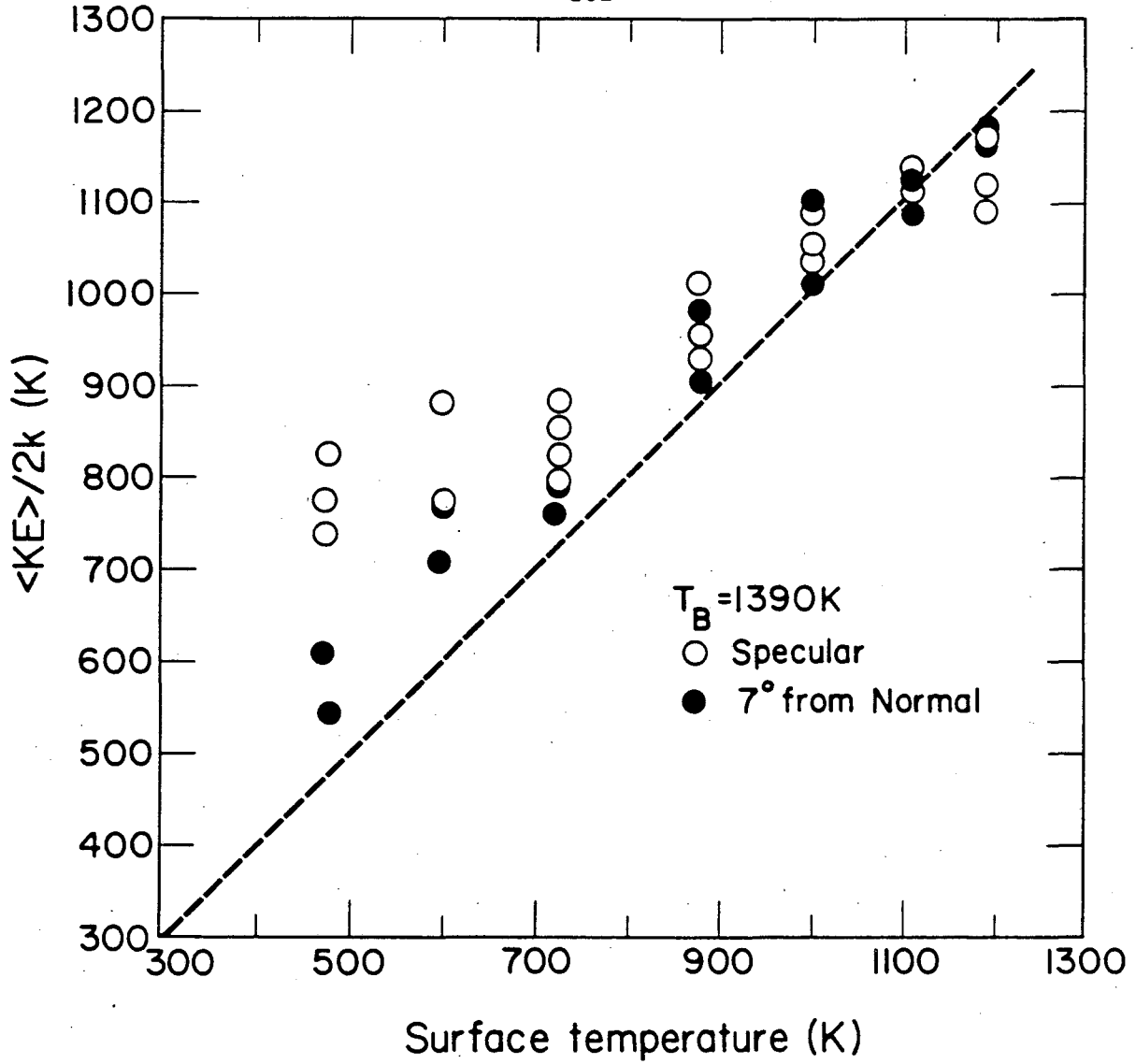
XBL 818-11051

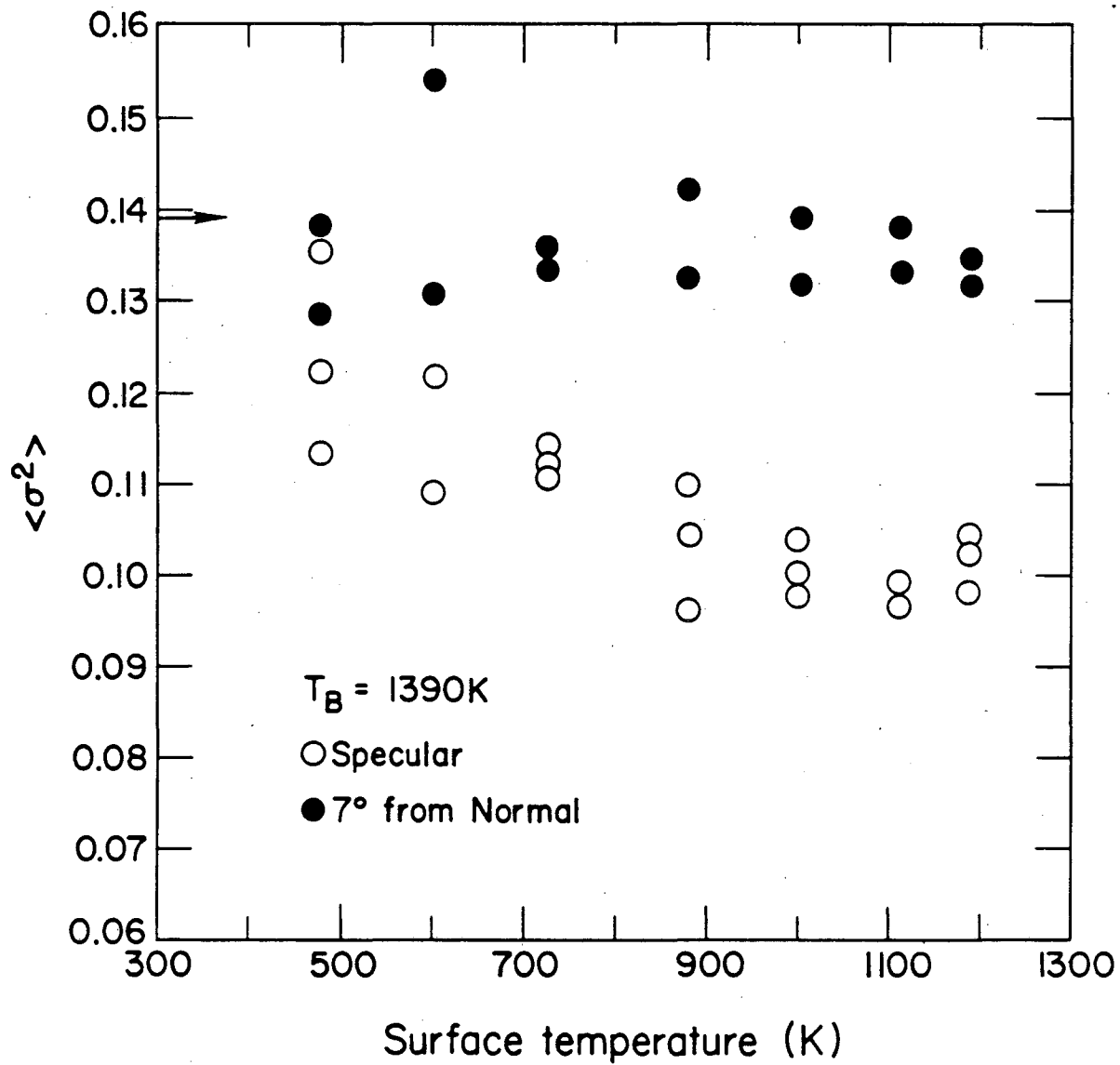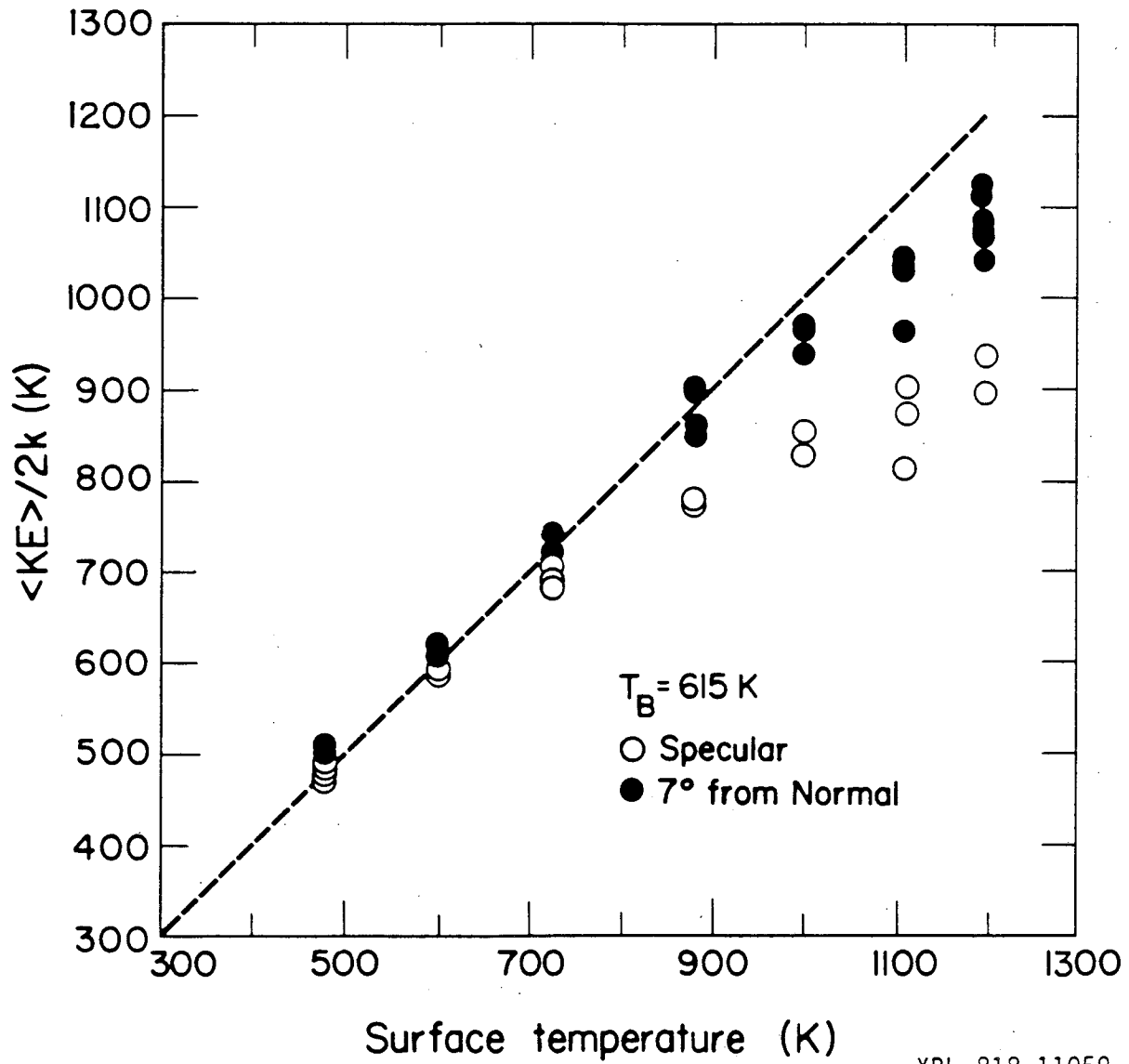Figure 4.8b

Figure 4.9a

XBL 818-11059
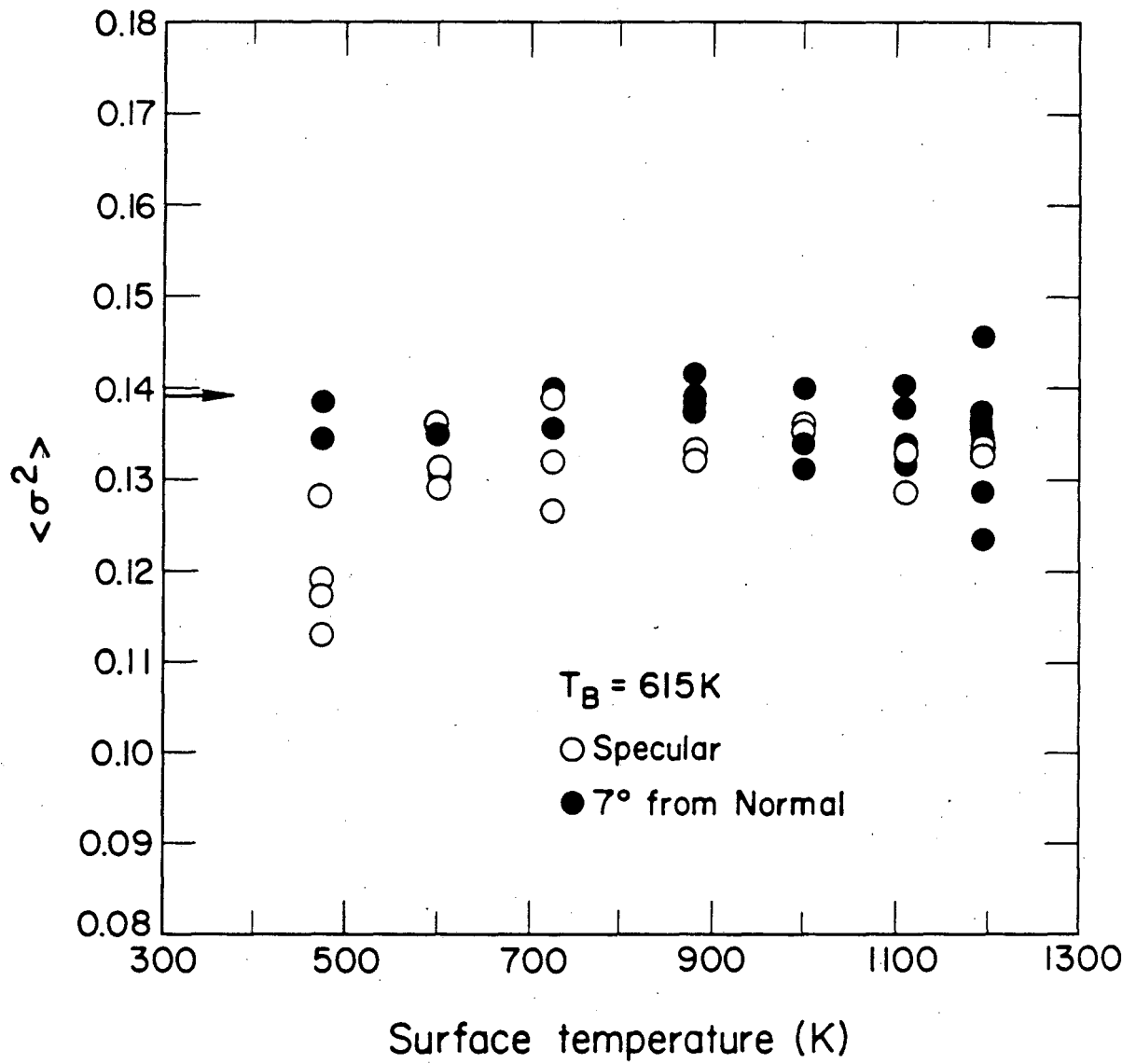
Figure 4.9b

XBL 818-11060

Figure 4.10

EXCITATION WAVELENGTH (Å)
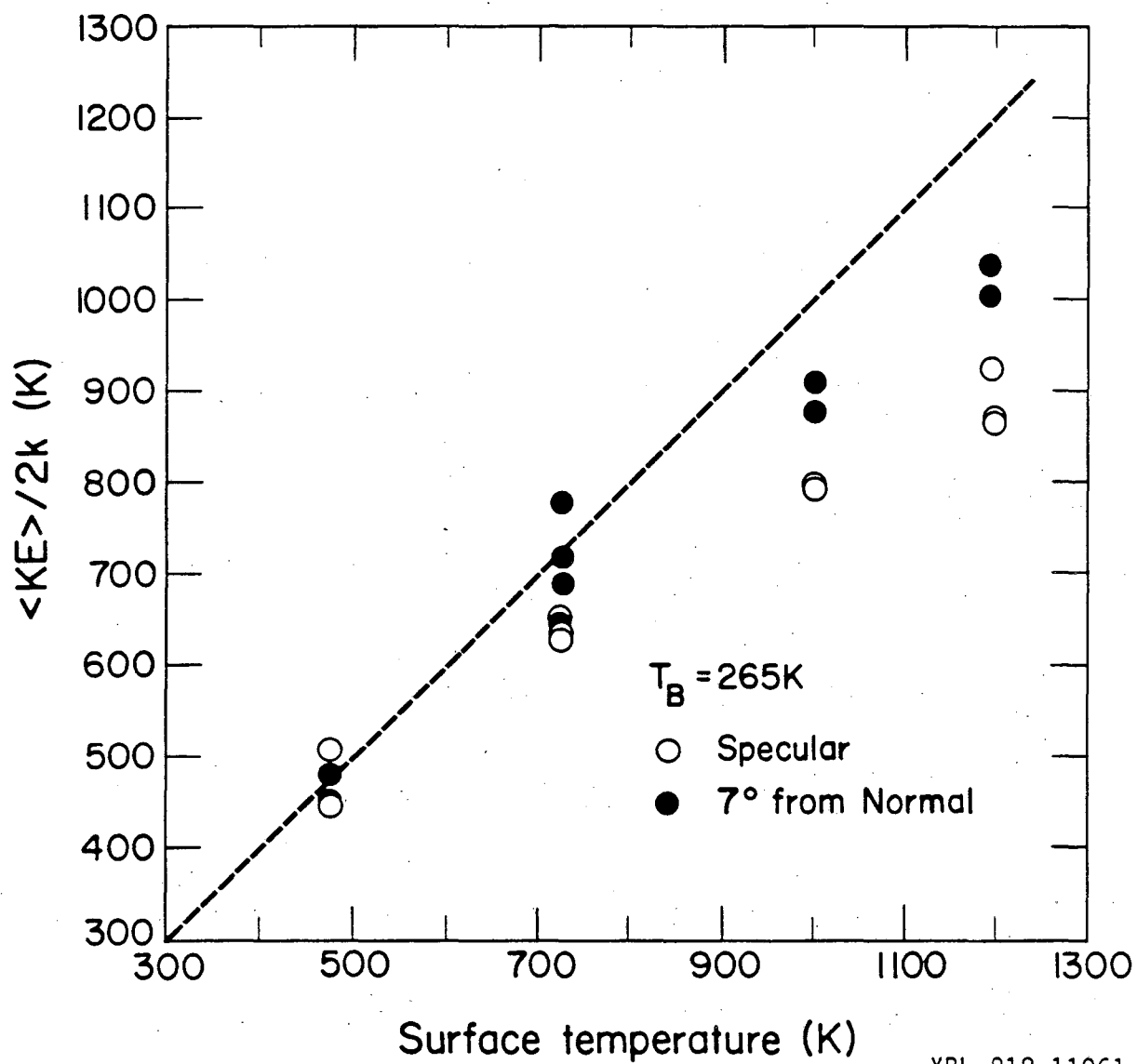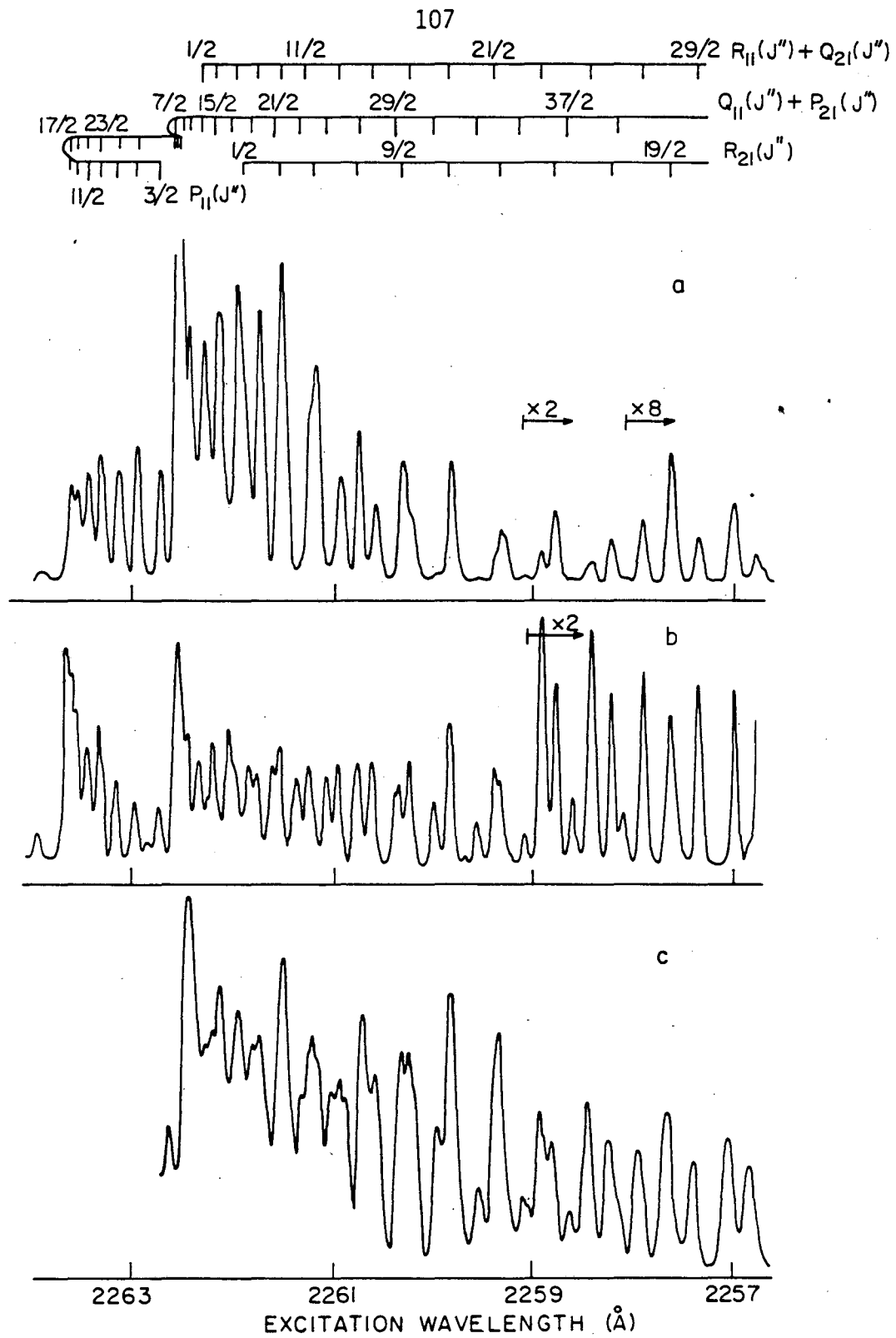
XBL 823-5393

Figure 4.11

Figure 4.12

XBL 837-6004

V″ = I

J″ = 1/2 − 6 1/2

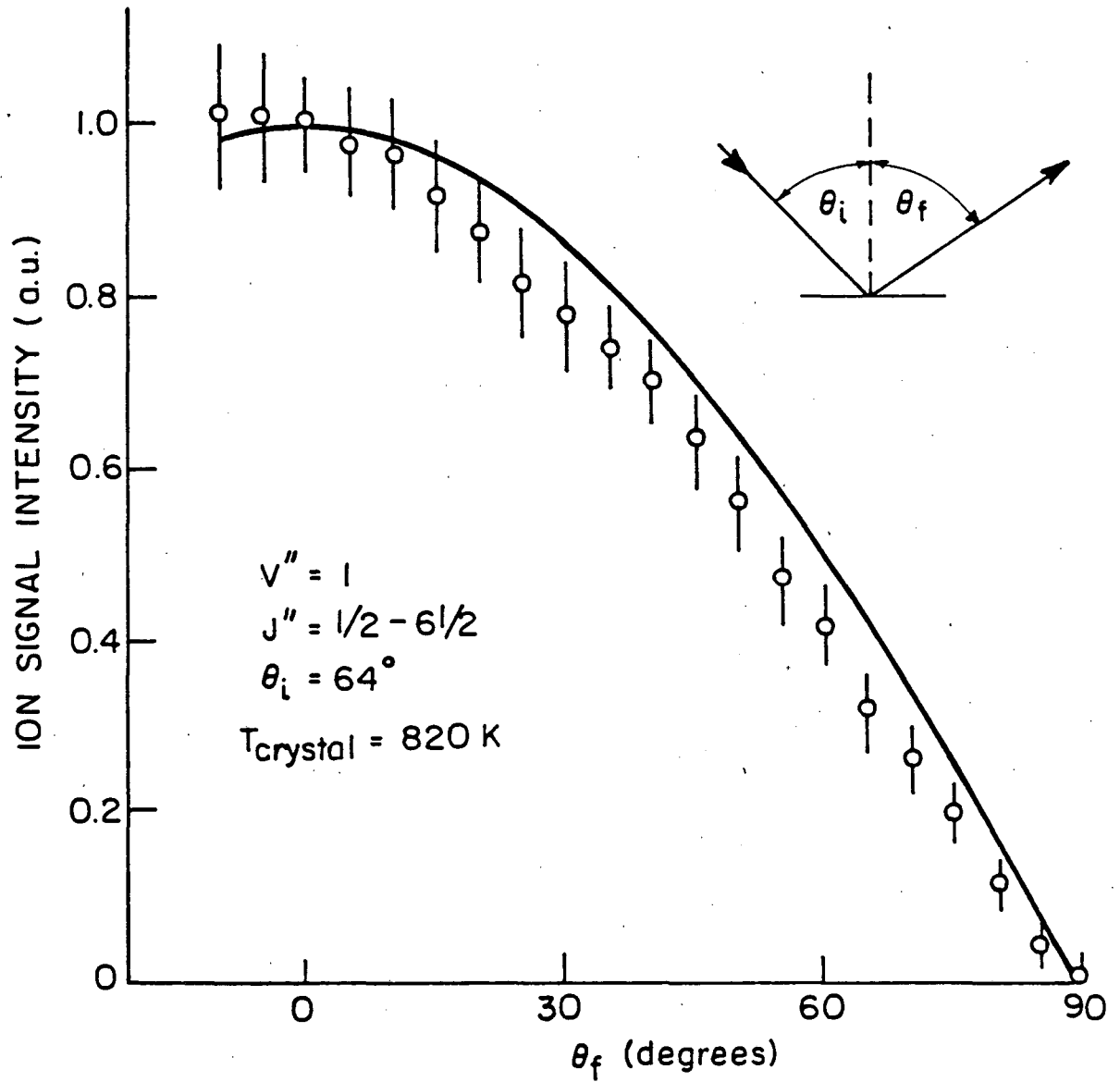$\theta_i = 64°$

$T_{crystal} = 820\ K$

θ_f (degrees)
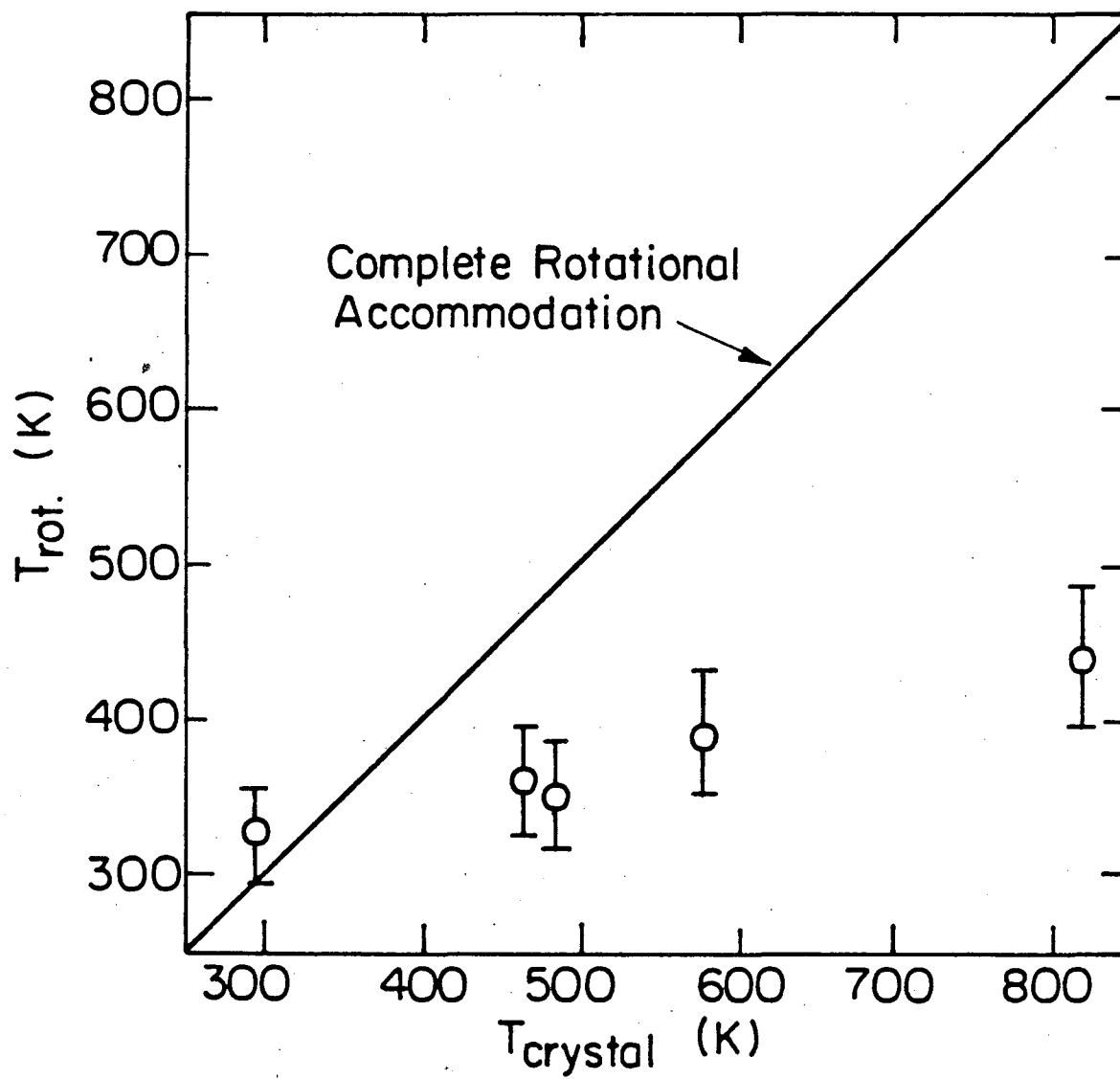
XBL823-5322
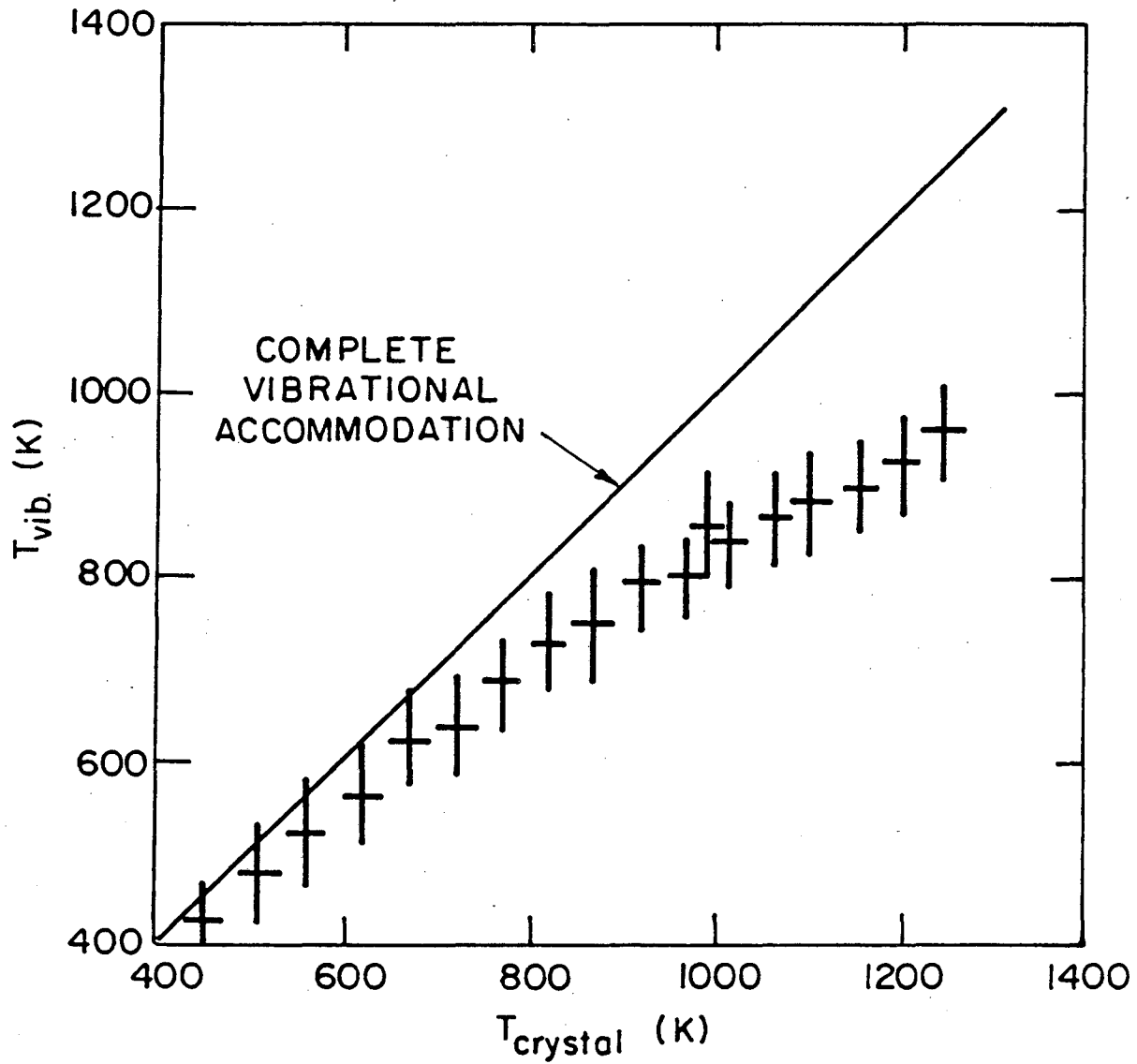
Figure 4.13
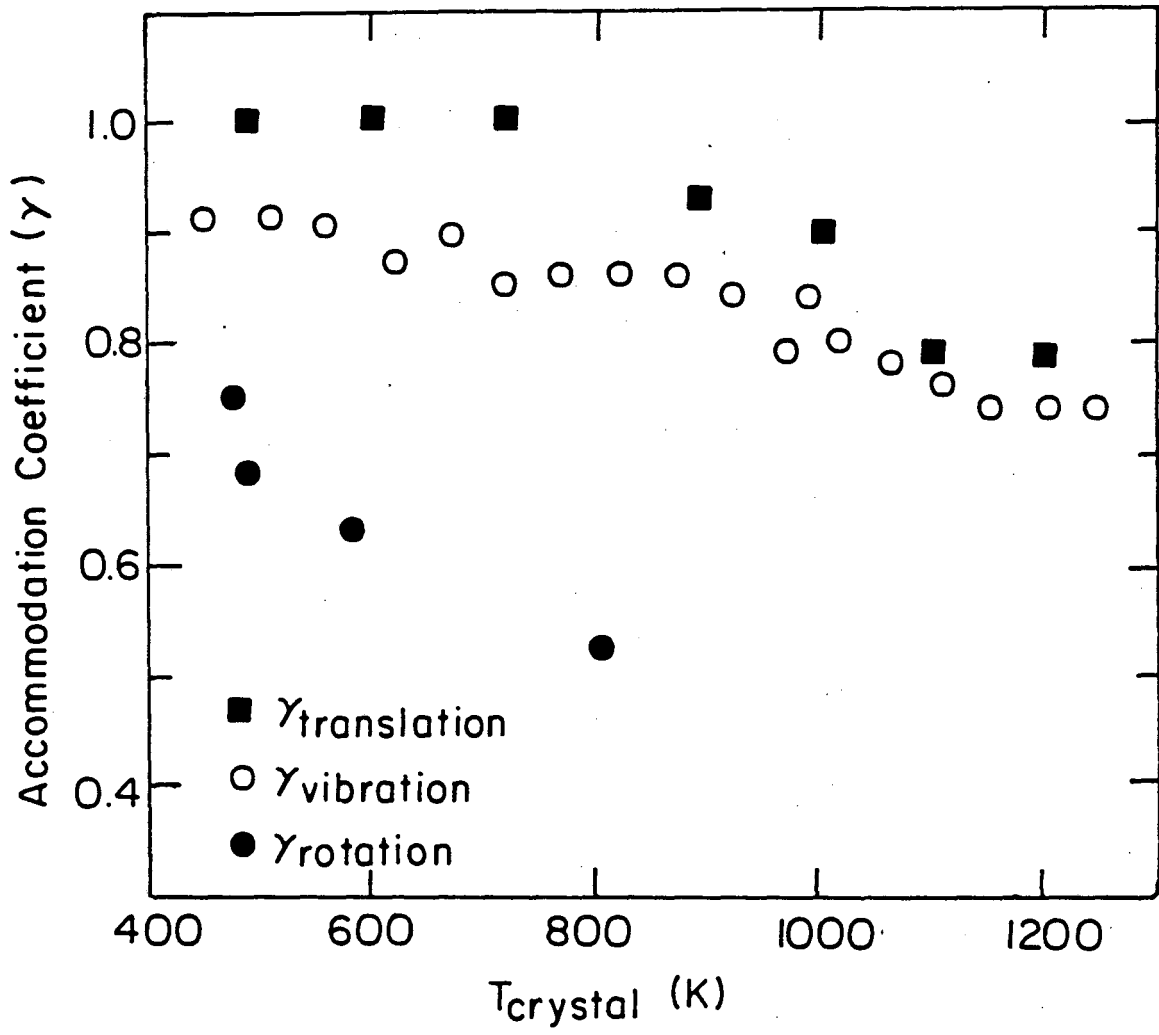
Figure 4.14

XBL 827- 6043A

Figure 4.15

CHAPTER V

HD PRODUCT ANGULAR AND VELOCITY DISTRIBUTIONS FROM THE H_2-D_2 EXCHANGE REACTION ON THE STEPPED Pt(557) SURFACE

5.1 Introduction

The study of the interaction of a molecular beam with a surface is a useful tool for understanding the dynamics of the gas–surface interactions. One way of investigating the interaction is measuring the angular distribution and velocity distribution of a reaction product as a function of the desorption angle and substrate temperature. There are many experiments that show that the angular distribution of desorbing species need not necessarily follow a cosine distribution. Also, the velocity distribution need not be Maxwellian at the substrate temperature and is often strongly desorption angle dependent (1-14). Because of these deviations from the simple laws, the results of angular and velocity distribution measurements are very useful for extracting detailed adsorption and desorption mechanisms.

Over the last few years, Comsa's group has been studying the interaction of hydrogen (deuterium) on Ni(111), Pd(100), Cu(100), and Cu(111) surfaces by measuring the angular and velocity distributions and the angular dependence of the velocity distribution of the desorbing molecules (9-13). The general features of their results are that (1) the angular distribution is peaked at the normal (2) the velocity distribution at the normal is "hotter" than the corresponding Maxwellian distribution at the substrate temperature (3) except for

the case of Cu, the mean kinetic energy decreases as one moves the detector away from the surface normal and becomes "colder" than the substrate temperature at the grazing angle of detection. Although their explanation of these results is not completely satisfactory as will be discussed in more detail in the discussion section, these results do provide a great deal of information about the associative desorption mechanisms. Since the deuterium atoms are supplied to the surface by the bulk permeation from the backside of the crystal, there is some uncertainty of the initial state, chemisorption or subsurface state, of the atoms that participate in the associative desorption.

In this chapter, the results of experiments in which HD is desorbed from the stepped platinum single crystal surface are presented. The HD molecules are produced via the H_2-D_2 exchange reaction and the reactants are supplied to the surface by two separate incident molecular beams. The angular distribution of the desorbing HD and the velocity distribution as a function of desorption angle and substrate temperature are measured. We have found that although the angular distribution is slightly peaked at the normal, the velocity distribution of the desorbing HD is slightly colder than the substrate temperature and the deviation increases as the detection angle increases. Various models explaining the results will be discussed.

Salmeron et al. have found that the H_2-D_2 exchange probability on a stepped platinum surface, Pt(s)[6(111)x(111)], is a strong function of the incident azimuthal angle (15). The reaction probability is highest when the reactants strike the open side of the

step structure, decreasing by approximately a factor of two when the inner corner of the step is shadowed. The result was explained by the geometrical variation of the number of reactant molecules that strike the open side of the step structure and cannot be attributed to an activation energy barrier for adsorption. The incident azimuthal angle dependence of the reaction probability is also observed on Pt(s)[6(111)x(100)] which has (100) step structure rather than (111). The time-of-flight results support the explanation suggested by Salmeron et al. (15).

5.2 Experimental

The apparatus is the modified system described in Chapter 2. The two supersonic sources were operated at a stagnation pressure of 100 Torr which gave the highest beam flux. Occasionally, the effusive sources were used to vary the incident beam energy. The single crystal Pt(557) surface, Pt(s)[6(111)x(100)], is cleaned by argon ion sputtering and annealing. The cleanliness is determined by AES. The orientation of the crystal is determined by helium diffraction described in Section 2.4. For most of the experiments, the primary beam is incident at an angle of 70° from normal, oriented along the stepped edge and the secondary beam is incident at an azimuthal angle of 30 degrees from the open side of the step.

The initial channel of the time-of-flight distribution is determined by obtaining a TOF distribution using a helium-neon laser as the incident beam and a photo-multiplier as the detector. Since the speed of the light can be considered to be infinite, the channel

of the peak signal is the initial channel of the TOF distribution. The initial channel has to be redetermined whenever the photodiode and light emitting diode support is remounted since their position would possibly shift slightly.

The angular distributions and TOF distributions of the product HD were measured at several substrate temperatures and detector angles. The data accumulation time for the TOF distributions varied from 1 hour to 6 hours depending on angle of detection and the substrate temperature. The crystal was sputtered with argon ion after one hour data accumulation and the only contamination was carbon which is less than .05 monolayer after completing the experiments.

5.3 Results

In Fig. 1 I present the angular distribution of HD produced by the H_2-D_2 exchange reaction on Pt(557) at a substrate temperature of 690K. The angle of incidence of the primary beam is 60 degrees from the surface normal. The dashed line is the cosine function and the solid line is the square of the cosine function. One can see that the number density distribution of the HD is proportional to the square of the cosine of the desorption angle. As will be shown below, the average energy of the desorbing HD decreases as the desorption angle increases. Therefore, if the relative molecular flux is plotted as a function of the desorption angle, the angular distribution will be even sharper than a $\cos^2\theta$ distribution.

A typical time-of-flight distribution is shown in Fig. 2. The open circles represent the experimental data and the solid line a corresponding Maxwellian distribution at the substrate temperature (690K). It is evident from the figure that the desorbing HD is slightly colder than the substrate. The average kinetic energy of the HD flux divided by 2k (Boltzmann constant) has been calculated in the same way as in Chapter 4 and is about 480K for this distribution. The results for other substrate temperatures are shown in Fig. 3. The open circles represent the average kinetic energy divided by 2k at various crystal temperature. The angle of incidence of the primary beam is 70 degrees with respect to the surface normal. If the desorbing HD is equilibrated with the surface, the experimental result should lie along the dashed line. However, the average kinetic energies divided by 2k are always lower than the substrate temperature when the temperature is varied between 500 and 1170K, and the average kinetic energy is proportional to T_s over the temperature range. All the TOF distributions are slightly wider than the corresponding Maxwellian distributions at their average temperatures.

The dependence of the mean HD kinetic energy on polar angle is presented in Figs. 4 and 5. Figure 4 shows examples of two TOF distributions. In both cases, the substrate temperature is 690K and the angle of incidence is 60 degrees. The closed circles represents the TOF distribution for normal detection, and the open circles the TOF distribution for detector at 60 degrees from the surface normal.

The peak of the $\theta_D = 0°$ (closed circles) distribution occurs at a shorter flight time than that of the $\theta_D = 60°$ (open circles) distribution. This implies that HD molecules desorbing normal to the surface have a higher average kinetic energy than those desorbing at 60° to the normal. The average kinetic energy divided by 2k as a function of the HD desorbing angle is shown in Fig. 5, and, as can be seen, as the desorption angle increases, the average kinetic energy decreases.

As mentioned above, the reactivity of the H_2-D_2 exchange reaction has been found to be a strong function of the incident beam azimuthal angle for the stepped surface, Pt(s) [6(111)x(111)] (15). The maximum reactivity is observed when the incoming molecules are incident onto the open side of the step. A similar result is found with Pt(s)[6(111)x(100)] as can be seen in Fig. 6, where HD intensity is plotted as a function of azimuthal angle (the zero of azimuthal angle is also shown in Fig. 6).

In order to see if the average kinetic energy of the desorbing HD depends on the azimuthal desorption angle, the following experiment was carried out. With 45° polar angle and zero degree azimuthal angle detection, a TOF distribution was taken for 70° incident angle at a surface temperature of 690K. Without changing any experimental conditions except rotating the azimuthal angle of the crystal such that the detector is at 45 degrees polar angle and 90 degrees azimuthal angle, another TOF distribution is obtained. Within the experimental error, no difference is observed between these two distributions.

The rate of the HD production is found to be independent of substrate temperature above 650K and to decrease rapidly below 650K. We also observed that the average kinetic energy of the desorbing HD does not depend on incident beam energy. This was determined by varying the incident beam energy by replacing the supersonic sources with effusive sources operating at a stagnation pressure of 2 Torr behind 1 mm diameter nozzles.

5.4 Discussion

The following experimental findings indicate that the H_2-D_2 exchange reaction occurs via a Langmuir-Hinshelwood (LH) rather than an Eley-Rideal (ER) mechanism. In other words, the HD molecules are formed via reaction between adsorbed species. If the ER mechanism was to operate, one would expect that the angular distribution of the product should peak towards the specular angle, and that the kinetic energy of the products should depend on the incident beam energy but only very weakly on the substrate temperature. Since the angular distribution is $\cos^2\theta$, the kinetic energy of the products does not depend on the incident beam energy but is proportional to the substrate temperature, it is concluded that the reaction proceeds via a LH mechanism. This mechanism is also believed to hold for the H_2-D_2 exchange reaction on other platinum and transition metal surfaces (16-18).

It has been found by bound level resonances of HD scattered from Pt(111) surface that the heat of adsorption of a HD molecule is about 1 kcal/mole (19). Assuming that heats of adsorption of H_2, HD, and

D_2 on the platinum surface are reasonably similar, it can be concluded that the heats of adsorption of H_2, HD and D_2 will be no more than 5 kcal/mole greater even at the step site. The heat of dissociative adsorption is much greater than that of molecular adsorption. Although the reported heat of dissociative adsorption varies somewhat depending on measurement techniques, it is about 20 kcal/mole. In the following discussion a value obtained by Comsa's group (20) will be used, so that values for heats of dissociative adsorption of 22 kcal/mole at the step site and 19 kcal/mole on the terrace are assumed.

Since the surface temperature at which the H_2-D_2 exchange reaction was carried out is high, only the dissociative adsorption states of H_2 and D_2 are significantly populated. Thus, it is believed that the HD molecules are formed by the recombination of the adsorbed H and D atoms. This was also concluded by other authors (18,20-25). The recombination is most likely to take place at the step edges since the residence time of H and D atoms is likely to be greater at these sites.

The next step is to explain the $\cos^2\theta$ angular distribution, the angular and substrate temperature dependence of the mean kinetic energy within this reaction model framework. One of the frequently used models, proposed by Van Willigen (1), assumes an activation barrier for adsorption parallel to the surface as show in Fig. 7(a). Therefore, only those molecules with a sufficiently large component of momentum normal to the surface can escape. This model predicts that

the average kinetic energy of the desorbing molecules will be higher
than the corresponding Maxwellian distribution at the substrate
temperature and the angular distribution of the product will be peaked
in the normal direction. It also predicts that the average kinetic
energy of the desorbing molecules increases as the desorption angle
changes from normal to parallel to the surface. Thus, this model
cannot explain the experimental observations that the average kinetic
energy decreases as the detector moved from normal to grazing
direction and that the mean kinetic energy is slightly colder than the
corresponding Maxwellian distribution at the substrate temperature.

Another model, proposed by Comsa, assumes that the Van Willigen's
activation barrier is not constant but contains "holes" through which
a finite fraction of the incident molecules may dissociatively adsorb
without an activation energy (10). Therefore, the desorbing flux is a
mixture of molecules having overcome the activation barrier and of
molecules desorbed through the holes. The former fraction has an
angular distribution peaked at the normal and will only contribute
significantly to the desorbing flux at the surface normal. The latter
fraction has a cosθ angular distribution and will dorminate the
desorbing flux at grazing angles. Since the latter fraction surmounts
no activation barrier, it could well desorb at a "colder" temperature
than that of the surface according to detailed balance arguments (26)
and theoretical calculations by Tully (27). Consider a gas and
surface at equilibrium and no activation barrier for adsorption.
Molecules incident onto the surface with high velocities might be

expected to have a lower probability of sticking than low energy incident molecules. By detailed balancing the molecules which have equilibrated on the surface and subsequently desorb will be "colder" than the surface.

This model seems able to explain our results if we assume that the fraction which overcomes no activation barrier is the dominant fraction even in the normal direction and desorbs at "colder" than surface temperature. The $\cos^2\theta$ angular distribution is a combination of a distribution peaked at normal from the fraction which involves activated desorption and a cosine angular distribution which involves no activation barrier. At grazing angle, the average kinetic energy is colder than that at the normal since the main contribution to the flux at the grazing angle is from the fraction which overcomes no barrier. At the normal, the average kinetic energy is still colder than the corresponding substrate temperature which may be because the fraction which surmounts the barrier is still the smaller fraction.

The substrate temperature dependence of the average kinetic energy is more difficult to explain. If the "cold" desorbing molecules is indeed due to non-equilibrium desorption, then the average kinetic energy divided by 2k should deviate from the substrate temperature more and more as the substrate temperature increases (27), while we observe that the average kinetic energy is proportional to the substrate temperature in the range of 600K to 1050K.

The most difficult problem with Comsa's model is as follows. The activation barrier can be deduced by measuring three quantities; the

average kinetic energy, the angular distribution and the sticking
coefficient as a function of the incident beam energy. The activation
barrier deduced from these three quantities are in poor agreement
(12,13). Because of this, it was necessary to assume that the D atoms
recombine in a subsurface state and desorb immediately without
equilibrating in a chemisorbed state (12,13). The main drawback with
this assumption is that there is probably no molecular subsurface
state, so that, direct subsurface recombination seems unlikely.

Another problem with Comsa's "activation barrier with hole" model
is pointed out by Horton and Masel (28,29). They have found that
flash desorption spectra are not angular dependent. According to the
"activation barrier with holes" model, one would expect the peaks of
the flash desorption spectra to shift to lower temperature on moving
the detector from the normal to grazing angle. Horton and Masel did
provide a model which concludes that the molecules could desorb
preferentially in the surface normal direction if the surface is
sufficiently corrugated in the region of the desorption site.
However, as the authors have pointed out, the model should predict
that the angular distribution of the desorption flux will vary with
crystallographic and azimuthal orientation, however, no variations
have been observed. Indeed, Salmeron et al. (18) have found that the
angular distributions of HD produced from the stepped Pt(332) crystal
surface have $cos^2\theta$ form for two azimuthal angle orientations, $\Phi = 0°$
and 90°. Balooch and Stickney have also found that the angular

distributions of H_2 desorbed from the copper surfaces are not azimuthal angle dependent (7).

The model which can explain our results satisfactorily is proposed in the following. Figure 7(b) is the one dimensional potential energy diagram for H_2/Pt and H/Pt. E_1-E_2 is positive in this figure but could be negative for other systems when there is an activation energy barrier for dissociative adsorption as shown in Fig. 7(a). There are systems which are believed to have positive E_1-E_2 even though the angular distributions of the associative desorption are $\cos^2\theta$ (18,30). The fact that the desorbing HD is slightly colder than the substrate leads us to believe that this is plausible. The shaded area in Fig. 7(b) is where both atomic and molecular states can coexist, so that this is where recombination is expected to occur.

Because there is no activation barrier for the dissociative adsorption, the Van Willigen model implies unit sticking coefficient since all the molecules can dissociate before they encounter the repulsive molecular potential. However, this is not the case because there is only a certain probability for those molecules in the shaded area to dissociate and be trapped in the atomic potential well. Experimental evidence can be seen from O_2/Pt(111) (30) and H_2/Pt(332) (18), where these two systems have no activation barrier for dissociative adsorption while the sticking coefficients are less than one.

Now, let us consider the associative desorption process. Since the recombination can occur only in the shaded area, and if H and D recombine in the region of low potential energy, the HD produced will immediately feel a repulsive force from the molecular potential. This repulsive force is most likely to be normal to the surface and if it is strongly repulsive, the HD will have unsufficient time to equilibrate and will desorb with an angular distribution peaked at the normal, and its mean kinetic energy will be higher at the normal than at the grazing angle. At the normal direction, the average kinetic energy divided by 2k could be higher or lower than the substrate temperature depending on the potential energy at which recombination occurs. Of course, if E_1-E_2 is negative, as shown in Fig. 7(a), then there is an activation barrier for the dissociative adsorption and the recombination can occur only in the high potential energy region, so that the product will desorb at "higher" temperature than that of the substrate. The substrate temperature dependence of the mean kinetic energy is easier to explain with this model. As the substrate temperature increases, the atomic H and D are excited up in the atomic potential well and recombine at higher potential energy level, so that it is reasonable that the mean kinetic energy of the desorbing HD be proportional to the substrate temperature.

This model seems to explain satisfactorily the peaked angular distribution and the angular dependence of the mean kinetic energy of the desorbing product. The model is based on the fact that H(D)-Pt bond length is shorter than the distance between the trapped molecular

hydrogen and the surface, thus, H and D will recombine near the repulsive molecular potential and feel the normal repulsive force immediately after forming HD. Theoretically, Tully (31) has found that CO produced from atomic oxygen reacting with adsorbed carbon has an angular distribution that is peaked at the surface normal and its normal component of translational energy is considerably higher than the tangential component. The result was interpreted by the fact that CO feels the repulsive interaction with the surface at short C-Pt distances corresponding to the adsorption site of the carbon atom. The experimental facts of hydrogen recombination on nickel (9) and CO oxidation on platinum (32) are consistent with this model.

The rotational and vibrational energy distributions of the HD desorbing from the surface might be important in the interpretation of our experimental results. Unfortunately, no such information is available, so that, it is not appropriate to discuss in detail how rotational and vibrational energy distributions affect the product translational energy distribution. However, one can expect that if the axis of the HD molecules is at 45° to the surface normal immediately after formation, it is possible that the repulsive force will excite rotation and produce a cold translational distribution.

The fact that the reactivity of the H_2-D_2 exchange reaction increases as the azimuthal angle of the incident beams increases is similar to the result on the Pt(s)[6(111)x(111)] surface (15). Since our crystal surface is Pt(s)[6(111)x(100)], this property appears to be the same for both (100) and (111) orientation steps. Although the

step structures might influence the exchange probability somewhat, the steps, no matter what structures they are, are probably the main cause of the high exchange probability. Tsang and Falicov have calculated H-H bond breaking activity for the different sites on a stepped Pt(557) surface and found the most active site is that associated with the inner corner atom of the step (33). Based on this calculation, Salmeron et al. explained the azimuthal angular dependence by the geometrical variation of the number of reactant molecules that strike the open side of the step structure, which is more active for H-H bond breaking (15). We believe this is the case and applicable to our angular dependence observation with further support from the fact that the mean kinetic energy of the desorbing HD is not azimuthal angle dependent. If the variation of the exchange probability with respect to the incident azimuthal angle is due to the variation of the activation energy barrier for bond breaking, the desorbed HD velocity should not be independent of the azimuthal angle of desorption.

5.5 Conclusion

The angular and velocity distributions of the HD produced from the H_2-D_2 exchange reaction on Pt(557) surface have been measured. The fact that the angular distribution is peaked at the normal and that the average kinetic energy of the product does not depend on the incident beam energy but is proportional to the substrate temperature indicates that the reaction proceeds via a Langmuir-Hinshelwood mechanism that is reaction between two adsorbed hydrogen atoms. Although HD desorbs with $\cos^2\theta$ angular distribution, its average

kinetic energy corresponds to a temperature slightly colder than that of the substrate. As the desorption angle increaes, the mean kinetic energy of the desorbing molecules decreases. Comsa's "activation barrier with holes" model can explain most of the results but some difficulties exist with the model. An alternative more satisfactory model is proposed. This assumes that as soon as H and D recombine, they will immediately feel a repulsive force which is most likely perpendicular to the surface.

The H_2-D_2 exchange probability is found to be incident azimuthal angle dependent on Pt(s)[6(111)x(100)] surface. This is simliar to that on Pt(s)[6(111)x(111)] surface, thus, the steps, not the detailed steps structure, are the main cause of the high exchange probability. The dependence can be understood in terms of the scattering geometry and the enhanced bond breaking properties of the step sites.
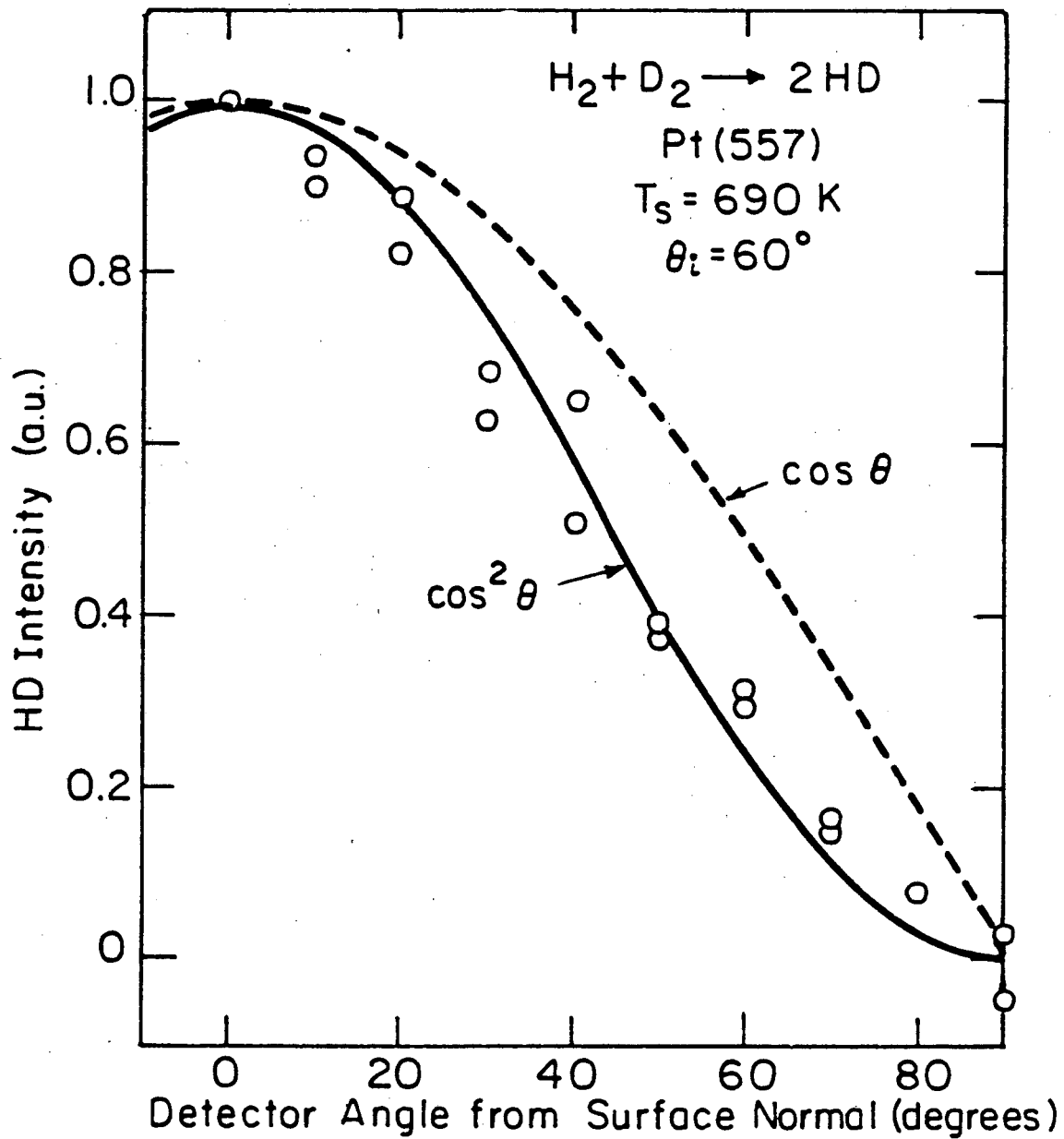
References

1. W. Van Willigen, Phys. Lett. A28, 80 (1968).

2. R. L. Palmer, J. N. Smith, Jr., H. Saltsburg and D. R. O'Keefe, J. Chem. Phys. 53, 1666 (1970).

3. J. N. Smith, Jr. and R. L. Palmer, J. Chem. Phys. 56, 13 (1972).

4. A. E. Dabiri, T. J. Lee and R. E. Stickney, Surface Sci. 26, 522 (1971).

5. T. L. Bradley, A. E. Dabiri and R. E. Stickney, Surface Sci. 29, 590 (1972).

6. T. L. Bradley and R. E. Stickney, Surface Sci. 38, 313 (1973).

7. M. Balooch and R. E. Stickney, Surface Sci. 44, 310 (1974).

8. M. Balooch, M. J. Cardillo, D. R. Miller and R. E. Stickney, Surface Sci. 46, 358 (1974).

9. G. Comsa, R. David and K. D. Rendulic, Phys. Rev. Lett. 38, 775 (1977).

10. G. Comsa and R. David, Chem. Phys. Lett. 49, 512 (1977).

11. G. Comsa, R. David and B. J. Schumacher, Surface Sci. 85, 45 (1979).

12. G. Comsa, R. David and B. J. Schumacher, Surface Sci. 95, L210 (1980).

13. G. Comsa and R. David, Surface Sci. 117, 77 (1982).

14. S. T. Ceyer, W. L. Guthrie, T. H. Lin and G. A. somorjai, J. Chem. Phys. 78, 6982 (1983).

15. M. Salmeron, R. J. Gale and G. A. Somorjai, J. Chem. Phys. 67, 5324 (1977).

16. T. Engel and H. Kuipers, Surface Sci. 90, 162 (1979).

17. I. E. Wachs and R. J. Madix, Surface Sci. 58, 590 (1976).

18. M. Salmeron, R. J. Gale and G. A. Somorjai, J. Chem. Phys. 70, 2807 (1979).

19. J. P. Cowin, C. F. Yu, S. J. Sibener and J. E. Hurst, J. Chem. Phys. 75, 1033 (1981).

20. B. Poelsema, G. Mechtersheimer and G. Comsa, Surface Sci. 111, 519 (1981).

21. K. E. Lu and R. R. Rye, Surface Sci. 45, 677 (1974).

22. K. Christmann, G. Ertl and T. Pignet, Surface Sci. 54, 365 (1976).

23. K. Christmann and G. Ertl, Surface Sci. 60, 365 (1976).

24. R. W. McCabe and L. D. Schmidt, Surface Sci. 65, 189 (1977).

25. D. M. Collins and W. E. Spicer, Surface Sci. 69, 85 (1977).

26. M. J. Cardillo, M. Balooch and R. E. Stickney, Surface Sci. 50, 263 (1975).

27. J. C. Tully, Surface Sci. 111, 461 (1981).

28. D. R. Horton and R. I. Masel, Surface Sci. 116, 13 (1982).

29. D. R. Horton, W. F. Banholzer and R. I. Masel, Surface Sci. 116, 22 (1982).

30. C. T. Campbell, G. Ertl, H. Kuipers and J. Segner, Surface Sci. 107, 220 (1981).

31. J. C. Tully, J. Chem. Phys. 73, 6333 (1980).

32. C. A. Becker, J. P. Cowin, L. Wharton and D. J. Auerbach, J. Chem. Phys. 67, 3394 (1977).

33. Y. W. Tsang and L. M. Falicov, J. Mol. Catal. 3, 351 (1977/1978).

Figure Captions

Fig. 5.1 Angular distribution of HD produced from H_2-D_2 exchange
reaction.

Fig. 5.2 Time-of-flight distribution of the produced HD at 690K and
normal angle detection. The solid line is the corresponding
Maxwellian distribution at 690K.

Fig. 5.3 The HD mean kinetic energy divided by 2k as a function of the
crystal temperature. Dashed line indicates the temperature
that would result for equilibrium between the surface and the
produced HD.

Fig. 5.4 Two time-of-flight distributions for HD produced from
H_2-D_2 exchange reaction. The closed circles represent
the TOF distribution for the normal angle detection and the
open circles 60 degrees from the normal angle detection.

Fig. 5.5 The HD average kinetic energy divided by 2k is plotted as a
function of the desorption angle.

Fig. 5.6 Production of HD on the Pt(557) surface as a function of the
azimuthal angle of incidence, ϕ. ϕ equals to 90 degrees when
the primary incident beam impinges perpendicularly onto the
open side of the step.

Fig. 5.7 Potential energy diagrams showing the interaction of the
hydrogen with a metal surface. The atomic potential curve
and the molecular curve cross at 7(a) a level higher than
that of H_2 or 7(b) a level lower than that of H_2.

Figure 5.1

XBL 836-5874
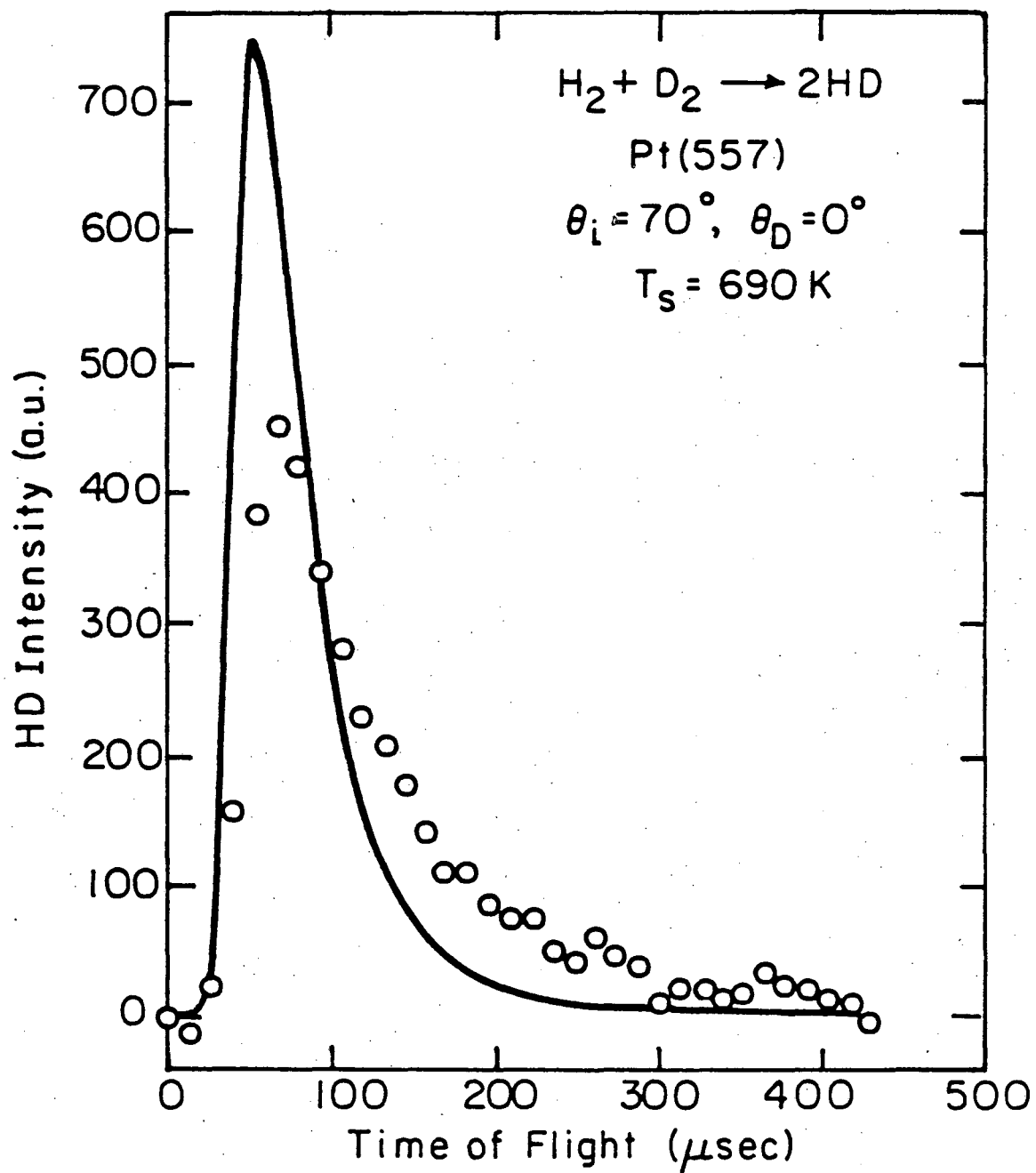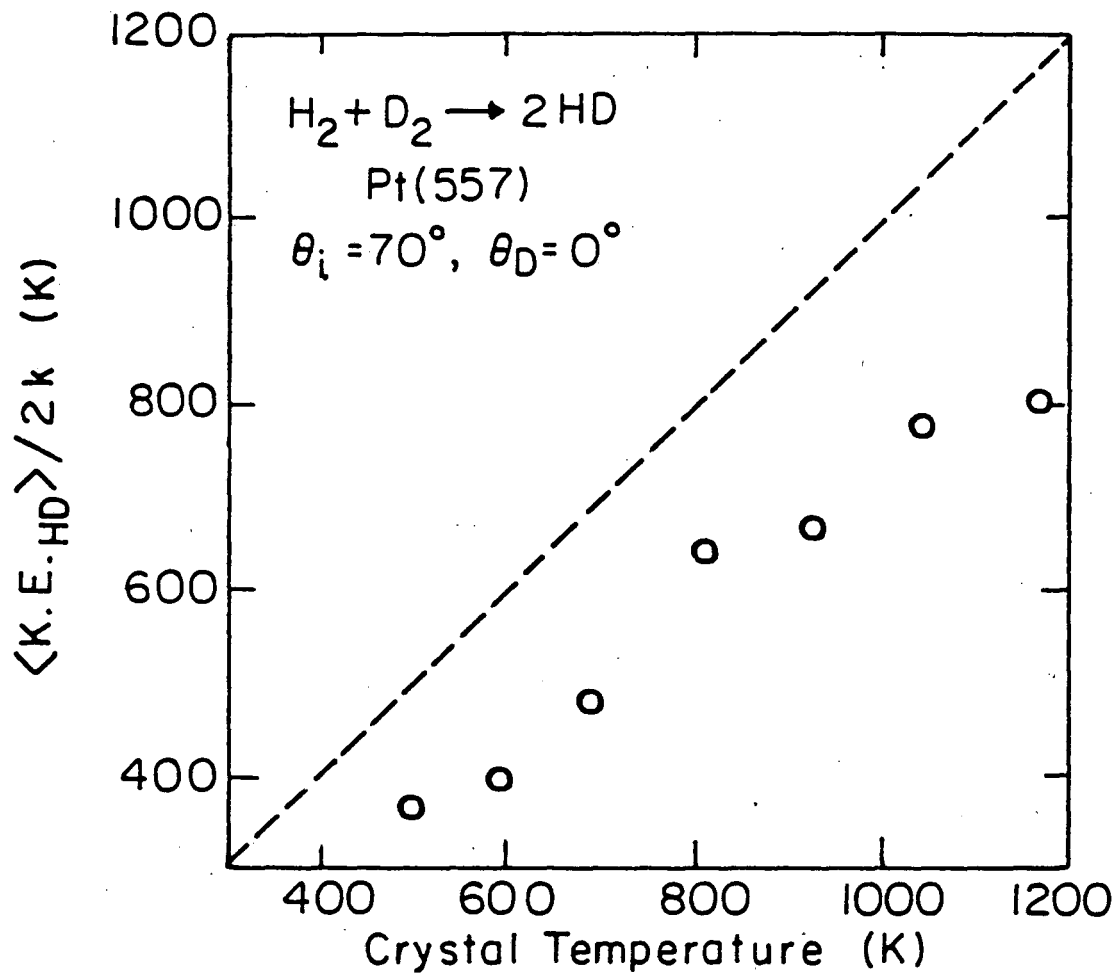
$$H_2 + D_2 \longrightarrow 2HD$$
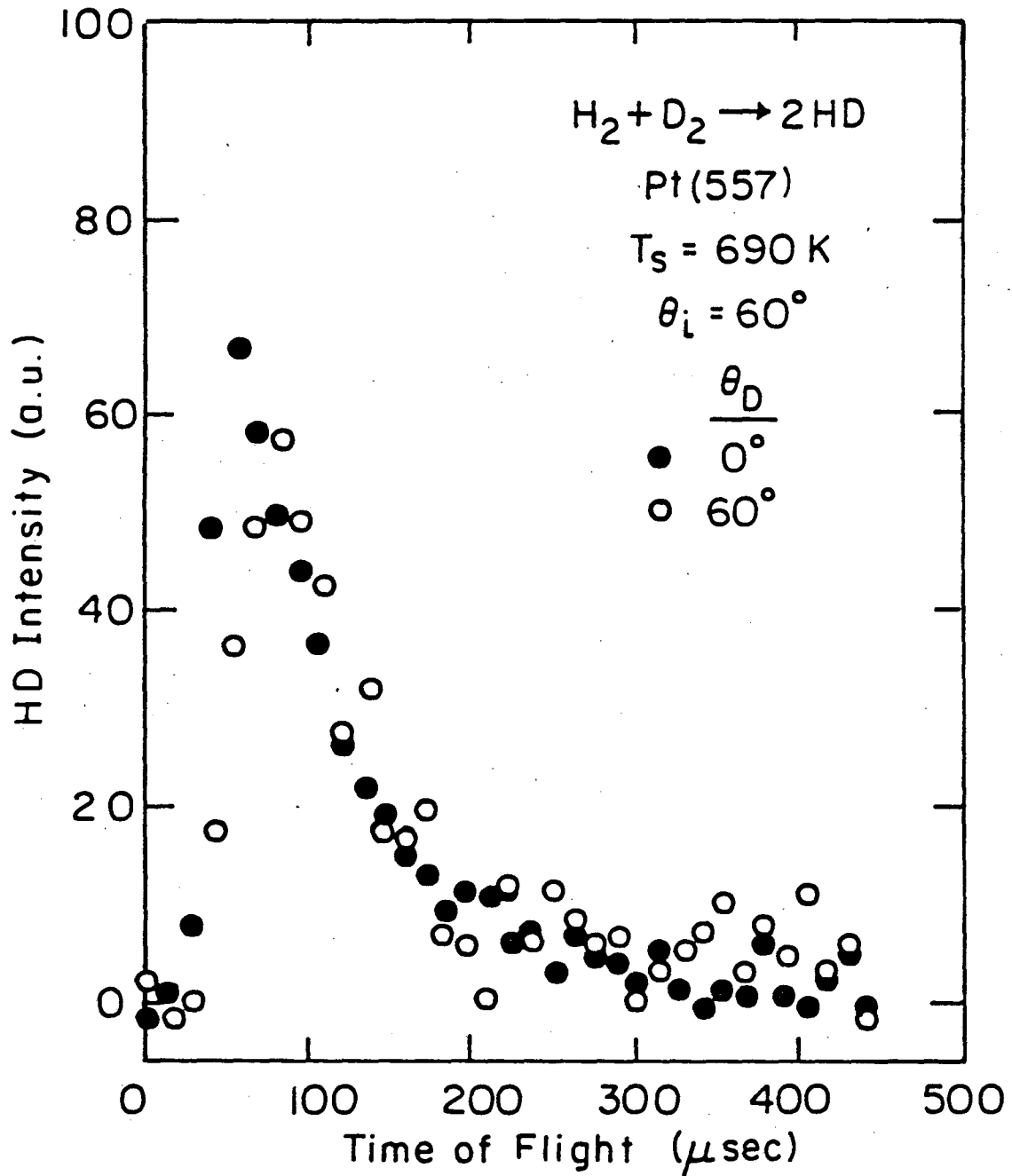
Pt(557)

$\theta_i = 70°, \ \theta_D = 0°$

$T_s = 690 \, K$

Figure 5.2

XBL 836- 5875

XBL 836-5876

Figure 5.3

Figure 5.4

$H_2 + D_2 \rightarrow 2\,HD$

Pt(557)

$T_s = 690\ K$

$\theta_i = 60°$

〈K.E.$_{HD}$〉/2k (K)

Detector Angle from Surface Normal (degrees)

XBL 836-5878

Figure 5.5

$H_2 + D_2 \longrightarrow 2\,HD$

Pt(557)

$T_s = 690\,K$

$\theta_i = 60°,\ \theta_D = 0°$

$\Phi = -90°$ $\Phi = 90°$

HD Intensity (a.u.)

Azimuthal Angle, Φ (degrees)
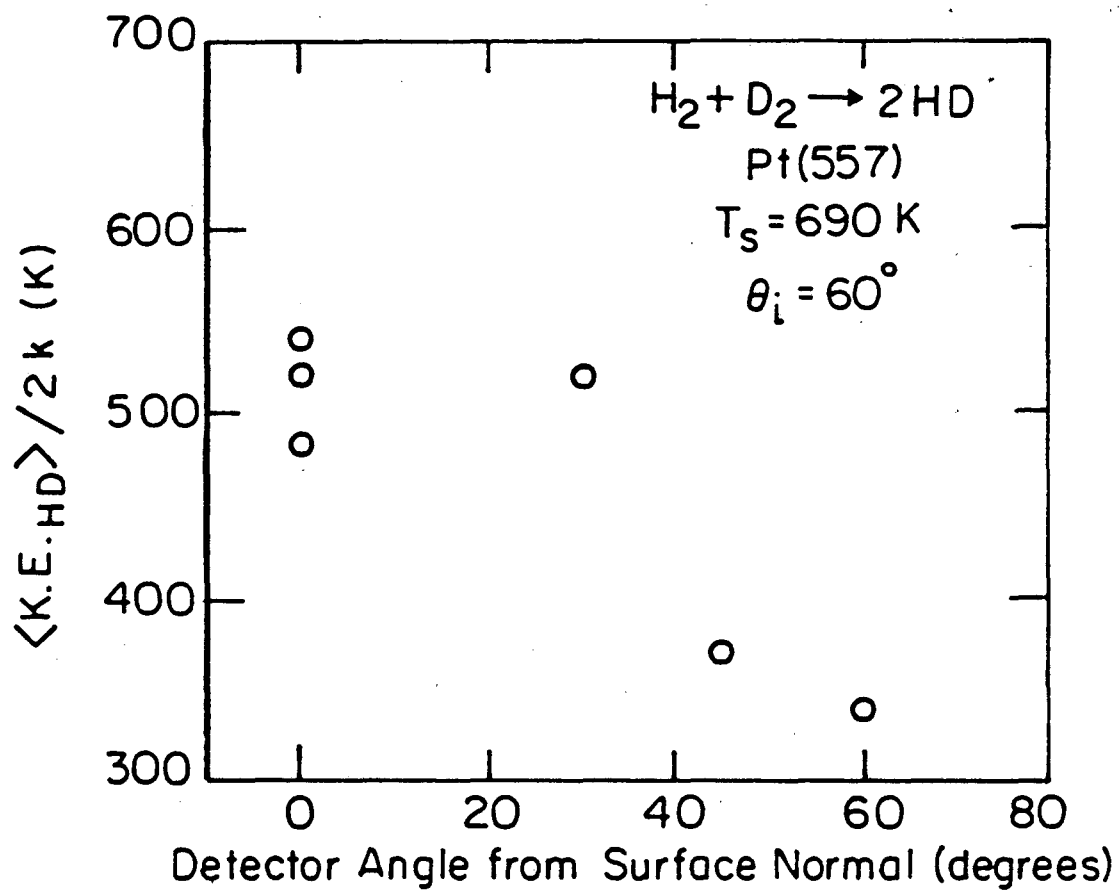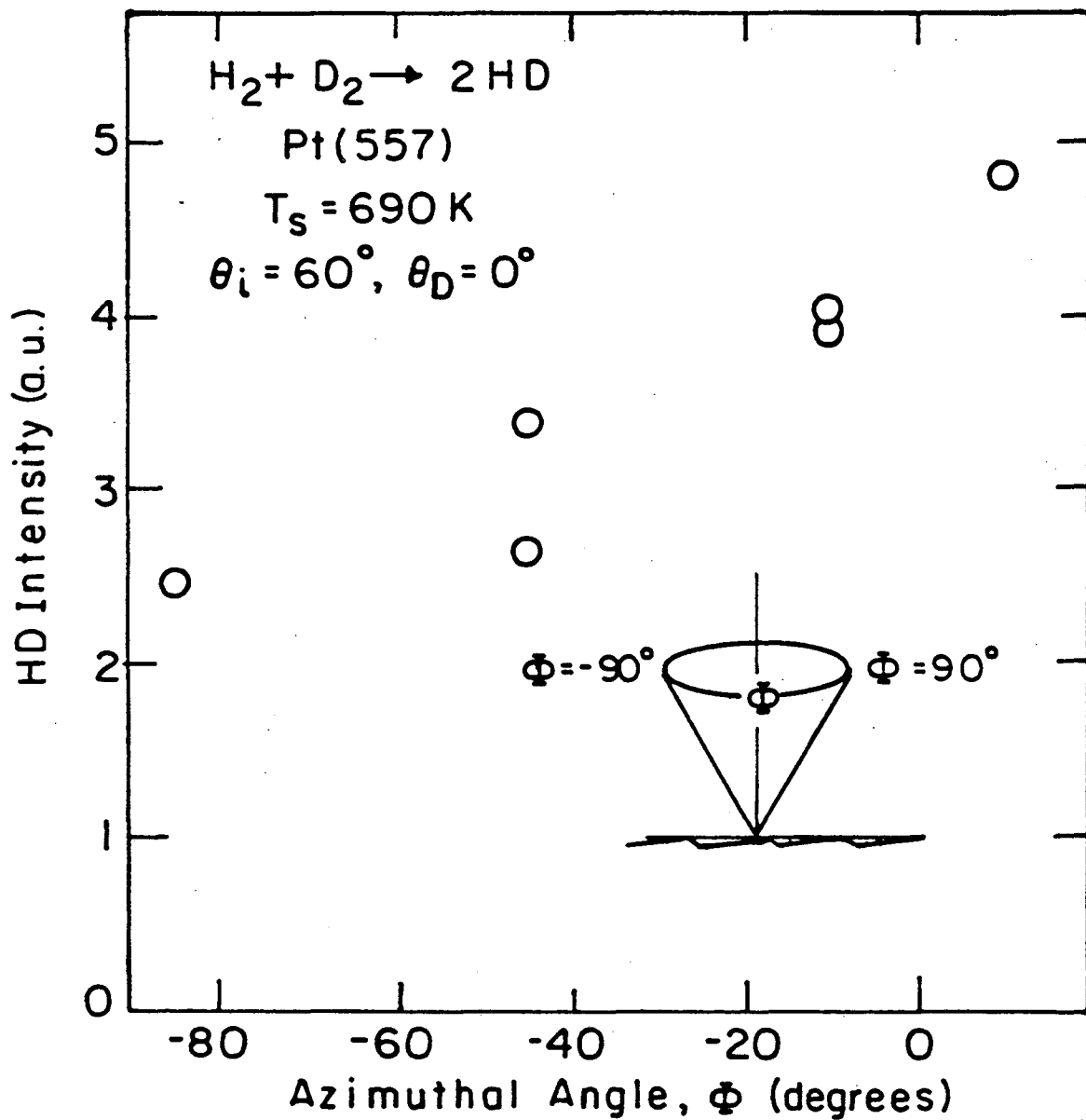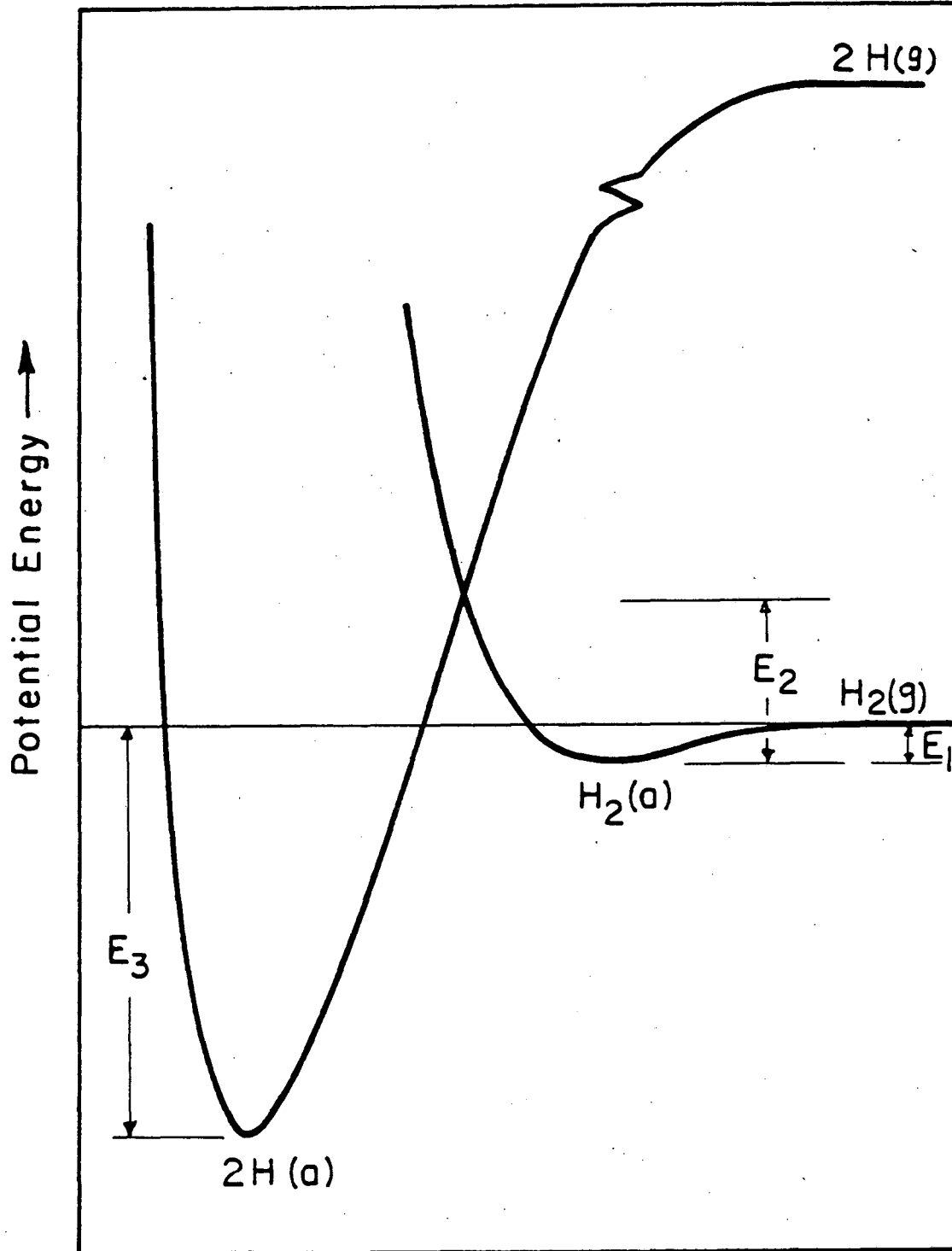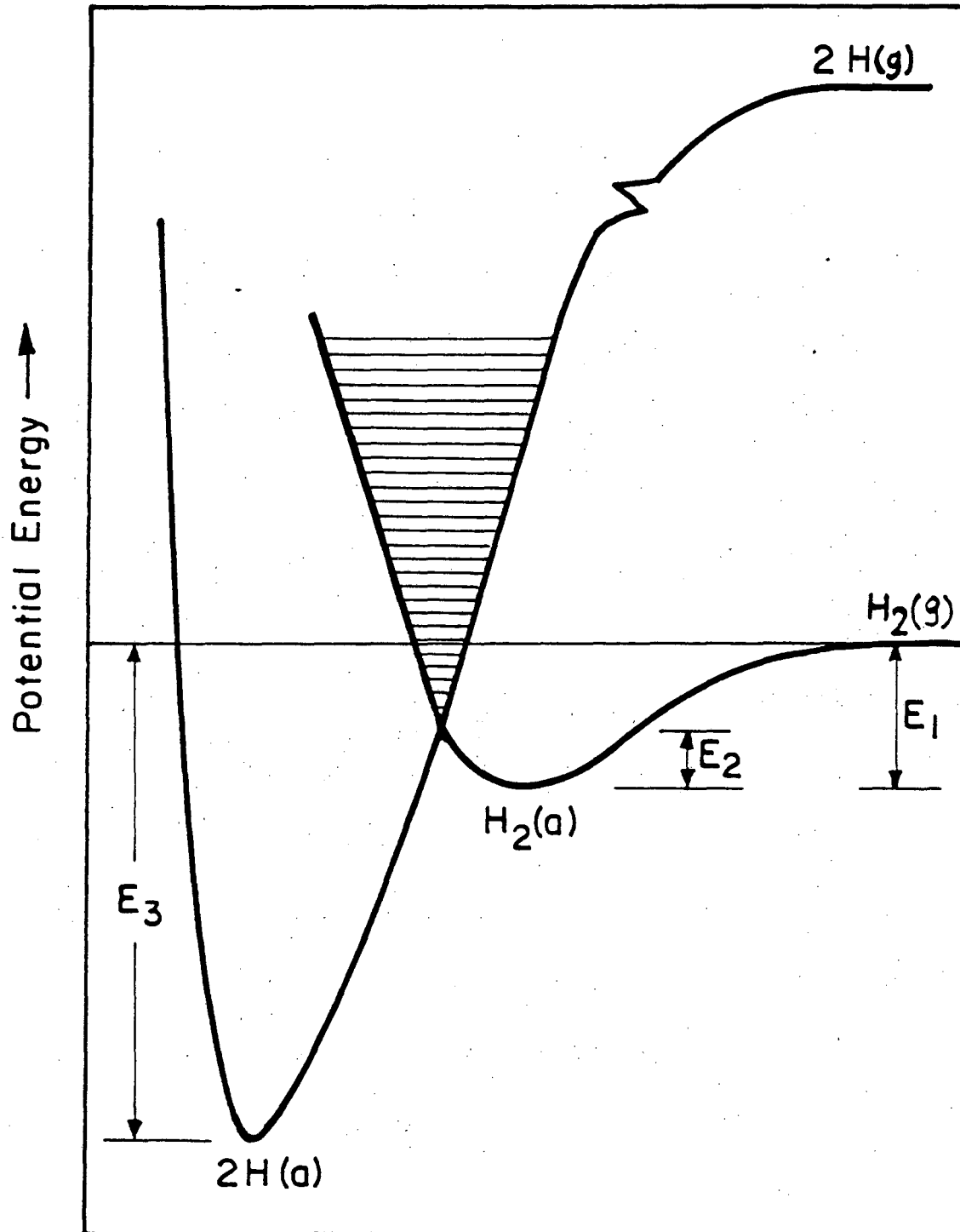
XBL836-5879

Figure 5.6

XBL 836-5880

Figure 5.7a

138

Figure 5.7b

XBL 836-5881

CHAPTER VI. THE DYNAMICS OF ATOMIC HYDROGEN AND DEUTERIUM

RECOMBINATION ON Pt(557) SURFACE

6.1 Introduction

Although the understanding of the interaction between atomic

hydrogen and solid surfaces is very important from both a theoretical

and a practical point of view, very little experimental work has been

done in this area (1-5). Theoretically, H is the simplest atom and so

there is great interest in theoretical calculations of its chemical

interaction with surfaces. Practically the walls of fusion devices

are known to degrade under hydrogen plasma impact although the exact

mechanism is a point of controversy (1). The plasma etching process

used in electronic device fabrication cannot be understood if one has

no knowledge of how the atoms, F, Cl, and H interact with the silicon

surface (6). Finally, the knowledge of the equilibrium and kinetic

properties of H on surfaces is essential to the understanding of the

evolution of interstallar gas clouds (7).

The study of the interaction between atomic hydrogen (deuterium)

and the platinum surface is presented in this chapter. With separate

atomic hydrogen and deuterium incident beams, the velocity

distribution of the product HD molecule is measured at substrate

temperature of 150K ~ 700K. Above 500K, the kinetic energy divided by

2k is slightly colder than the corresponding substrate temperature and

increases as the crystal temperature increases. However, below room

temperature, it increases as the crystal temperature decreases and

becomes higher than the corresponding substrate temperature. The hot

product is interpreted by assuming that some of the incident atoms can react with chemisorbed atoms at high coverage before they are in thermal equilibrium with the surface. The results of this nonstatistical distribution of energy among products of chemical reactions on surfaces are very useful for uncovering information about the dynamics of the reactive event.

6.2 Experimental

The apparatus is the modified system described in Section 2.3 with additional modification to cool the sample down to 150K. A cryopump with both cold and warm panels removed is mounted to an 8" conflat flange and used to cool the crystal. Because the sample needs to translate ~7.5" from the surface analysis position to the scattering position, a 6" long copper braid is used to connect the cryopump cold stage to a copper rod which is attached to the manipulator with proper insulation. Another 2" copper braid connects the copper rod to a platinum foil on which the crystal is mounted. With this modification, the azimuthal rotation is no longer available and the variation of polar angle is also significantly reduced. Nevertheless, Auger electron spectroscopy and argon ion sputtering can be used. Because of the long distance between the cryopump and the crystal, the sample can only be cooled to 150K while cryopump cold-stage is at 14K. It takes 15 min. to cool the crystal down from 1200K to its ultimate minimum temperature.

The two atomic hydrogen and deuterium beams are produced in the discharges located at the 1mm nozzle tips (8). The plasma is produced

in a microwave cavity at a pressure of 2 Torr. By comparing the
direct beam intensities with or without the plasma, we estimate that
there is about 35 percent dissociation. Some argon (20 percent) is
added to the source whenever the plasma is not stable. The primary
beam is incident at an angle of 70 degrees along the step edges of the
crystal. The Pt(557) crystal was cleaned by argon ion sputtering and
annealing. The background pressure with the cryopump operating is
7×10^{-10} Torr and increases to 8×10^{-9} Torr when both beams are
incident on the crystal.

For the surface residence time measurement, the incident atomic
hydrogen beam was chopped with the tuning fork chopper at 150 Hz and
the waveform of the HD product is collected with the 255 multi-channel
scalar. The same program which controls the TOF distribution collec-
tion is used to control the waveform data collection. A trigger from
a pick-up coil of the tuning fork chopper is used to trigger the
multi-channel scalar.

6.3 Results

Figure 1 shows two TOF distributions of the HD product for
detection normal to the surface. The open circles represent the
distribution at a substrate temperature of 200K and the closed circles
500K. The peak intensities of the distributions were adjusted to be
the same. The striking feature is that the velocity of the HD product
at a substrate temperature of 200K is higher than that at 500K.
Quantitatively, the average kinetic energy divided by 2k for
T_s = 200k is 615K which is much higher than the substrate temperature

whereas for T_s = 500K it is 300K, lower than the substrate temperature. The distribution for T_s = 200K is also considerably wider than that for T_s = 500K. It should be noted that there is high signal intensity (70 percent of the peak intensity) at the third channel indicated with the arrow in the figure. This channel's signal comes from the HD with the kinetic energy of .16 ev or 1915 K and exists only if the crystal temperature is below 300K. The average energy divided by 2k is only 615K because of the wide distribution, meaning that there is a significant amount of slow product to bring the average energy down. Nevertheless, a considerable amount of HD has a temperature of 1915K.

The average kinetic energy divided by 2k of the produced HD as function of the crystal temperature is shown in Fig. 2. If there were complete accommodation between the HD molecules and the surface, the data points would lie on the dashed line. As the substrate temperature increases from 500K to 690K, the average kinetic energy divided by 2k increases and is slightly lower than the corresponding substrate temperature. Similar results were found (Chapter V) when the incident beams were H_2 and D_2 rather than H and D. The striking feature is that as the crystal temperature decreases from 500K to 200K, the average energy divided by 2k increases from 300K to 615K and for T_s < 300K is higher than the corresponding crystal temperature. As we mentioned before, for T_s < 300K a significant amount of HD leaves the surface with energy as high as 1915K.

The experimental TOF distribution for T_s = 200K is compared with the Maxwellian distribution at 200K (solid curve) in Fig. 3. The theoretical peak intensity is adjusted to be the same as that of the experimental data. Although the "hot" molecules are definitely not from those equilibrated with the surface, the tails of the distributions seem to indicate that the "cold" product is colder than the substrate.

To measure the surface residence time, the incident atomic hydrogen was chopped at 150 Hz and the HD product waveform was collected (9). The waveforms as the function of the crystal temperature are shown in Fig. 4. At substrate temperature of 690K, the waveform does not demodulate because of the short residence time. As the temperature decreases, the residence time increases and the waveform demodulates correspondingly as can be seen for T_s = 500 and 300K. However, the interesting feature is that the waveform appears again, although with low intensity, at 200K indicating that the residence time for some incident atoms becomes shorter.

If the HD signal is proportional to the sticking coefficient and assuming that molecular hydrogen has a sticking coefficient of 0.3 on the stepped Pt(557) surface at 690K (10), we estimate that atomic hydrogen and deuterium have unit sticking coefficient. The HD signal decreases as the crystal temperature decreases below room temperature and almost completely disappears at 150K. This is concluded from the observation that the time needed to obtain a TOF distribution increases as the crystal temperature decreases.

6.4 Discussion

It is useful to review the major features of the measurements before discussing the proposed model. The important results are as follows. The average kinetic energy of the HD product increases as the crystal temperature decreases from 500K to 200K and a significant amount of HD leaves the surface with kinetic energy as high as 1915K at a substrate temperature of 200K. Although the product residence time increases as the substrate temperature decreases from 690K to 300K, it decreases with further lowering of the substrate temperatures.

All the anomalous features seem to occur below 500K. Above this temperature, the average kinetic energy divided by 2k increases as substrate temperature increases and is slightly lower than the crystal temperature. This is consistent with the results obtained with H_2 and D_2 incident beams as described in Chapter V and explained with the assumption that dissociative adsorption is non-activated. The agreement between these two experimental results confirms that the H_2-D_2 exchange reaction occurs through adsorbed H and D atoms. It also indicates that adsorbed H and D atoms dissipate all of their chemical energy, at least 53 Kcal/mole, and are in thermal equilibrium with the surface before finding another atom with which to recombine and desorbs. The interaction time decreases as the crystal temperature increases in this temperature range, as expected. Since the heat of adsorption for atomic hydrogen on the platinum surface is about 63 Kcal/mole (11), the unity sticking coefficient at a substrate temperature of 690K is not surprising.

Since the striking features occur below room temperature, the reason for the abnormal results is probably related to the coverage of the adsorbates. One possiblity is that the interaction potential is a strong function of the coverage as suggested in the case of CO oxidation on the platinum surface (12). If the interaction potential is non-activated for molecular hydrogen adsorption at low coverage and activated at high coverage, then the average kinetic energy of the product would increase as the crystal temperature decreases causing the coverage to increase. As discussed in Chapter V, the high activation energy will force the recombination to occur at higher potential energy, thus, the translational energy of the product will be higher. The existence of a coverage dependent interaction potential is supported by the fact that flash desorption of hydrogen on Pt(111) shows two states β_1 and β_2 (13). The difference between the flash desorption peak temperatures for the β_2 state at low coverage and the β_1 state at high coverage is about 150K. The appearance of lateral interactions between neighboring hydrogen atoms has been suggested to be the origin of β_1 state (13) and supported by the experimental results of electron energy loss spectroscopy (14).

Although this model explains some of the experimental findings, it is not consistent with the following results. The TOF distribution at substrate temperature of 200K is too wide to be explained by the increase of the activation barrier with coverage. Indeed, all the experimental results show that the TOF distribution is narrower than the corresponding Maxwellian distribution when there is an activation

barrier for associative desorption (15-18). The appearance of the waveform at 200K in Fig. 4 indicates short residence time which is hard to correlate with an increase in coverage. Thus, this model should be excluded.

The following model appears to be able to explain all the experimental findings satisfactorily. Consider a hydrogen atom that strikes the platinum surface and is trapped in the potential well which is about 63 Kcal/mole deep. The trapped atom will not be in thermal equilibrium with the surface instantaneously since the energy transfer is not perfectly efficient. The period of time between the initial collision and reaching thermal equilibrium will depend on the rate of dissipation of the chemisorption energy. If the trapped hydrogen atom does not have the chance to recombine with other chemisorbed atoms before it is in thermal equilibrium with the surface, there will not be any recombination energy available for the product and the product energy will be the same for incident beams that are either atomic or molecular. However, if the trapped hydrogen atom recombines with a chemisorbed deuterium atom before it is in thermal equilibrium with the surface, there is some chemical energy available that could be carried away by the product. Thus, the amount of chemical energy available for the product is strongly dependent on the elapsed time between the initial collision of the atom with the surface and the recombination reaction. Conceivably, this elapsed time depends on the coverage.

Above room temperature, the coverage is low and the trapped atom dissipates all its chemical energy before recombination takes place, thus, the product kinetic energy is controlled by the interaction potential as discussed before. As the crystal is cooled down below room temperature, the coverage of the hydrogen (deuterium) will be high. Under these conditions, one can roughly classify the incident atoms into three groups as they impinge on the surface. The first group includes those atoms which collide with the open platinum surface and are far away, for example 2Å, from any chemisorbed hydrogen (deuterium) atom. The second group consists of those atoms which collide with the open platinum surface and are within 2Å of any chemisorbed atom. Finally, the third group consists of those which are incident at sites where atoms are already adsorbed. The third group atoms are probably scattered back into the gas phase instantly. This is concluded from the facts that HD signal decreases as the crystal temperature decreases from room temperature and disappears at 150K when one monolayer coverage is reached.

The first group atoms will have long residence time, keeping the coverage high, and reach thermal equilibrium with the surface before recombination can take place. Thus, the kinetic energy of HD produced from this group's atoms will be determined by the interaction potential and crystal temperature. Extending the results above 500K down to below room temperature, the HD kinetic energy divided by 2k should be slightly lower than the corresponding substrate temperature.

The second group atoms can react with the chemisorbed atoms immediately because of the following reasons. There are chemisorbed atoms within 2Å of the incident atoms, and the reaction is probably non-activated. Furthermore the reaction is exothermic by 43 Kcal/mole assuming the binding energy of atomic hydrogen with platinum surface to be 63 Kcal/mole and that there is no energy exchange between the incident atom and the surface before the reaction occurs. If there is some energy exchange but the reaction takes place before the incident atom reaches thermal equilibrium with the surface, which is probably true in this case, the reaction is still exothermic and the liberated energy can be carried away by the product. Thus, the HD kinetic energy divided by 2k can be higher than the substrate temperature.

The experimental results below room temperature can be explained with the above model. As the crystal temperature decreases, the coverage increases and the percentage of the HD produced from the second group incident atoms increases. Since these HD molecules can be "hotter" than the substrate, the average kinetic energy divided by 2k will increase and can be higher than the crystal temperature as shown in Fig. 2. At a substrate temperature of 200K, HD can be produced from the second group incident atoms as well as the first group incident atoms. As mentioned before, the HD produced from the first group incident atoms is slightly "colder" than the substrate temperature. Thus, the TOF distribution is wide and the hot product is "hotter" and the cold product is "colder" than the substrate temperature as shown in Fig. 3. The appearance of the waveform at

200K in Fig. 4 is due to the HD produced from second group incident atoms. These atoms react immediately with the chemisorbed atoms, thus, the product waveform is not demodulated.

There is a significant amount of HD leaving the surface with translational energy of 1915K which corresponds to 10 percent of the liberated chemical energy. It is very likely that a considerable amount of reaction energy will end up in the product vibrational and rotational modes although no experimental results are available. Theoretically, Tully has studied the reaction of incident oxygen atoms that strike within 2Å of an adsorbed carbon atom on the Pt(111) surface and found that 90 percent of the 6 eV of liberated energy is carried away by the product CO molecule (19). He determined that 30 percent of reaction energy was carried away as the translational energy of the product. A qualitative argument explaining this phenomenon was suggested by Harris and Kasemo (20). They referred to the trapped atoms which are not in thermal equilibrium with the surface as "hot precursors" and the resulting interaction mechanism as a "precursor mechanism".

There are many experimental results showing product temperatures that are higher than the corresponding substrate temperatures. Examples are N_2 desorbing from sulphur covered Fe (21) and D_2 desorbing from Ni (15), sulphur covered Pd (16), and Cu (17) surfaces. However, the reactants are probably in thermal equilibrium with the surface and the existence of an activation barrier for dissociative adsorption is the origin of the excess energy. The hot

molecules produced from the second group incident atoms in this study desorb through a non-activated interaction potential and the lack of equilibration in the potential well is the origin of the excess energy. Thus, this is the first experimental result which shows that energy equilibration on solid surfaces is not extremely fast, and thus, that the dynamics of the reactive events can be studied.

6.5 Conclusion

The velocity distribution of HD produced from atomic hydrogen and deuterium recombination on Pt(557) surface is measured for substrate temperature of 200-700K. The average kinetic energy divided by 2k is slightly lower than the corresponding substrate temperature between 500-700K and increases as the crystal temperature increases. However, it increases as the crystal temperature decreases from 500-200K and becomes higher than the substrate temperature below 300K. At 200K, the distribution, is considerably wider than the Maxwellian distribution and there is a significant amount of HD leaving the surface with 1915K translational energy. The waveform measurement indicates that the residence time increases as the crystal temperature decreases from 700K to 300K and decreases for some of the incident atoms as the crystal temperature decreases from 300K to 200K.

The striking experimental findings are interpreted by assuming that some of the incident atoms can react with chemisorbed atoms at high coverage before they are in thermal equilibrium with the surface. This mechanism is very different from the previous explanation of hot products (15-18;21-22) in which the activation barrier is believed to be the origin of the excess energy.

References

1. O. Auciello, A. A. Haasz and P. C. Stangeby, Phys. Rev. Lett. <u>50</u>, 783 (1983).

2. E. Ghio, L. Mattera, C. Salvo, F. Tommasini, and U. Valbusa, J. Chem. Phys. <u>73</u>, 556 (1980).

3. G. Marenco, A. Schutte, G. Scoles, and F. Tommasini, J. Vac. Sci. Technol. <u>9</u>, 824 (1972).

4. M. Balooch and D. R. Olander, J. Chem. Phys. <u>63</u>, 4772 (1975).

5. B. J. Wood and H. Wise, J. Phys. Chem., <u>73</u>, 1348 (1969).

6. H. F. Winters, J. W. Coburn, and T. J. Chuang, J. Vac. Sci. Technol. B, <u>1</u>, 469 (1983).

7. L. Spitzer, Jr. and E. G. Zweibel, Astrophys. J. <u>191</u>, L127 (1974).

8. S. Y. Ceyer, Ph.D. Thesis, U. California, Berkeley, 1979.

9. H. Sawin and R. P. Merrill, J. Vac. Sci. Technol. <u>19</u>, 40 (1981).

10. M. Salmeron, R. J. Gale, and G. A. Somorjai, J. Chem. Phys. <u>70</u>, 2807 (1979).

11. B. Poelsema, G. Mechtersheimer, and G. Comsa, Surface Sci. <u>111</u>, 519 (1981).

12. C. T. Campbell and G. Ertl, private communication.

13. K. Christmann, G. Ertl and T. Pignet, Surface Sci. <u>54</u>, 365 (1976).

14. A. M. Baro, H. Ibach and H. D. Bruchmann, Surface Sci. <u>88</u>, 384 (1979).

15. G. Comsa, R. David and B. J. Schumacher, Surface Sci. <u>85</u>, 45 (1979).

16. G. Comsa, R. David and B. J. Schumacher, Surface Sci. <u>95</u>, L210 (1980).

17. G. Comsa and R. David, Surface Sci. <u>117</u>, 77 (1982).

18. C. A. Becker, J. P. Cowin, L. Wharton and D. J. Auerbach, J. Chem. Phys. <u>67</u>, 3394 (1977).

19. J. C. Tully, J. Chem. Phys. <u>73</u>, 6333 (1980).

20. J. Harris and B. Kasemo, Surface Sci. <u>105</u>, L281 (1981).

21. R. P. Thorman and S. L. Bernasek, J. Chem. Phys. <u>74</u>, 6498 (1981).

22. D. A. Mantell, S. B. Ryali, B. L. Halpern, G. L. Haller, and J. B. Fenn, Chem. Phys. Lett. <u>81</u>, 185 (1981).

Figure Captions

Fig. 6.1 Two time-of-flight distributions for HD produced from atomic hydrogen and deuterium recombination. The closed circles represent the TOF distribution for T_s = 500K and the open circles T_s = 200K. The arrow indicates that there is a significant amount of HD leaving the surface with translational energy of 1915K.

Fig. 6.2 The HD mean kinetic energy divided by 2k as a function of the crystal temperature. Dashed line indicates the temperature that would result for equilibrium between the surface and the produced HD.

Fig. 6.3 Time-of-flight distribution of the produced HD at 200K. The solid line is the corresponding Maxwellian distribution at 200K.

Fig. 6.4 Waveforms for HD produced from atomic hydrogen and deuterium recombination on Pt(557) and for temperatures ranging from 200 to 690K.
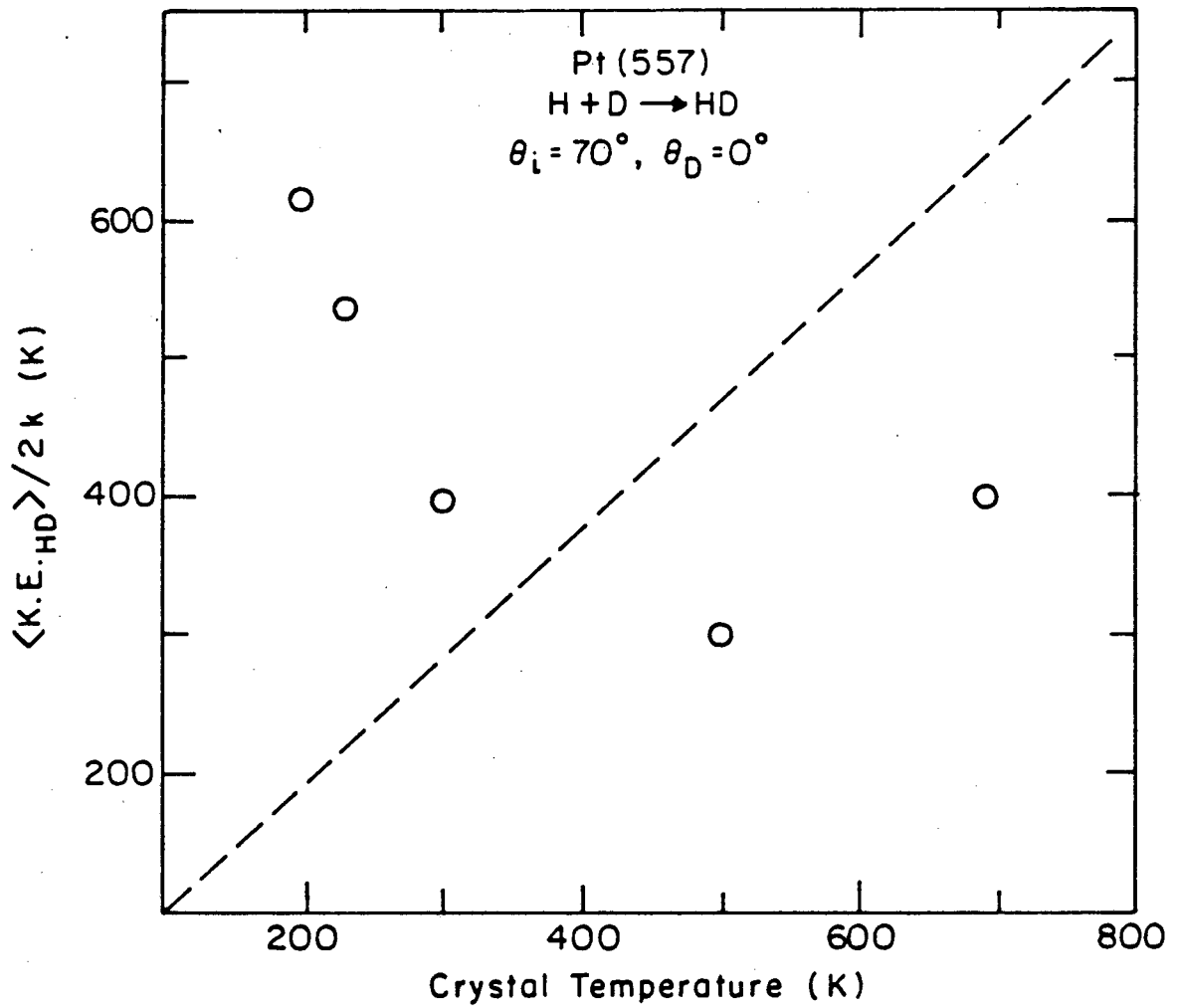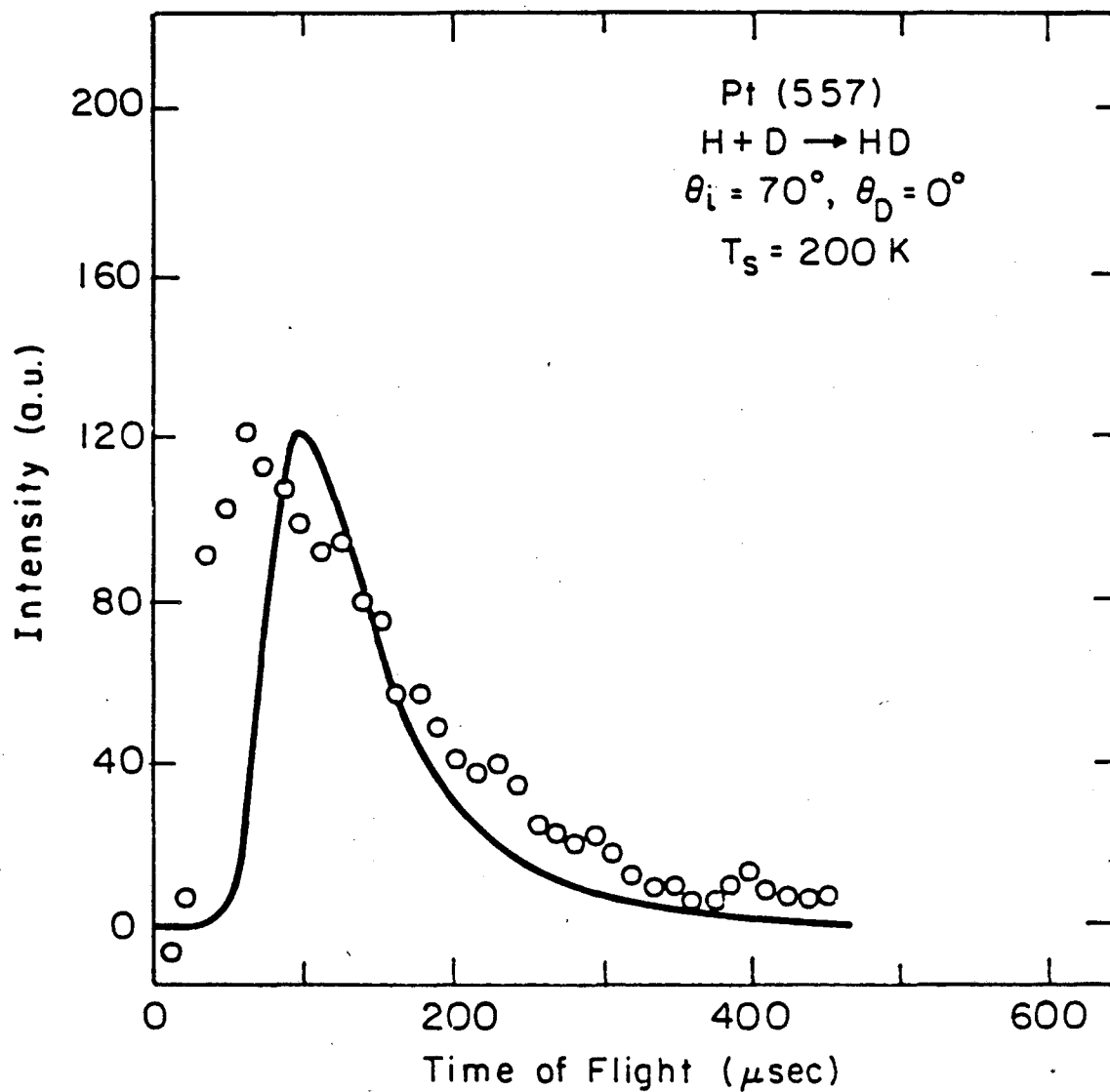
Pt (557)

H + D ⟶ HD

$\theta_i = 70°$, $\theta_D = 0°$

T_S (K)

● 500

○ 200
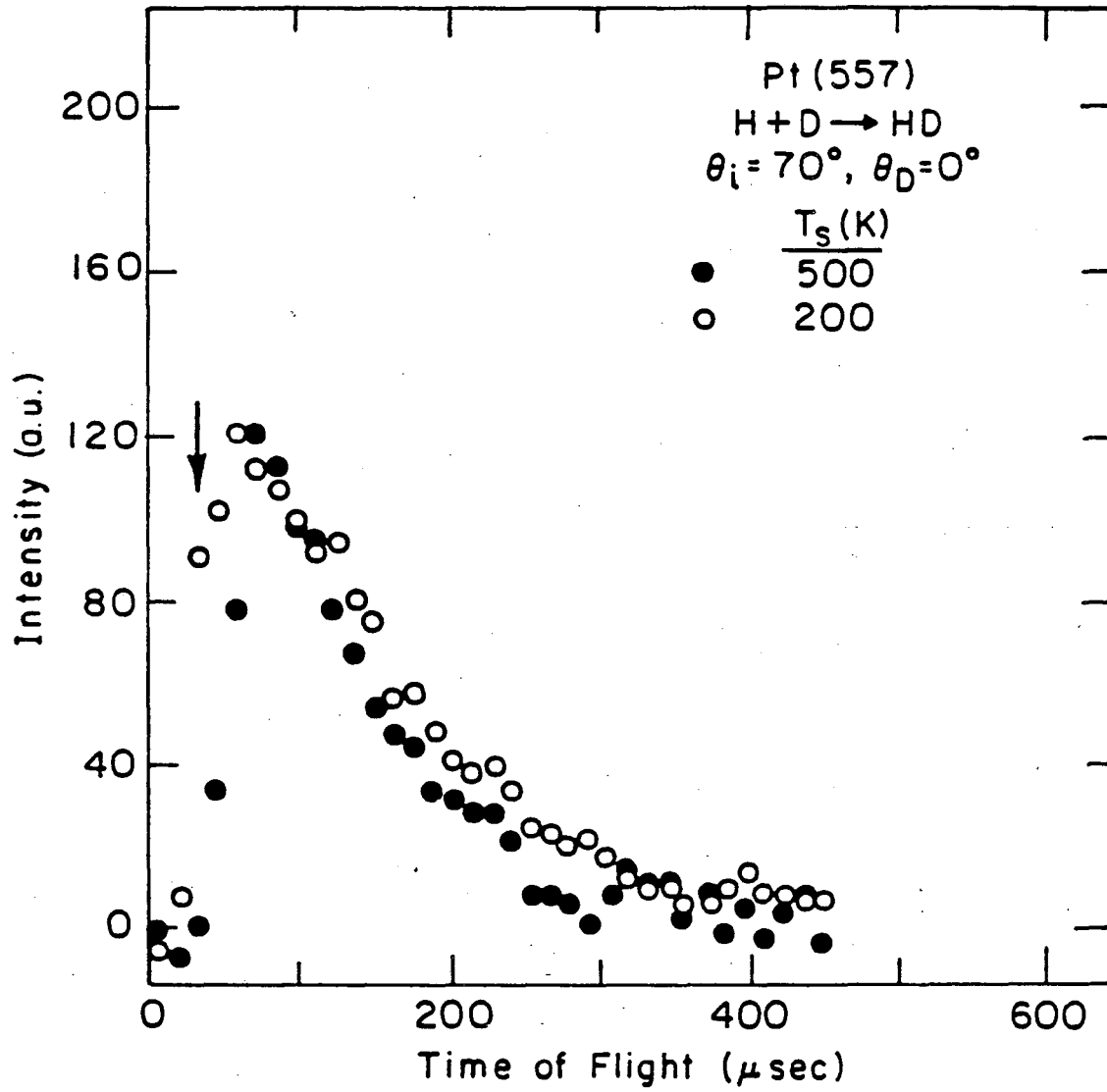
XBL 838-6089

Figure 6.1

Figure 6.2
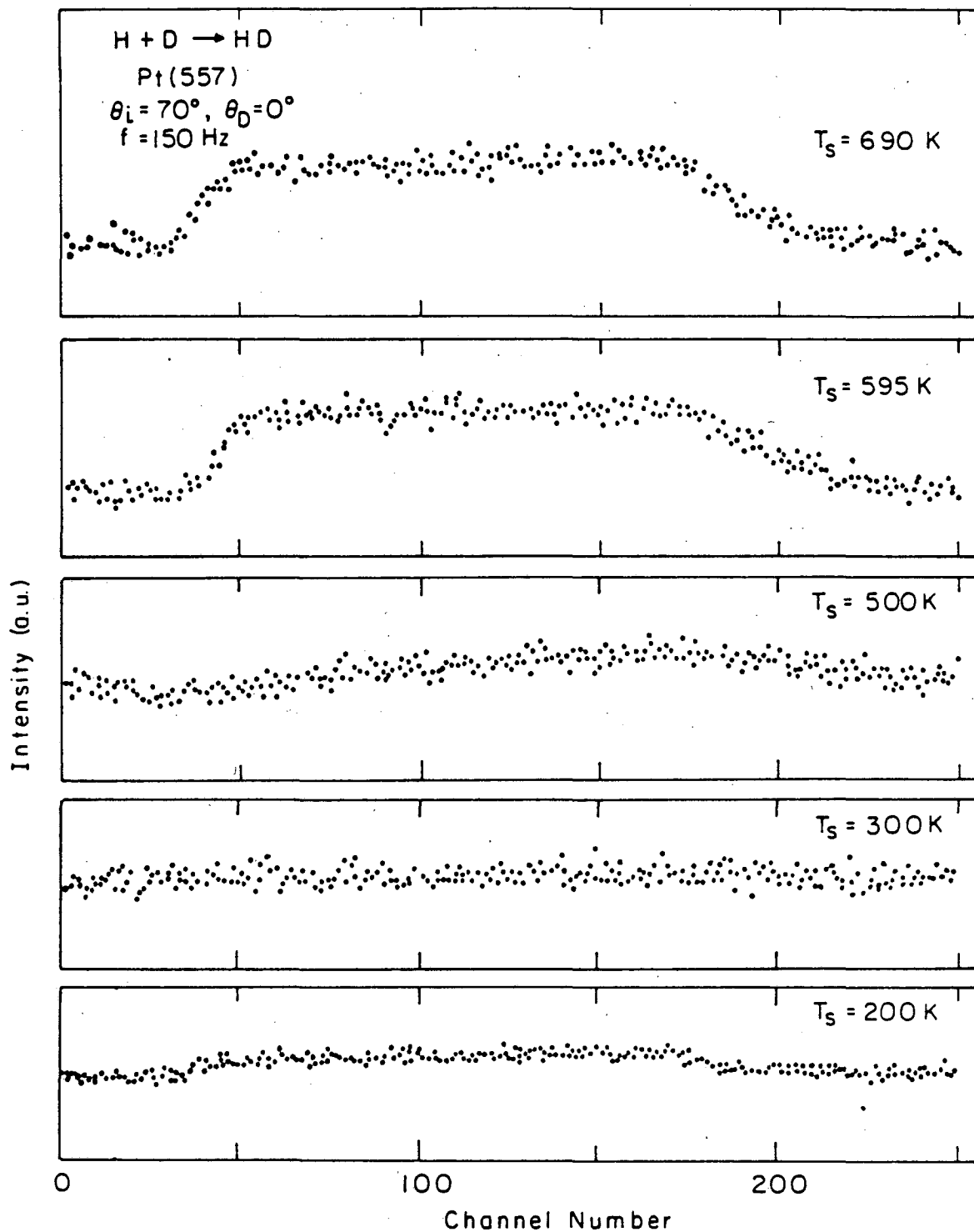
XBL 838-6088

Figure 6.3

XBL 838-6087

Figure 6.4

XBL 836-5882

CHAPTER VII. SUMMARY

The molecular beam-surface scattering technique has been used to investigate the dynamics of gas-solid interactions for strongly interacting systems. Modulated molecular beam techniques were used to study reaction mechanisms and to measure surface residence times. The measurements of angular, translational energy, and internal energy distributions of reaction products or strongly scattered molecules are used for extracting information about energy exchange dynamics, reaction mechanisms, desorption dynamics, scattering mechanisms, and the interaction potential. The deviation of energy distributions from a Boltzmann distribution, the polar angle dependence of energy distribution and the noncosine angular flux distributions allow one to obtain dynamic information.

The modulated molecular beam scattering of CO and NO from Pt(111) and Pt(557) have been studied in the temperature range of 300-1100K. For the case of CO, an adsorption-desorption model with constant sticking coefficient fits the data well for both crystal surfaces. The higher activation energy for desorption from the stepped Pt(557), as compared to the flat Pt(111), and the identical sticking coefficient for both surfaces suggest that while the incident CO can be adsorbed at the step as well as at the terrace, their desorption kinetic is controlled by the steps. It appears that any adsorbed molecule has to visit the step sites once before it desorbs. The kinetic properties of NO/Pt are found to be very different and more complex than those of CO/Pt. The data indicate that one high adsorption energy state is

sampled above 525K and a lower adsorption energy state appears suddenly below 480K. The features of the data rule out the usual linear, parallel or series processes immediately. The nonlinear process might due to the fact that the desorption kinetics are controlled by a small concentration of defects which could be blocked by some impurity at lower temperatures.

To gain insight into the energy transfer processes on a chemically interesting system, the angular, translational, and internal energy distributions of NO scattered from Pt(111) were measured and are presented in Chapter IV. We found that both trapping-desorption and inelastic scattering mechanisms apply under all of our experimental conditions, and that the trapping probability decreases as the incident beam energy or crystal temperature increases. The translational and vibrational energy accommodation cofficients are nearly equal to one for T_s < 900K and deviate from unity above this temperature due to non-equilibrated desorption. Vibrationally excited molecules are produced by the molecules scattered by the trapping-desorption mechanism whereas inelastically scattered molecules cannot be vibrationally excited. The rotational energy accommodation is very poor as compared with that of the other two modes. This may be due to the fact that NO is not a free rotor on the surface and so may be cooled down further during the desorption process. The complete energy exchange information on a system is important for comparison with theoretical calculations which need drastic approximations for strongly interacting systems.

Chapter V describes the results for the H_2-D_2 exchange reaction on the Pt(557) surface. The fact that the angular distribution is peaked at the normal and that the average kinetic energy of HD does not depend on the incident beam energy but is proportional to the substrate temperature indicates that the reaction proceeds via a Langmuir-Hinshelwood mechanism. Although the angular distribution is slightly peaked at the normal, the velocity distribution of the desorbing HD is slightly colder than the substrate temperature, and the deviation increases as the detection angle increases. This result is explained by a model which assumes that as soon as H and D recombine, they will immediately feel a repulsive force which is most likely perpendicular to the surface. The exchange probability is found to be dependent upon the incident azimuthal angle. This can be explained by the geometrical variation of the number of reactant molecules that strike the open side of the step which has higher bond breaking rate than the rest of the surface.

Finally, the dynamics of the interaction of atomic hydrogen (deuterium) with the platinum surface are reported in Chapter VI. The incident beams are atomic hydrogen and deuterium and the velocity and interaction time of the HD product are measured as a function of the crystal temperature. For crystal temperatures between 500 and 700K, the velocity distribution is slightly colder than the corresponding substrate and increases as the crystal temperature increases. The striking feature is that the average kinetic energy increases as the crystal temperature decreases from 300K to 200K. At 200K, the

distribution is considerably wider than the Maxwellian distribution, and there is a significant amount of HD leaving the surface with 1915K translational energy. The waveform measurement indicates that the residence time increases as the crystal temperature decreases from 700K to 300K and decreases for some of the incident atoms as the crystal temperature decreases from 300K to 200K. The results are interpreted by assuming that some of the incident atoms can react with chemisorbed atoms at high coverage before they are in thermal equilibrium with the surface.